Fundamentals of solute enrichment at interfaces in medium manganese steel

Von der Fakultät für Georessourcen und Materialtechnik der
Rheinisch-Westfälischen Technischen Hochschule Aachen

zur Erlangung des akademischen Grades eines

Doktors der Ingenieurwissenschaften

genehmigte Dissertation
vorgelegt von

Faisal Waqar Syed, M.Tech.

Berichter: apl. Prof. Dr.-Ing. Dierk Raabe
Univ.-Prof. Dr.-Ing Hauke Springer

Tag der mündlichen Prüfung: 27.11.2024

العلم ليس ما حُفِظَ، العلم ما نَفَعَ

الإمام الشافعي (٧٦٧-٨٢٠)

Knowledge is not what is memorised.
Knowledge is what benefits.

-Imam Shafi'i (767-820)

Acknowledgements

All praise to God for blessing me with a supportive and loving family, friends, colleagues, and mentors. I wish to convey my heartfelt appreciation to these individuals who have supported me on both personal and professional levels.

To begin with, I would like to express my sincere gratitude to Prof. Dr.-Ing. habil. Dierk Raabe for providing me with the opportunity to conduct my PhD research at the Department of Microstructure Physics and Alloy Design at the Max Planck Institute für Eisenforschung (MPIE). Furthermore, his knowledge in phase transformation in steels and related phenomena acted like a beacon of light for a stranded sailor. The river of innovation that flows in the valley of MPIE undoubtedly has its origin in his office.

My group leader, Dr.-Ing. Dirk Ponge, provided the shoulders on which I stood to see the vast ocean of physical metallurgy of steels. His doors were always open for discussing new concepts in phase transformations. I am truly grateful for the trust he placed in me regarding project selection and its progress.

Immense thanks to Prof. Binhan Sun for giving me a warm welcome to the institute. His introduction to partitioning in steels was a constant reference point whenever I encountered a problem in my research. Despite being in a time zone with an eight-hour difference, he was always available to discuss my issues.

I am especially grateful to Prof. Baptiste Gault. Without his assistance in understanding the pole analysis in the ion map for identifying the crystallography of features observed in the APT dataset, my explanation of results would not have carried this much weight.

Discussions with Prof. Stefan Zaefferer started relatively late in my PhD career. However, his explanations and lectures on the crystallographic interpretation of EBSD and TKD results significantly enhanced my thesis.

No matter how much I thank Dr. Devulapalli Vivek, Dr. Rama Srinivas Varanasi, Dr. T.S. Prithiv, and Dr. Srikakulapu Kiranbabu, it will not be enough. Whether it was a cold winter morning or the scorching summer of July, Kiranbabu and Prithiv were always there to introduce me to the atom probe tomography instrument. They were mentors in the guise of friends. I have known Vivek for almost 12 years, and not once has he refused to help me. He continued the same attitude when it came to operating STEM for me. Almost everyone had declined to investigate the complex phase boundary structure, but he always showed up. Rama was

available 24x7 to discuss matters related to magnetic field studies. He was like Google to me but with more precise answers. Many thanks to all of these friends, mentors, and colleagues.

I cannot fathom how difficult it would have been without the guidance of Ms. Monika Nellessen, Ms. Katja Angenendt, and Mr. Christian Broß when it came to operating the SEM. For someone who had never touched any characterization instrument until the start of his PhD, it was both exciting and scary to operate instruments worth millions. Their help was always a phone call away. Mr. Tezins and Mr. Sturm deserve all the praise showered upon them at the institute. Without them, I cannot imagine the state of my thesis had they not helped maintain the FIB and APT instruments. I also thank Mr. Kuhl and Mr. Beckschäffer for helping me maintain my PC.

The helping hand from my colleagues from the computational materials department is worth mentioning. Dr. Ali Tehranchi and Dr. Ujjal Saikia were instrumental in substantiating my experimental findings.

The key to a happy journey lies with whom it is traveled. My fellow compatriots at MPIE are certainly the most interesting characters in my PhD travel diary. Whether it was Sharan's dinner plans or Navyanth's cycling trips, these two always made me look forward to weekends. Table tennis evenings with Supriyo were always refreshing. Trying Chinese cuisine with Qing or Indian food with Saurabh and Mahander created memories for a lifetime. Introduction to German humour with Manuel or talking literal nonsense with Waleed, Raymond, and Kartik is something both worth remembering and remaining silent about.

One always longs for home, but Saba, Saood, Kamran, Mohamed, and Manoj never made me feel that I was away from home. Eid dinners hosted by Saba and Saood will be something I will always mention in the future. My brothers in faith, Kamran, Ubaid, and Mohamed, always stood by me in times of distress. Our quest to find the best food during Ramadan or struggle for the best result, we were comrades in arms. And need I mention Manoj? His spicy Karnataka cuisine and computer coding were both lit. Phone calls with Lavesh always made me feel as if I was in India.

Most importantly, I would like to thank my parents, my sister, and Asad Bhaijaan for their constant love, support, and unwavering efforts to motivate me to achieve knowledge and excel in whichever work I take up. The lessons of integrity and honesty taught by my parents helped me maintain scientific standards throughout my PhD journey. Oceans will dry up before I can fully ink their contributions in this journey.

Table of Contents

Abstract

In steels, solid-state phase transformations are key to achieving and understanding diverse microstructure evolution and desired mechanical properties. These phase transformations are usually accompanied by the partitioning of elements from one phase to another. When studying quaternary systems (Fe-Mn-Al-C) with interstitial (C) and substitutional alloying elements (Mn, Al), addressing the drastically different diffusivity of elements is of prime importance. The difference in diffusivity becomes even more critical during thermal processing at low temperatures, where the diffusion of substitutional elements may become the rate-controlling step. Low-temperature treatment usually results in a spike in the concentration of partitioning elements at the phase boundary, commonly referred to as enrichment at the phase boundary in conventional literature. Although the thermodynamics and kinetics of phase boundary enrichment are widely reported, the details associated with the different decoration states are scarce. This thesis focuses on establishing and understanding the fundamentals of the enrichment and decoration states of partitioning elements (Manganese; Mn, and Carbon; C) at the phase boundaries in medium manganese steels

An Fe-10Mn-3Al-0.2C wt.% alloy medium Mn alloy was subjected to complete austenitization followed by water quenching and subsequent intercritical annealing, producing a laminated microstructure with a Kurdjumov-Sachs (KS) orientation relationship existing between adjacent austenite and ferrite. The intercritically annealed sample was then subjected to low-temperature tempering (450°C) for 2, 50, and 200 hours to study the effects on Mn and C enrichment.

An investigation into the effect of grain boundaries on the enrichment of C at the phase boundary revealed that grain boundaries act as extracting agent for C from phase boundaries when they exist in a triple junction. Furthermore, no difference in C enrichment at the phase interfaces of KS and near-KS oriented phases was witnessed, ruling out that such phase boundary character difference as a primary cause for such an observation and confirming that the grain boundary is the primary source for C extraction from phase boundaries.

Further studies to comment on the solute decoration states at the phase boundaries of tempered samples, revealed in-plane linear segregation of Mn. These decorations are misfit dislocations in straight phase boundaries and superledges in curved phase boundaries. Misfit dislocations, having a mixed character, and superledges, characterized by one set plane arrangements in GT' type orientation and other set belonging to index planes with multiatomic facets, attracting Mn due to their strain energy and facet junction configurations. Over the timescale of tempering, it was observed that superledges at 450°C were fastest in approaching equilibrium with the surrounding matrix at 200 hours, while the same could not be said for misfit dislocations. However, phase boundary portions without distinct features have not yet

achieved local equilibrium partitioning values as predicted by DICTRA, though they are approaching it. This discrepancy is attributed to the initial quasi-paraequilibrium mode of partitioning, transitioning to local equilibrium over time.

Finally, to study the effect of an external magnetic field on Mn segregation at ferrite grain boundaries, an experiment was designed using a 50% cold rolled Fe-8Mn wt.% alloy and annealing at 450°C for 5.5 hours with and without a 9 Tesla magnetic field. It was found that no effect of the magnetic field on Mn segregation is observed. This can be understood by the fact that, in the absence of an external magnetic field, at 450°C the bulk ferrite is in a ferromagnetic state while the grain boundary is in a paramagnetic state. And the external magnetic field does not quite alter this state. To witness a change in segregation behaviour, both the bulk and the grain boundary would need to transition to a paramagnetic state, altering the segregation energy from -0.40eV (ferro bulk + para grain boundary) to -0.1eV for a completely paramagnetic system. Neither the annealing temperature used was not sufficient to bring about that change nor the magnetic field used is strong enough to shift the system to complete ferromagnetic state to see a change in segregation energy (-.42eV).

This thesis provides valuable insights into solute (Mn and C) decoration states and associated mechanism in medium manganese steels and highlights the complex relationship between thermal processing, crystallographic features at the phase boundary and external fields on the solid-state phase transformations and solute redistribution.

Zusammenfassung

Bei Stählen sind Festkörper-Phasenumwandlungen der Schlüssel zum Verständnis der Entwicklung unterschiedlicher Mikrostrukturen und der gewünschten mechanischen Eigenschaften. Diese Phasenumwandlungen gehen in der Regel mit der Umverteilung (Partitionierung) von Elementen von einer Phase in eine andere einher. Bei der Untersuchung von quaternären Systemen (Fe-Mn-Al-C) mit interstitiellen (C) und substituierenden Legierungselementen (Mn, Al) ist es von größter Bedeutung, die drastisch unterschiedliche Diffusionsfähigkeit der Elemente zu berücksichtigen. Der Unterschied in der Diffusionsfähigkeit wird bei der Wärmebehandlung bei niedrigen Temperaturen noch kritischer, da die Diffusion der Substitutionselemente zum geschwindigkeitsbestimmenden Schritt werden kann. Die Behandlung bei niedrigen Temperaturen führt in der Regel zu einem Anstieg der Konzentration der Elemente an der Phasengrenze, was in der Fachliteratur allgemein als Anreicherung an der Phasengrenze bezeichnet wird. Obwohl über die Thermodynamik und Kinetik der Anreicherung an der Phasengrenze viel berichtet wird, sind die Details im Zusammenhang mit den verschiedenen Dekorationszuständen selten. Diese Arbeit konzentriert sich auf die Erforschung und das Verständnis der Grundlagen der Anreicherung und der Dekorationszustände von partitionierenden Elementen (Mangan; Mn, und Kohlenstoff; C) an den Phasengrenzen in Stählen mit mittlerem Mangangehalt

Eine Fe-10Mn-3Al-0,2C-Legierung mit einem Gewichtsprozentanteil von 10 % Mangan wurde einer vollständigen Austenitisierung unterzogen, gefolgt von einer Wasserabschreckung und einem anschließenden interkritischen Glühen, wodurch eine laminierte Mikrostruktur mit einer Kurdjumov-Sachs-Orientierungsbeziehung (KS) zwischen benachbartem Austenit und Ferrit entstand. Die interkritisch geglühte Probe wurde dann 2, 50 und 200 Stunden lang bei niedriger Temperatur (450 °C) angelassen, um die Auswirkungen auf die Anreicherung von Mn und C zu untersuchen.

Eine Untersuchung der Auswirkungen von Korngrenzen auf die Anreicherung von Kohlenstoff an der Phasengrenze ergab, dass Korngrenzen als Senke für Kohlenstoff aus Phasengrenzen fungieren, wenn sie an Tripellinien miteinander verbunden sind. Darüber hinaus wurde kein Unterschied in der Kohlenstoffanreicherung an den Phasengrenzen von KS- und KS-nahen Phasen festgestellt, was ausschließt, dass solche Unterschiede im Phasengrenzcharakter die Hauptursache für eine solche Beobachtung sind, und bestätigt, dass die Korngrenze die Hauptquelle für den Entzug von Kohenstoff aus Phasengrenzen ist.

Weitere Studien zur Untersuchung der Zustände der gelösten Dekorationen an den Phasengrenzen der getemperten Proben ergaben eine lineare Segregation von Mn in der Ebene der Phasengrenze. Diese Dekorationen findet an Fehlpassungsversetzungen in geraden Phasengrenzen und Superleisten in

gekrümmten Phasengrenzen statt. Fehlpassungsversetzungen haben einen gemischten Charakter und Super-ledges sind durch eine Anordnung in einer Ebene in GT-Typ-Orientierung und eine andere Anordnung in Indexebenen mit mehratomigen Facetten gekennzeichnet, die Mn aufgrund ihrer Spannungsenergie und Facettenübergangskonfigurationen anziehen. Im Laufe der Zeit wurde beobachtet, dass Superledges bei 450 °C nach 200 Stunden am schnellsten ein Gleichgewicht mit der umgebenden Matrix erreichten, während dies nicht für Versetzungsfehlpassungen galt. Allerdings haben Phasengrenzbereiche ohne eindeutige Merkmale noch nicht die von DICTRA vorhergesagten Werte für die lokale Gleichgewichtsverteilung erreicht, obwohl sie sich ihnen annähern. Diese Diskrepanz wird auf die anfängliche Quasi-Paraequilibrium-Verteilung zurückgeführt, die im Laufe der Zeit in ein lokales Gleichgewicht übergeht.

Schließlich wurde ein Gedankenexperiment durchgeführt, um die Auswirkungen eines externen Magnetfelds auf die Mn-Segregation an Ferritkorngrenzen zu untersuchen. Dazu wurde eine 50 % kaltgewalzte Fe-8Mn-Legierung verwendet und bei 450 °C 5,5 Stunden lang mit und ohne ein 9-Tesla-Magnetfeld geglüht. Es wurde festgestellt, dass das Magnetfeld keinen Einfluss auf die Mn-Segregation hat. Dies lässt sich dadurch erklären, dass sich der Ferrit ohne externes Magnetfeld bei 450 °C in einem ferromagnetischen Zustand befindet, während sich die Korngrenze in einem paramagnetischen Zustand befindet. Das externe Magnetfeld ändert diesen Zustand nicht wesentlich. Um eine Veränderung im Segregationsverhalten zu beobachten, müssten sowohl der Ferritkörper als auch die Korngrenze in einen paramagnetischen Zustand übergehen, wodurch sich die Segregationsenergie von -0,40 eV (Ferritkörper + paramagnetische Korngrenze) auf -0,1 eV für ein vollständig paramagnetisches System ändern würde. Weder die verwendete Glühtemperatur reichte aus, um diese Veränderung zu bewirken, noch war das verwendete Magnetfeld stark genug, um das System in einen vollständig ferromagnetischen Zustand zu versetzen und eine Veränderung der Segregationsenergie (-0,42 eV) zu bewirken.

Diese These liefert wertvolle Einblicke in die Dekorationszustände von gelösten Stoffen (Mn und C) und die damit verbundenen Mechanismen in Manganstählen mittlerer Zusammensetzung und hebt die komplexe Beziehung zwischen thermischer Verarbeitung, kristallografischen Merkmalen an der Phasengrenze und externen Feldern auf die Festkörper-Phasenumwandlungen und die Umverteilung der gelösten Stoffe hervor.

1. Introduction

1.1 Introduction

Solid-state thermal processing of steel is a key step in achieving multiphase microstructure and diverse mechanical properties [1, 2]. The transformation from the FCC austenite phase to the BCC ferrite phase is particularly significant. This is because these phases are common in a wide range of steels and studying this transformation can provide insights into other related phase transformations, such as bainite or martensite transformations [1-4]. The diffusional mechanism involved in the growth of transformation products is characterized by the partitioning of solute elements, which significantly influences ferrite growth kinetics. Depending on the solubility and diffusivity of solutes, they partition from one phase to another. For example, carbon, being the most prominent solute in steels due to its low solubility and high diffusivity in ferrite, is expelled to the neighboring austenite and must be accounted for when modeling ferrite growth kinetics. However, steels with substitutional alloying (Manganese and Aluminum) elements exhibit an added layer of complexity. The low diffusivity of substitutional species prevents their long-range diffusion, but they do exhibit short-range diffusion near the migrating phase boundary. Various models have been proposed to understand the partitioning of solute elements, namely, local equilibrium negligible partitioning (LENP), local equilibrium partitioning (LEP), and paraequilibrium (PE). The LEP model exhibits full equilibrium at the interface and diffusion of all alloying elements, while the PE model considers no partitioning of substitutional species [5-8]. Furthermore, the energy dissipation caused by the interaction of substitutional species with the phase boundary and their subsequent cross-boundary diffusion retards the boundary migration, a phenomenon termed the solute drag effect. Thus, ferrite growth kinetics is governed by the combined effects of carbon diffusion, crystal structure rearrangement, and the solute drag effect of substitutional elements. It is important to address the contribution of each factor, particularly the influence of substitutional elements on the transformation and kinetics.

One of the most important observations of partitioning behaviour is the presence of a distinct spike in the concentration of diffusing species at the phase boundary [9, 10]. This enrichment at the phase boundary can have multiple origins. Firstly, similar to grain boundary segregation, the driving force for such a spike at the interface is the minimization of the system's total Gibbs energy [11]. Secondly, forced equilibrium at the interface can cause an enrichment of solutes

at the interface. Lastly, the low diffusivity of solutes in either phase leads to a build-up of solutes next to the interface, appearing as enrichment. This nonequilibrium enrichment of solute elements at the phase boundary is called kinetic freezing [10].

Conventional characterization techniques like atom probe tomography (APT) and transmission electron microscopy (TEM), which are generally used to study phase boundary composition, cannot distinguish between the underlying mechanisms governing the enrichment. As a result, composition profiles from region of interest (ROI) analysis in APT or energy dispersive spectroscopy (EDS) in TEM are not sufficient to comment on the phase boundary segregation states. Consecutively, the relative contributions of different mechanisms to boundary enrichment still remain an unexplored subject.

In studies of phase transformations in ferrous alloys, it is widely reported that phase stability can be altered by applying an external magnetic field [12-16]. The ability to manipulate the stability of the parent and product phases presents an intriguing opportunity to control and alter the microstructure for desired strategic applications. Therefore, the combined effect of thermal processing and an external magnetic field has proven to be a robust approach to achieving homogeneous and reproducible microstructures. With the imposition of an external magnetic field, the Gibbs free energy change of the parent phase causes the phase boundaries in the composition vs. temperature space to become a function of the external field strength. Using modern high magnetic field magnets, with flux densities as high as 30T, a free energy change of 360 J/mol can be achieved. Besides the free energy change being comparable to the energy of mixing and ordering energies, crystalline defects with associated small energies, such as stacking faults, twinning, and antisite defects, can also be influenced by strong magnetic fields.

In practical applications, magnetic processing has proven beneficial in achieving parallelly spaced rods aligned along the magnetization direction when processing is undertaken close to the intersection of the Curie temperature and the spinodal instability boundary[17]. Furthermore, an external field promotes the spheroidization of cementite and prevents its directional growth. Additionally, due to the magnetic ordering effect of the field, the recovery of ferrite is delayed [18].

Although significant strides have been made in understanding the effect of external magnetic fields on material properties [19-32], atomic-scale analysis of magnetic processing remains an avenue worth exploring, especially when the alloy contains solutes that favor the product phase while the external magnetic field stabilizes the parent phase.

1.2 Research Objective:

1. To identify chemical decoration states and corresponding thermodynamics in a phase boundary and distinguish the dominant mechanism contributing to enrichment: This will be achieved by comparing the average composition trend obtained from experimental techniques (APT) and comparing it with the diffusion module prediction from DICTRA. The experimental observation will account for both kinetic freezing and equilibrium contribution to segregation values while the simulation form DICTRA will only account for the kinetic freezing and local equilibrium partitioning tendency. This can provide us with comparison and a possible explanation to this conundrum.
2. An experiment to comment on the effect of external magnetic field on the segregation of Mn at α/α grain boundaries: The aim is to anneal a medium Mn binary alloy with and without the presence of magnetic field and study random high angle grain boundaries under atom probe tomography instrument for segregation of Mn and its variation with introduction of magnetic field.

1.3 Thesis Outline

This doctoral thesis is dedicated to understand the fundamentals of Mn and C enrichment at the interfaces in medium Mn steels. Experimental and simulation techniques have been utilized and the outcomes are described as follows:

1. **Chapter 1** introduces the motivation behind undertaking this research project. It provides a brief introduction to the established knowledge regarding partitioning in ferrite growth and magnetic processing and explores possible avenues for enhancements. It also highlights open questions within the existing framework and the approach adopted to address them.
2. **Chapter 2** discusses previously reported works and the prerequisite knowledge needed to understand the subsequent results. Special focus is given to the crystallography of the product phase and the partitioning modes
3. **Chapter 3** briefly describes the experimental techniques utilized for conducting experiments and analyzing the obtained results.
4. **Chapter 4** details the effect of interface character on the enrichment of carbon (C). It observes that the presence of a grain boundary, in conjunction with phase boundaries, has a depleting effect on C enrichment at the phase boundaries. Therefore, it maintains

that commenting on phase boundary enrichment behavior without considering its crystallographic environment can lead to erroneous conclusions.

5. **Chapter 5** deals with phase boundary segregation states where manganese (Mn) is observed to segregate in distinct crystallographic features in the phase boundary plane. For further analysis, diverse characterization techniques and crystallographic analyses are employed. Mn tends to segregate along the misfit dislocations and superledges on straight and curved phase boundaries, respectively. The evolution of segregation along these features over time helps in understanding the partitioning kinetics. Boundaries without any distinct features appear to have the slowest approach to local equilibrium concentration predicted by DICTRA, while the superledges exhibit fast kinetics in achieving local equilibrium concentration.
6. **Chapter 6** describes how an external magnetic field has no influence on the segregation of Mn on ferrite grain boundaries. This is due to the combined effect of annealing temperature and magnetic field strength. Without an external field, the bulk and grain boundary exhibit different magnetic characters; the bulk is ferromagnetic, and the grain boundary is paramagnetic. The introduction of a magnetic field does not change the magnetic state, and consequently, the segregation energy does not change. As a result, no influence on Mn segregation is observed.
7. **Chapter 7** summarizes the outcomes of the experiments and highlights the main conclusions of this research project. Furthermore, it presents an outlook delineating the possible scope of future work, including theories that I plan to explore in the future.

2. Literature Review

2.1 Fe-Mn-Al-C low density steels

Fe-Mn-Al-C steels, originally developed in the 1950s as a replacement for Fe-Cr-Ni steels, are currently garnering significant interest for potential applications in structural components of the automotive industry due to their lighter weight [33]. This class of steels exhibits an impressive combination of superior mechanical performance (ultimate tensile strength: 0.6-2.0 GPa, yield strength: 0.4-1.0 GPa, elongation: 30-100% [34-37]) and density reduction (1.3% density reduction for every 1 wt.% Al [36]). Furthermore, these alloys demonstrate high strength and toughness at both room and cryogenic temperatures [34-37], impressive fatigue properties [38, 39], and improved oxidation resistance at high temperatures [40].

Medium Mn steel is an alloy belonging to the Fe-Mn-Al-C system, characterized by a Mn content of 3-11 wt.% [41, 42]. The stringent regulations concerning weight reduction, fuel economy, and vehicle safety make medium Mn steel a potential candidate for automotive applications [43]. Medium Mn steels offer an improved strength-ductility combination and lower cost. The addition of aluminum aims to suppress the precipitation of cementite and modify the stacking fault energy of the retained austenite, which is present in high fractions in medium Mn steel. The stability and properties of this retained austenite can be altered by alloying element partitioning during the intercritical annealing stage and by the Mn content of the bulk alloy. This further helps in circumventing the overaging of bainite or the quench and partitioning treatment of martensite [42, 44].

Subsequent sections will cover the thermal processing of medium Mn steels, transformation crystallography, and mechanisms associated with the nucleation and growth of transformation products.

2.2 Phase Transformation

Solid-solid phase transformations in steels are categorized into two types: diffusional and displacive transformations. Diffusional transformations are reconstructive in nature, involving the breaking of atomic bonds and their reorganization into a new crystal structure. Displacive transformations, on the other hand, are diffusionless and involve an orderly rearrangement of atoms to form a new crystal structure [2, 3].

When a plain carbon steel is heated, it undergoes the following phase transformation: Ferrite (α-iron) exists below 912°C and has a maximum C solubility of 0.022 wt.% at 727°C. Austenite (γ-iron) can contain up to 2.14 wt.% C at 1147°C and exists between 727°C and 1493°C. For iron (Fe)-C alloys with a C content greater than 0.022 wt.%, the austenite start temperature (Ae1) remains constant at 727°C, while the austenite finish temperature (Ae3) varies from 912°C for pure Fe to 727°C for steels with a C content of 0.8 wt.% [3, 45]. It is worth mentioning that Ae1 and Ae3 are equilibrium transformation temperatures, while the respective non-equilibrium temperatures are denoted as Ac for heating and Ar for cooling. All four temperatures (Ac1, Ac3, Ar1, and Ar3) depend on the alloy composition as well as the heating and cooling rates [3, 46].

During the slow cooling of steels with less than 0.8 wt.% carbon, ferrite is the first phase to nucleate at the triple junctions of austenite grain boundaries through a reconstructive mechanism. It then grows anisotropically along the grain boundaries with an aspect ratio of 1:3 in length, resulting in the formation of allotriomorphic α-ferrite [47].

During rapid cooling, when austenite transforms at low temperatures, a displacive mechanism dominates, resulting in different morphologies. These include Widmanstätten α-plates, intermediate bainite morphology consisting of ferrite plates with embedded cementite particles, and martensite at the lowest temperatures, where no nucleation or growth takes place [47-51]. Subsequently, when martensite is further heated what is achieved is called reverted austenite which nucleates preferentially at the prior austenite grain boundaries and sub-block boundaries [52].

2.2.1 Intercritical annealing

To achieve an extraordinary balance of strength and ductility in medium Mn steel, retention of large amount of austenite is essential. The higher manganese content in medium Mn steel compared to low C TRIP or Q&P steel significantly enhances the thermal stability of austenite, allowing it to be easily retained at room temperature via a robust annealing process. Intercritical annealing (IA), also known as, austenite-reverted-transformation (ART) annealing, is a simple yet effective method for this purpose. This process eliminates the need for subsequent bainite overaging or martensite quenching-partitioning, making it a straightforward and efficient treatment [53-55]. The IA process is currently the most widely used method for heat treating such steels, with a large fraction of retained austenite, as high as ~70%, typically achievable by controlling IA parameters [56-58].

A martensitic structure is preferred before intercritical annealing to achieve a duplex microstructure with ultrafine grain size. Generally, for hot-rolled samples, martensite is usually achieved through quenching [59]. For medium Mn steels, due to their high hardenability, even slow cooling can produce martensite [60]. Prior to cold rolling, samples often possess a diverse combination of features, including ferrite, tempered martensite, retained austenite, or quenched martensite, requiring additional processing steps [61]. After cold rolling, the samples primarily comprise martensite formed from the deformation-induced transformation of austenite [62]. During subsequent annealing treatment, recovery of deformed martensite occurs. If the intercritical annealing temperature is high enough, recrystallization, can also take place. This coupled with increased fraction of austenite result in a decrease in strength and enhanced ductility. One report indicated an intercritical annealing of 1 hour, for medium-Mn steel resulted in 15.7% reversed austenite, appreciable ductility (total elongation of 23%), increased strength (ultimate tensile strength of 815 MPa), and no signs of yield point elongation [63].

2.2.2 Alternate thermal processing methods for medium Mn steels

Apart from intercritical annealing, alternate thermal processing methods have also been proposed, including quench and partitioning (Q&P) [64-67], interrupted quenching followed by intercritical annealing [68], and multi-step annealing [69, 70].

Q&P processing involves four stages: complete or partial austenitization, quenching to form martensite alongside retained austenite, elevated temperature partitioning to enrich the retained austenite with carbon, and a final quench to retain the carbon-enriched austenite. Extending this technique to medium Mn steels promises better strength and ductility, as the high Mn content ensures an increased fraction of the austenite phase rich in carbon.

Authors of references [69, 70] applied multi-step annealing to medium Mn steels by employing repeated martensite formation and reversion of austenite. This routine involved full austenitization followed by quenching to achieve an entirely martensitic microstructure. The steel is then intercritically annealed at a low temperature, followed by fast annealing at a high temperature, a subsequent quench, and finally tempering as the last stage. The aim of these stages was reported as follows: low-temperature annealing enriches the austenite with Mn; high-temperature annealing makes the austenite lean of Mn, which can transform to martensite upon quenching; and tempering enriches the retained austenite with carbon.

As for interrupted quenching and annealing treatment [68], the steel is quenched from austenitization temperature to between Ms and Mf temperature to form martensite and retained

austenite. The retained austenite usually has a lower Mn content than the austenite reversed from martensite during the annealing stage. Upon final quenching, the retained austenite transforms to martensite, while the reversed austenite, enriched with Mn, remains stable. Thus, the final microstructure contains fresh martensite, ferrite, and Mn-enriched austenite.

2.3 Crystallography of transformation products

For low undercoolings, allotriomorphic ferrite exhibits a distinct orientation relationship (OR) with one of the austenite grains [71]. The most commonly observed OR is the Kurdjumov-Sachs (KS) relationship, which follows: $(111)_\gamma||(110)_\alpha$ and $< 110 >_\gamma \; || \; < 111 >_\alpha$ [3, 72]. Another frequently observed OR is the Nishiyama-Wasserman (NW) relationship, characterized by: $(111)_\gamma||(110)_\alpha$ and $< 110 >_\gamma \; || \; < 001 >_\alpha$ [73, 74]. Generally, the nucleated ferrite has either a KS or NW OR with one of the austenite grains and a random orientation relationship with the other grain. The latter is more mobile at higher temperatures, while the former is dominant at lower temperatures [3]. This results in the allotriomorphs having a curved, incoherent phase boundary with one grain and a faceted, partially coherent boundary with the other [75, 76]. For the case of reverted austenite, it is reported to have a sharp surface relief, and maintains a KS OR with the martensite [77, 78]. In the subsequent section different orientation relationships will be discussed in more detail.

2.3.1 The KS orientation relationship

The Kurdjumov-Sachs orientation relationship:

- $(111)_{FCC} || (110)_{BCC}$
- $[110]_{FCC} || [111]_{BCC}$

The KS is most commonly observed ORs in experimental analysis of FCC to BCC transformation. It describes a special alignment where the closed pack plane (111) in FCC aligns perfectly parallel to the closed packed plane (110) in the BCC, and the closed packed direction [110] in FCC parallel to the closed packed direction [111] in the BCC (figure 1.1). Both BCC and FCC structures have high symmetry. Owing to this high symmetry, multiple alignments of FCC and BCC structure exist, in which the KS orientation relationship is preserved. As a result, there exists 24 variants of KS orientation relationship: 4 $(111)_{FCC}$ planes and 6 $(110)_{BCC}$ planes and corresponding direction in these planes that can be aligned.

Variant	Parallel Plane	Parallel Direction
V1	$(111)_{FCC}\|\|(011)_{BCC}$	$[\bar{1}\,0\,1]_{FCC}\|\|[\bar{1}\,\bar{1}1]_{BCC}$
V2		$[\bar{1}\,0\,1]_{FCC}\|\|[\bar{1}\,1\,\bar{1}]_{BCC}$
V3		$[0\,1\,\bar{1}]_{FCC}\|\|[\bar{1}\,\bar{1}\,1]_{BCC}$
V4		$[0\,1\,\bar{1}]_{FCC}\|\|[\bar{1}\,1\,\bar{1}]_{BCC}$
V5		$[1\,\bar{1}\,0]_{FCC}\|\|[\bar{1}\,\bar{1}\,1]_{BCC}$
V6		$[1\,\bar{1}\,0]_{FCC}\|\|[\bar{1}\,1\,\bar{1}]_{BCC}$
V7	$(1\bar{1}1)_{FCC}\|\|(011)_{BCC}$	$[1\,0\,\bar{1}]_{FCC}\|\|[\bar{1}\,\bar{1}1]_{BCC}$
V8		$[1\,0\,\bar{1}]_{FCC}\|\|[\bar{1}\,1\,\bar{1}]_{BCC}$
V9		$[\bar{1}\,\bar{1}\,0]_{FCC}\|\|[\bar{1}\,\bar{1}1]_{BCC}$
V10		$[\bar{1}\,\bar{1}\,0]_{FCC}\|\|[\bar{1}\,1\,\bar{1}]_{BCC}$
V11		$[0\,1\,1]_{FCC}\|\|[\bar{1}\,\bar{1}\,1]_{BCC}$
V12		$[0\,1\,1]_{FCC}\|\|[\bar{1}\,1\,\bar{1}\,]_{BCC}$
V13	$(\bar{1}11)_{FCC}\|\|(011)_{BCC}$	$[0\,\bar{1}\,1]_{FCC}\|\|[\bar{1}\,\bar{1}\,1]_{BCC}$
V14		$[0\,\bar{1}\,1]_{FCC}\|\|[\bar{1}\,1\,\bar{1}]_{BCC}$
V15		$[\bar{1}\,0\,\bar{1}]_{FCC}\|\|[\bar{1}\,\bar{1}\,1]_{BCC}$
V16		$[\bar{1}\,0\,\bar{1}]_{FCC}\|\|[\bar{1}\,1\,\bar{1}]_{BCC}$
V17		$[1\,1\,0]_{FCC}\|\|[\bar{1}\,\bar{1}\,1]_{BCC}$
V18		$[1\,1\,0]_{FCC}\|\|[\bar{1}\,1\,\bar{1}]_{BCC}$
V19	$(11\bar{1})_{FCC}\|\|(011)_{BCC}$	$[\bar{1}\,1\,0]_{FCC}\|\|[\bar{1}\,\bar{1}\,1]_{BCC}$
V20		$[\bar{1}\,1\,0]_{FCC}\|\|[\bar{1}\,1\,\bar{1}]_{BCC}$
V21		$[0\,\bar{1}\,\bar{1}]_{FCC}\|\|[\bar{1}\,\bar{1}\,1]_{BCC}$
V22		$[0\,\bar{1}\,\bar{1}]_{FCC}\|\|[\bar{1}\,1\,\bar{1}]_{BCC}$
V23		$[1\,0\,1\,]_{FCC}\|\|[\bar{1}\,\bar{1}\,1]_{BCC}$
V24		$[1\,0\,1\,]_{FCC}\|\|[\bar{1}\,1\,\bar{1}]_{BCC}$

Table 2.1 The KS orientation relationship with 24 variants

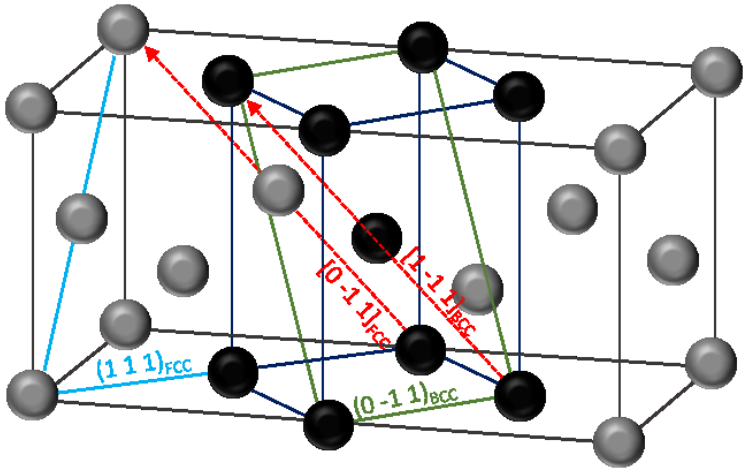

Figure 2.1 Schematic diagram illustrating KS orientation relationship.

2.3.1.1 Mathematical representation

FCC (γ) orientation matrix 'A' can be expressed as:

$$A = [[1\ 1\ 1]_{\mathrm{FCC}} \quad [\bar{1}\ 0\ 1]_{\mathrm{FCC}} \quad [1\ \bar{2}\ 1]_{\mathrm{FCC}}]$$

The BCC (α) orientation matrix 'M' can be expressed as:

$$M = [[0\ 1\ 1]_{\mathrm{BCC}} \quad [\bar{1}\ \bar{1}1]_{\mathrm{BCC}} \quad [2\ \bar{1}\ 1]_{\mathrm{BCC}}]$$

The unit vectors for FCC:

$$[1\ 1\ 1]_{\mathrm{FCC}} = \frac{1}{\sqrt{3}}\begin{bmatrix}1\\1\\1\end{bmatrix}, \qquad [\bar{1}\ 0\ 1]_{\mathrm{FCC}} = \frac{1}{\sqrt{2}}\begin{bmatrix}-1\\0\\1\end{bmatrix}, \qquad [\bar{1}\ 2\ 1]_{\mathrm{FCC}} = \frac{1}{\sqrt{6}}\begin{bmatrix}1\\-2\\1\end{bmatrix}$$

The unit vectors for BCC:

$$[0\ 1\ 1]_{\mathrm{BCC}} = \frac{1}{\sqrt{2}}\begin{bmatrix}0\\1\\1\end{bmatrix}, \qquad [\bar{1}\ 1\ 1]_{\mathrm{BCC}} = \frac{1}{\sqrt{3}}\begin{bmatrix}-1\\-1\\1\end{bmatrix}, \qquad [\bar{1}\ 2\ 1]_{\mathrm{BCC}} = \frac{1}{\sqrt{6}}\begin{bmatrix}2\\-1\\1\end{bmatrix}$$

Thus, the FCC (A) and BCC (M) orientation matrix becomes:

$$A = \begin{bmatrix}\frac{1}{\sqrt{3}} & \frac{-1}{\sqrt{2}} & \frac{1}{\sqrt{6}}\\ \frac{1}{\sqrt{3}} & 0 & \frac{-2}{\sqrt{6}}\\ \frac{1}{\sqrt{3}} & \frac{1}{\sqrt{2}} & \frac{1}{\sqrt{6}}\end{bmatrix}, \qquad M = \begin{bmatrix}0 & \frac{-1}{\sqrt{3}} & \frac{2}{\sqrt{6}}\\ \frac{1}{\sqrt{2}} & \frac{-1}{\sqrt{3}} & \frac{-1}{\sqrt{6}}\\ \frac{1}{\sqrt{2}} & \frac{1}{\sqrt{3}} & \frac{1}{\sqrt{6}}\end{bmatrix}$$

In order to calculate the transformation matrix, $T_1 = MA^{-1}$

$$T_1 = \begin{bmatrix}0 & \frac{-1}{\sqrt{3}} & \frac{2}{\sqrt{6}}\\ \frac{1}{\sqrt{2}} & \frac{-1}{\sqrt{3}} & \frac{-1}{\sqrt{6}}\\ \frac{1}{\sqrt{2}} & \frac{1}{\sqrt{3}} & \frac{1}{\sqrt{6}}\end{bmatrix}\begin{bmatrix}\frac{1}{\sqrt{3}} & \frac{1}{\sqrt{3}} & \frac{1}{\sqrt{3}}\\ \frac{-1}{\sqrt{2}} & 0 & \frac{1}{\sqrt{2}}\\ \frac{1}{\sqrt{6}} & \frac{-2}{\sqrt{6}} & \frac{1}{\sqrt{6}}\end{bmatrix} = \begin{bmatrix}\frac{\sqrt{6}+3}{3\sqrt{6}} & \frac{-2}{3} & \frac{\sqrt{6}-3}{3\sqrt{6}}\\ \frac{2\sqrt{6}-1}{6} & \frac{\sqrt{6}+3}{3\sqrt{6}} & \frac{-1}{6}\\ \frac{1}{6} & \frac{3-\sqrt{6}}{3\sqrt{6}} & \frac{2\sqrt{6}+1}{6}\end{bmatrix}$$

Similarly, translation matrix can be identified for other 23 variants as well.

In practice, a sample seldom possess KS orientation relationship in entirety, Austenite grains are found to have from ideal KS to NW and Pitsch orientation relationship as well. Table 1.1 describes different orientation relationships observed between FCC and BCC crystals.

Name	Orientation Relationship	Number of Variants	<Axis>angle
Bain (B) [79]	$\{100\}_{\gamma} \parallel \{100\}_{\alpha}$ $<100>_{\gamma} \parallel <110>_{\alpha}$	3	<100>45
Kurdjumov-Sachs (KS) [80]	$\{111\}_{\gamma} \parallel \{110\}_{\alpha}$ $<110>_{\gamma} \parallel <111>_{\alpha}$	24	<0.97 0.18 0.18>42.85
Nishiyama Wasserman (NW) [81]	$\{111\}_{\gamma} \parallel \{110\}_{\alpha}$ $<112>_{\gamma} \parallel <111>_{\alpha}$	12	<0.98 0.08 0.20>45.98
Pitsch (P) [82]	$\{100\}_{\gamma} \parallel \{110\}_{\alpha}$ $<110>_{\gamma} \parallel <111>_{\alpha}$	12	<0.08 0.20 0.98>45.98
Greninger-Troiano (GT) [83]	$\{111\}_{\gamma} \parallel \{110\}_{\alpha}$ $<123>_{\gamma} \parallel <133>_{\alpha}$	24	<0.97 0.19 0.13>44.23
Greninger-Troiano' (GT') [83]	$\{110\}_{\gamma} \parallel \{111\}_{\alpha}$ $<133>_{\gamma} \parallel <123>_{\alpha}$	24	<0.19 0.97 0.13>44.23

Table 2.2 Different orientation relationship with their characteristics: parallel plane and directions, variants and angle axis constraint.

Bain OR represent the simplest OR in material systems, but it is never observed for steels. As a result, is it used as a first approximation when FCC to BCC transformation is studied. KS and NW ORs are most commonly observed and widely studied, but considering a small angular difference between these two orientations, experimental validation on which is the most dominant OR is a bit difficult. Greninger-troiano (GT) and GT' are irrational ORs. When an orientation relationship cannot be expressed by low index {hkl}<uvw>, it is termed as an irrational orientation relationship [84].

2.4 Kinetics of austenite (γ) nucleation and growth

Austenite formation is a diffusion-controlled phenomenon, that involves nucleation and growth [85-90]. The nucleation site depends on the starting microstructure of the steel. For hypoeutectoid steels, the pearlite/ferrite phase boundary hosts the austenite nuclei [85, 90]. In martensitic steels, martensitic laths or packets [87-89] and prior austenite grain boundaries aid in nucleating the fresh austenite nucleus [88, 91]. In steels with a tendency to form carbides, the carbide particles themselves form the nuclei for austenite [86, 90]. However, this phenomenon is limited to grain boundary carbides, while carbides within the grain interior dissolve into the matrix to supply carbon for austenite [90].

When it comes to austenite growth, it further comprises three steps [85, 86, 92-95].

1. Nucleation of austenite and growth aided by carbide dissolution.
    a. Experimentally not resolvable as pace of growth is very rapid.

b. Characterized by high C diffusivity

2. Austenite growth into neighboring ferrite to attain partial equilibrium.
    a. Intermediate speed of growth
    b. Rate controlling step:
        i. High temperature: C diffusion in austenite
        ii. Low temperature: Mn diffusion in ferrite
3. Complete equilibrium between austenite and ferrite
    a. Glacial growth
    b. Rate controlling step: sluggish diffusion of Mn in austenite

The formation kinetics of austenite also strongly depend on the initial microstructure. The austenitization rate increases in the following range of microstructures: ferrite with carbide precipitates, ferrite/pearlite, martensite, and cold-rolled microstructure [96].

2.5 Kinetics and thermodynamics of ferrite (α) formation

Since nucleation of ferrite has been widely discussed, in this section main focus will be given on ferrite growth.

2.5.1 Interface controlled growth

During ferrite growth stage, lean alloyed steels exhibit interface-controlled growth, where the mutually exclusive atomic transfer across the interface takes place [97]. The interface itself as a result becomes a barrier to transfer and needs overcoming through an activation energy ΔG [97].

For atomic jump frequency F, by which an atom crosses the interfaces is expressed as:

$$F_{\alpha\gamma} = v exp(\frac{\Delta G}{kT})$$

v is the characteristic frequency. Frequency of jump in the opposite direction i.e. from α to γ phase is given by equation:

$$F_{\gamma\alpha} = v exp(-\frac{\Delta G^{*} + \Delta G^{\alpha\gamma}}{kT})$$

The difference between the two equations gives the net transfer rate of atoms across the interface. By using the width of the interface d_b, the velocity of interface cab be obtained. For very low transformation driving force, $\Delta G^{\alpha\gamma} \ll kT$, the equations take the form [97]:

$$V_{interface} = \frac{v d_b \Delta G^{\alpha\gamma}}{kT} \exp\left(\frac{-\Delta G^*}{kT}\right)$$

This can be further simplified to [4142]:

$$V_{interface} = M^B \Delta G(T)$$

M^B corresponds to mobility of the interface and $\Delta G(T)$ is the free energy change per atom. This further help us conclude that velocity of the interface is a product of mobility and driving force [97]. The mobility is dependent upon the temperature and assumes the following form:

$$M^B = M_o \exp\left(\frac{-Q}{RT}\right)$$

M_o stands for preexponential factor, Q is atomic jump activation energy, R is gas constant and T is the temperature in consideration.

2.5.2 Diffusion controlled growth

In alloys with a considerable quantity of solute elements having differing solubilities in adjacent phases, the diffusion of elements away from the interface becomes the rate-controlling step [97]. The earliest model for understanding diffusion-controlled growth was proposed by Zener [98] for the growth of spherical precipitates. Diffusion-controlled growth is quite straightforward to explain for binary alloys, where it is assumed that local equilibrium is maintained at and near the interface. Hence, the tie-line operations provide the composition of phases on either side of the interface. However, this treatment is insufficient when the alloying elements have significantly different diffusivities. Various models have been proposed to understand the growth of ternary or quaternary alloy systems, which are discussed below.

2.5.2.1 Paraequilibrium (PE)

Alloys with composition Fe-C-X-Y, requires defining the diffusion of C (interstitial) and element X and Y (substitutional) simultaneously and the diffusion equation becomes [3, 6]:

$$(C_i^{\gamma} - C_i^{\alpha})v = -D_i \nabla C_i$$

i = C, X or Y. Difference in the diffusion coefficient between C and other elements results in a situation where selecting correct tie lines on a phase diagram becomes complex [6]. In order to simplify the understanding, one element is considered to diffuse rapidly (C in this case, as it is interstitial) and other element (most probably a substitutional) has sluggish diffusion throughout the experiment. This phenomenon of partial equilibrium is termed as paraequilibrium (PE). The tie lines depicted in figure identify equal Fe/X ratio compositions

and chemical potential of C staying stagnant across the phase boundary [7, 99]. Subsequently, diffusion of C or other interstitial elements becomes the rate determining step [8].

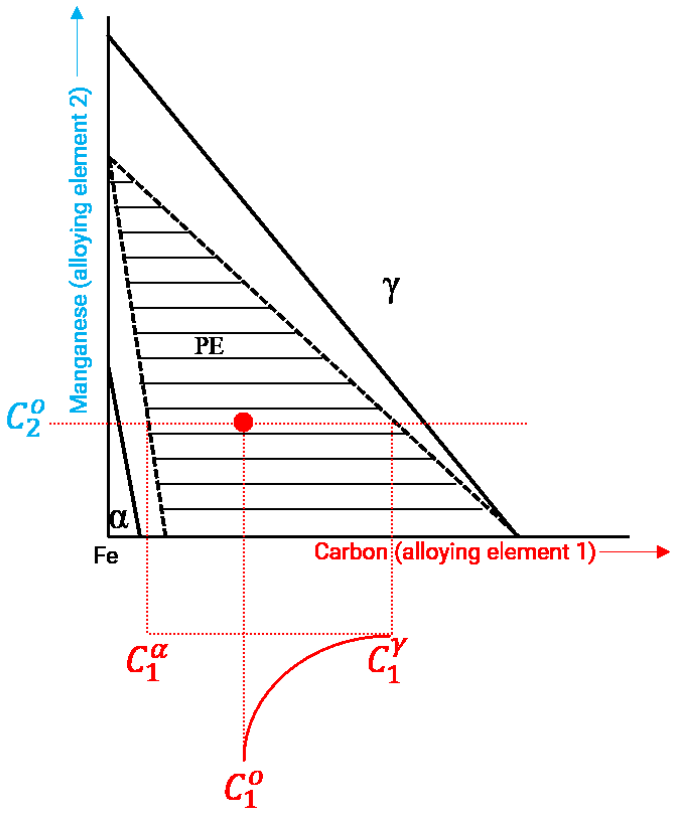

Figure 2.2: Schematic diagram of phase boundary composition, and diffusion profile for paraequilibrium condition from a plane of a quaternary system Fe-C-Mn-Al.

2.5.2.2 LEP (Local equilibrium with partitioning) and LENP (local equilibrium with negligible partitioning)

The approach is to find the tie line such that at the migrating interface mass balance of C and X is preserved [5, 100]. For this, the isotherm is divided into two section namely LEP and LENP with the boundary defined as zero partition envelope [101]. Above the line, the α growth is associated with long-range redistribution of C and X in both α and γ. Subsequently giving growing α phase the name partitioned α as the diffusion kinetics is controlled by mobility of substitutional element (X). The composition of X identified by LE approach is used in mass balance equation and α growth kinetics defined by this way is known as local equilibrium with partitioning.

For the section below the zero-partitioning envelope, is usually considered for high undercoolings, where maintaining LE is thermodynamically feasible but only C exhibits a long-range redistribution. Since substitutional elements are redistributed, C diffusion becomes the

rate controlling factor for α growth. The C content at the phase boundary can be obtained by using the tie-line and by employing the mass balance equation to understand non-partitioned α-growth kinetics [102].

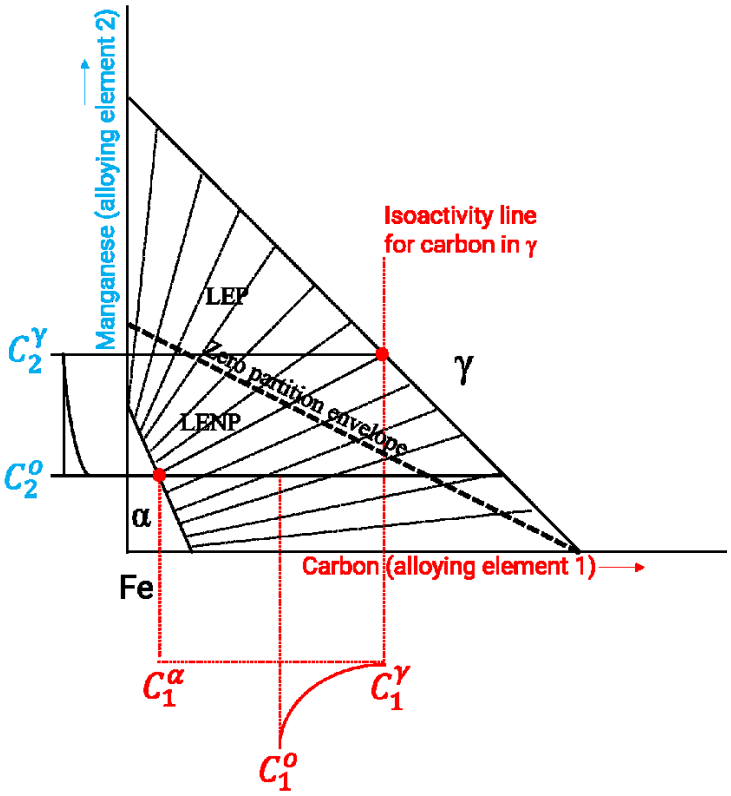

Figure 2.3: Schematic diagram of phase boundaries and composition and corresponding diffusion profile for LEP and LENP condition from a plane of a quaternary system Fe-C-Mn-Al.

2.6 Partitioning of solutes and interface enrichment

A common observation made during partitioning is a spike in the concentration of diffusing species, at the phase boundary [9, 103-107]. This concentration spike has multiple origins and its subsequent effects. Firstly, the most general approach to understanding the spike stems from the idea of grain boundary segregation, which is the Gibbs energy minimization of the system, also termed equilibrium segregation. This solute enrichment at the phase boundaries is further dependent upon the element in question and the phase boundary character, i.e. coherent, semi-coherent and incoherent. More details regarding boundary character and its relationship to segregation is discussed in chapter 4. Secondly, a less widely discussed mechanism, is non-equilibrium segregation originating from solute-vacancy complex formation. Lastly, a combined effect of the requirement to maintain thermodynamic equilibrium at the phase boundary and slow diffusivity in at least one of the adjacent phases results in an elemental

composition at the interface, that is much higher than the equilibrium concentration of solutes in either phase. This phenomenon of incomplete partitioning kinetics, is also known as kinetic freezing [10].

2.6.1 Effects of solute enrichment

2.6.1.1 As Solute drag effect

One of the most interesting outcomes of solute enrichment at phase boundaries is the solute drag effect (SDE), which further slows down the transformation kinetics [71, 108-112]. The SDE is an extension of the theory developed to describe the retardation of grain boundary velocity by the addition of solute elements [113, 114]. Subsequent theories by Purdy and Brechet [115] explained SDE in terms of energy dissipation and its relation to interface velocity, asserting that energy dissipation is maximum at intermediate interface velocity. Later theories by Enomoto [116], incorporated the co-segregation concept into the SDE model and reported the enhancement of the enrichment of X (substitutional elements) due to the attractive interaction between X and carbon [71]. The parameters used in defining the solute drag effect (SDE) in moving boundary problems include dissipation energy, segregation energy of C, X, and Y, diffusivity of X and Y at the phase boundary, phase boundary thickness, velocity, and the mutual interaction parameter between solute elements. Accurate prediction of these parameters is still required. Therefore, even though these models hold considerable credibility, proper calibration with experiments is very important.

2.6.1.2 In practical applications

In practical experience, if manganese (Mn) segregation at the grain boundaries is sufficient to initiate the nanoscale nucleation of austenite, it helps release the elastic stresses in martensite and aids in achieving tough and ductile martensite [117]. In the case of phase boundaries, carbon (C) segregation at the phase boundary obstructed the emission of phase boundary dislocations, thereby increasing the activation stress for dislocation nucleation and subsequently affecting plastic deformation [9]. Dislocations in the ferrite grain interiors also exhibit Mn segregation, with compositions corresponding to the equilibrium concentration of Mn in austenite at that temperature. Multiscale model-based thermodynamic calculations concluded that this austenite is defect-stabilized and subcritical, and can be referred to as complexions [118].

As opposed to grain boundaries, where literature concerning segregation and associated thermodynamics and kinetics is widely available [114, 119-137], the same cannot be said for

phase boundaries, and studies on the decoration states of these boundaries are even more limited. The primary objective of my research is to enhance the existing framework and expand the current literature by providing new insights and findings.

3. Materials and methods

3.1 Alloy synthesis

The casting of Fe-10Mn-3Al-0.2C wt.% medium Mn steel was performed in a vacuum induction furnace. The steel ingots were then reheated to 1,230°C and hot rolled to ~3 mm to above 750°C, followed by air cooling to room temperature. The hot-rolled plates consisted of a predominantly martensitic structure. The hot-rolled plates were then tempered at 500°C for 2 hours to soften the material, after which cold rolling with a thickness reduction of approximately 50% was performed.

The casting of Fe-8Mn wt.% binary alloy was done in a vacuum induction furnace. Hot rolling was conducted at 1100°C from 60 to 6 mm, followed by oil quenching. The hot-rolled plates were subsequently solution annealed at 1100°C for 3 hours. The solution-annealed samples were cold rolled to achieve a 50% reduction in thickness.

3.2 Methods

3.2.1 Electron backscatter diffraction (EBSD)

The heat-treated samples were cut in half, and the center of the specimens was ground using carbide sandpaper (400-1200 grit size). Subsequently, the samples were subjected to diamond paste polishing with 3µm size particles. Final polishing was carried out with an oxide polishing suspension.

A Zeiss Sigma 500 field emission scanning electron microscope (SEM) with a Hikari EBSD detector and a Zeiss Gemini 450 equipped with a Velocity EBSD detector were used for analysis. OIM Analysis 8 software was used for post-processing the EBSD scans.

3.2.2 Scanning electron microscope-focused ion beam (SEM-FIB)

Tips for atom probe analysis and transmission electron microscopy (TEM) were prepared using a FEI Helios NanoLab 660i SEM-focused ion beam.

3.2.4 Atom probe tomography (APT)

Composition analysis was conducted using a LEAP 5000XR HR with a reflectron and a 5000XS (Cameca instrument) at 60 K, in laser pulsing mode with a frequency of 200 kHz and

a pulse energy of 40 pJ. The reconstruction of the raw data was done using AP Suite, version 6.3.1.

3.2.5 Transmission electron microscopy (TEM)

TEM studies were conducted in a probe-corrected Titan Themis 80-300 (Thermo Fischer Scientific) with an accelerating voltage of 300 kV. Composition analysis was done using four in-column Super-X detectors with a beam current of 120 kV. The instrument was operated by Dr. Vivek Devulapalli.

3.2.6 Thermodynamic calculations

Thermodynamic parameters, such as chemical composition and Gibbs energy of phases for different annealing or tempering temperatures, were extracted by Thermo-Calc (2024b) using the TCFE9 database. The composition evolution during the tempering and annealing process was simulated using the MOBFE6 mobility database in DICTRA, Thermo-Calc 2024b.

3.2.7 Magnetic measurements

Annealing in the presence of a magnetic field was conducted using the Quantum Design Magnetic Property Measurement System (MPMS) with the standard Vibrating Sample Magnetometry (VSM) option.

4. Effect of interface character and misorientation on C and Mn segregation

4.1. Introduction

Solute segregation in metallic materials is often described as the local enrichment in the composition at interfaces (typically grain and phase boundaries), defects, or free surfaces [9, 118, 138, 139] . Thermodynamically, the interaction of solute atoms with various lattice defects lowers the Gibbs free energy of the system, thus facilitating the segregation of solutes. Such segregation can be controlled through specific thermomechanical treatments, which can result in substantial changes in mechanical properties such as strength and fracture toughness [117, 131]. The microstructure strategy of utilizing chemical segregations to improve material's mechanical performance is termed as segregation engineering. One typical metallic material that can benefit from such microstructure approach is steel which represent ~90% of the global metallic alloy market. To give an example, C segregation at ferrite grain boundaries has been reported to be beneficial for grain boundary strengthening due to is increasing effect on the Hall-Petch coefficient [119, 140, 141]. Segregation of manganese (Mn) at the martensitic grain boundaries of a Fe-9Mn steel was established to induce nano-scale austenite nucleation which thereby improved ductility and toughness [117].

There are some distinct differences between phase boundaries and random high-angle grain boundaries. Firstly, while a grain boundary (GB) is an interface separating two crystals of the same lattice structure and composition, a phase boundary (PB) is the junction of two crystals of dissimilar crystal structures and compositions [142]. This discrepancy in the environment of the interfaces influences their chemistry and structure, which further affects the solute decoration state at these interfaces. Secondly, unlike random high-angle grain boundaries, phase boundaries present a higher concentration of stress/strain owing to usually considerable mechanical contrast between the abutting phases [143-145]. These two differences are likely to result in different segregation driving forces and thus different segregation amount and kinetics for certain elements, which might give rise to solute competition when the two types

of interfaces coexist in one material. These points are yet to be investigated to enable a better control of interface segregation for improved mechanical properties.

Coherency at the phase interface has been traditionally used to distinguish among different boundary types. The presence of identical atomic arrangements both at the interface plane and throughout the continuous atomic planes across the boundary, either naturally or through imposition (in case of small misfit), resulting in a coherent interface. For large misfits the boundary comprises of regions of both coherency and disregistry. When the regions of disregistry are sufficiently close that coordination between interfacial atoms is lost, and the arrangement of atoms at the boundary resembles that of a liquid state, it is termed an incoherent interface. A fully coherent phase boundary can be differentiated from a semi-coherent phase boundary by identifying a linear misfit defect, usually a dislocation loop. This can be further understood by the fact that coherent precipitates cease to produce a strong diffraction contrast when a set of dislocation misfit dislocation loops is inserted at the phase boundary [97, 142, 146-148].

The energy of the boundary varies as its coherency changes. In the case of a phase boundary, this energy is defined as the difference in free energy between a system consisting of two adjacent crystals with different compositions and crystal structures and the average free energies of the two phases, each occupying the same volume as the system including the boundary [142]. As is the case with surface energy influencing the heats of sublimation and grain boundary energy affecting heat of fusion, energy of phase boundary will inevitably be influenced by solute segregation in the semi and incoherent boundaries [149]. In practical applications, not all the interfaces exhibit a semi-coherent or coherent character, but rather have a spectrum of orientation relationships or even random orientation relationships. Reported data shows significant scatter around KS OR [150, 151]. This scatter in habit plane and OR is smaller in fcc/bcc interfaces in substitutional alloys than for interstitial ones [152-155]. The reasons for observed scatter in orientation relationship (OR) within a sample can stem from the minimization of interfacial energy, the interaction between the critical nucleus and the nucleation site, as well as elastic and plastic constraints imposed on the interfaces when they form under non-equilibrium conditions [156-158]. With the scatter and deviation from perfect OR, it is safe to say that the phase boundaries can present a wide range of interfacial energy associated with their surfaces. This varying interfacial is likely to cause varying segregation driving forces, leading to different segregation amounts and kinetics for certain elements. Thus,

the study of orientation dependent segregation is more valuable as it can help in correlating the reported phase boundary energies and elemental segregation tendencies.

Here, C and Mn segregation behavior at the ferrite/austenite phase interface of a two-phase medium Mn steel will be presented. By employing correlative TKD-APT and 4D-STEM-APT techniques, a significant difference in enrichment behavior of the two elements was observed based on ORs.

4.2. Methods

A medium Mn steel with a chemical composition of Fe-10Mn-3Al-0.2C (wt.%) was selected for this investigation. After austenitization (1000°C-30min), followed by intercritical annealing (700°C-30min) and tempering (450°C-2h) treatments, an ultrafine ferrite-austenite laminated microstructure is obtained (as shown in figure. 4.1a) in which almost all, if not every, phase boundary possesses a Kurdjumov-Sachs (KS) orientation relationship (OR), as depicted in figure. 4.1(b). I used atom probe tomography (APT) to study the carbon (C) segregation behavior at different types of interfaces which primarily occurs during the tempering treatment.

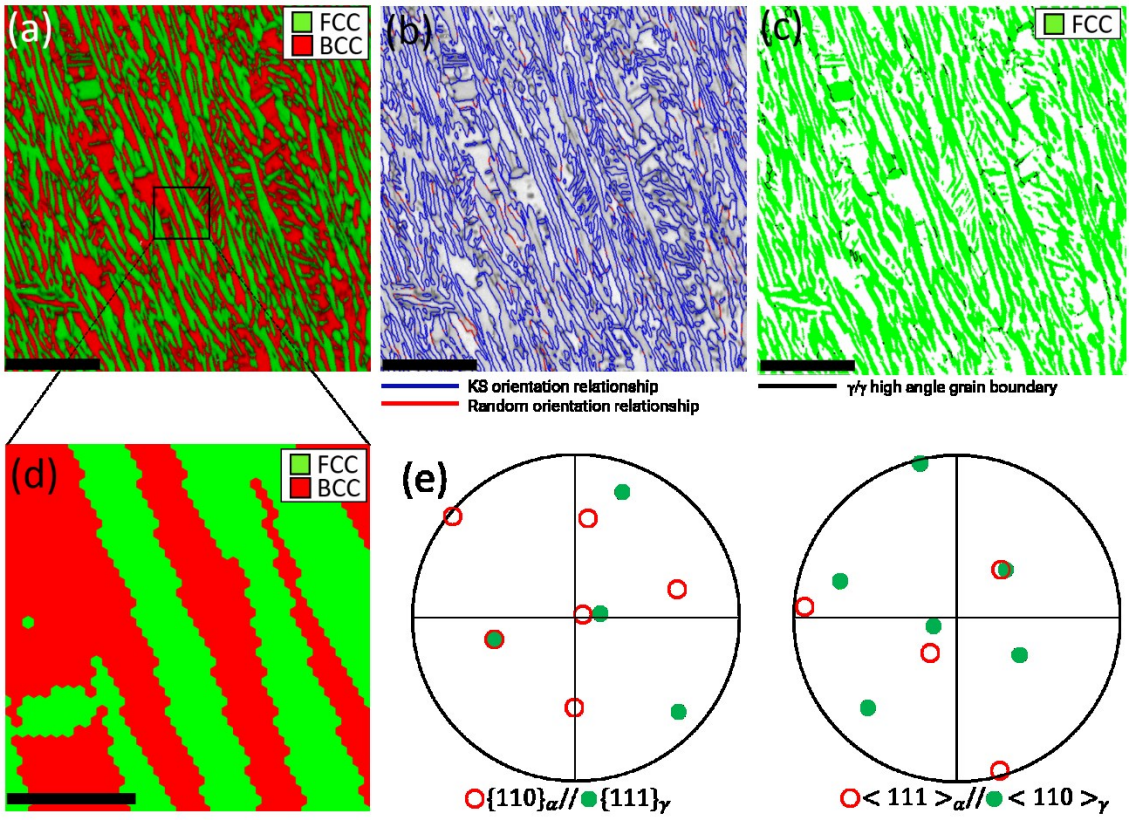

Figure 4.1 (a) Electron backscatter diffraction (EBSD) phase plus image quality map showing the microstructure of the investigated medium Mn steel heat treated at 450°C for 2 hours; (b) Interface plus IQ map showing highlighted phase boundaries possessing a Kurdjumov-Sachs (KS) orientation

relationship (blue) and no specific orientation relationships (red), (c) Austenite phase map showing γ/γ high angle grain boundaries (black), (d) Magnified phase map taken from the rectangular frame marked in (a), showing a detailed microstructure of laminated austenite and ferrite microstructure and; (e) Pole figure confirming the existence of KS orientation relationship between austenite and ferrite phases shown in (d). Scale in (a,b,c) is 5μm and in (d) is 500nm.

4.3 Results and discussion

4.3.1 Phase boundary composition analysis

Figure. 4.2(a) exhibits the C distribution map obtained from the APT analysis, where C-rich regions with a concentration of ~1 at.% correspond to austenite (γ iron), and C-depleted regions (concentration ~0.3 at.%) correspond to the ferrite (α iron) phases. A clear C enrichment is observed at both the γ-α phase boundary (PB1) and γ-γ grain boundary (GB1, figure. 4.2 a and b). Representative one-dimensional C profiles across these two interfaces reveal a different segregating amount: a peak value of 1.71 at.% and 2.75 at.% for the region of interest pertaining to PB1 and GB1, respectively (figure. 4.2b). However, we observe that not all the phase boundaries are enriched with C. The other phase boundary, marked as PB2 in this APT dataset, shows a complete absence of C enrichment (figure. 4.2a and c).

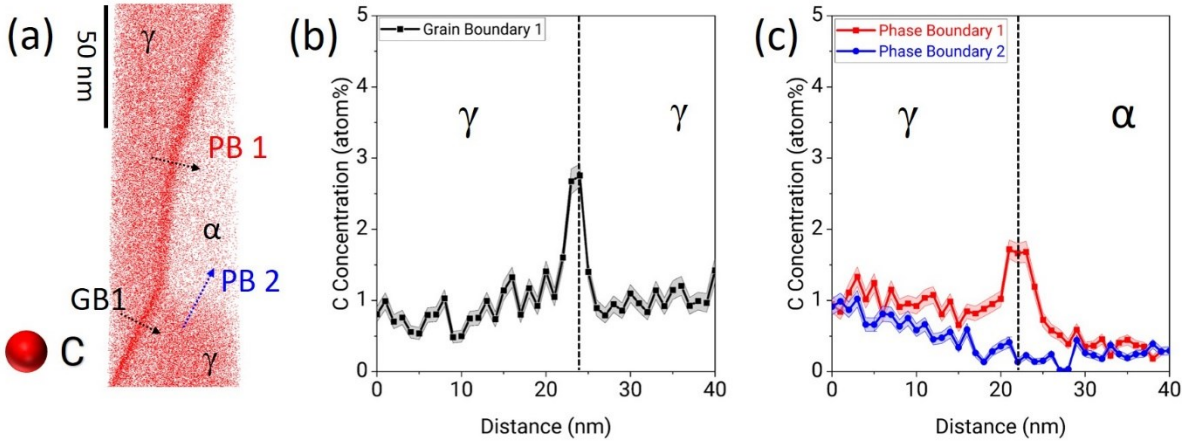

Figure 4.2 (a) APT carbon distribution map; GB represents grain boundary and PB represents phase boundary; One-Dimensional dimensional (1D) composition profile along (b) the γ/γ grain boundary (GB) and (c) two and α/γ phase boundaries (PB1 and PB2); ø=15nm for the ROIs drawn along PB1, PB2 and GB.

4.3.2 In-plane composition analysis

The discrepancy in the C segregating amount also exists among different local regions within one interface. Such heterogeneous C segregation behavior along interfaces can be visualized

through an in-plane C distribution analysis that was conducted using an open-source machine learning code [159]. The analysis employed convolutional neural network for recognizing interfaces in APT dataset, thereby introducing meshes in the boundaries and computing chemical composition within each mesh. The results containing PB1, GB1 and the associated triple junction are presented in figure. 4.3. It is visible from the two-dimensional C concentration mapping that even though there is an overall enrichment of C at PB1 compared to the abutting matrix, a decreasing trend of C segregation can be observed close to the triple junction (figure. 4.3b). In order to quantify the in-plane segregation behavior, the interface was divided into sections, and the average C content was calculated for each section and plotted in figure. 4.3(c). It is shown that the C enrichment level reduces continuously from ~2 at.% at the farthest end (~120 nm) away from the triple junction to ~1.15 at.% close to the triple junction. In contrast for the grain boundary (GB1), the amount of C enrichment increases when the location is closer to the triple junction (figure. 4.3c).

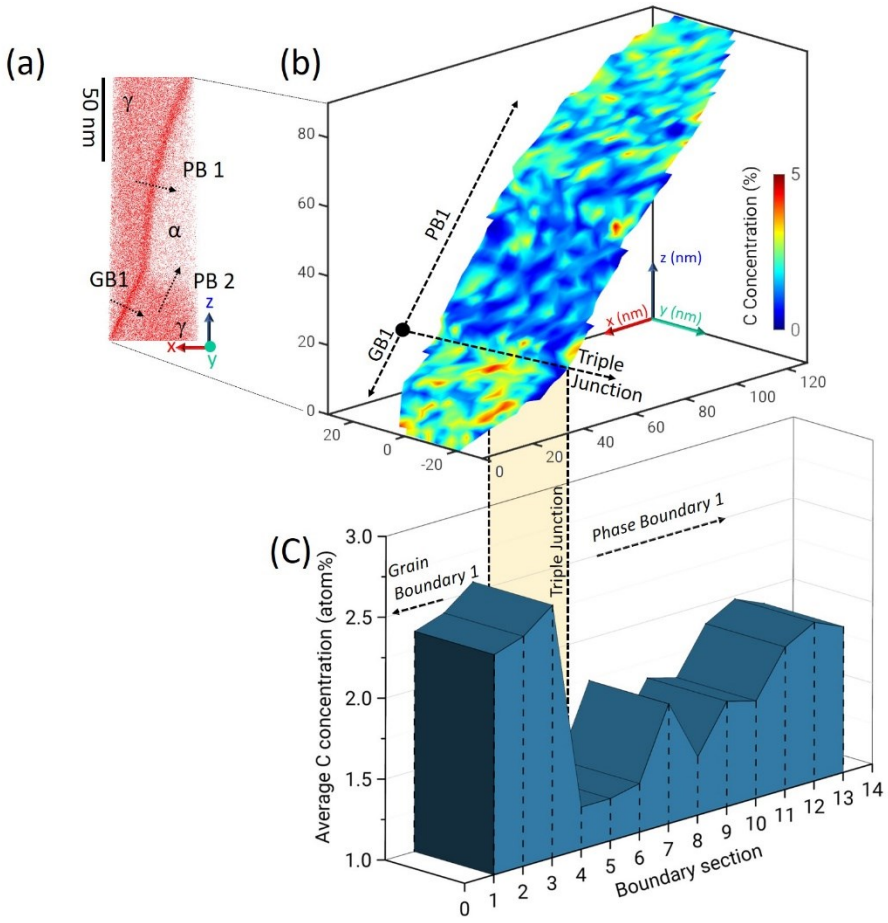

Figure 4.3 (a) Carbon distribution map, (b) 2D representation of in-plane C distribution along the interfaces PB1 and GB1, (c) Average C concentration in different sections of the phase and grain boundary.

The above analysis reveals a rather different and heterogeneous C segregation behavior, not only among different interfaces (e.g. GB1 and PB1, PB1 and PB2), but also among different locations within one interface. Such phenomenon is attributed to the different interfacial energy of different types of interfaces, which leads to different segregating potentials for C and thus the competition among different segregation sites. It has been reported in pure Fe, Fe-Cu and Ni-Cr alloys that the interfacial energy of semi-coherent interfaces is substantially lower than that of incoherent interfaces (250-400 mJ/m2 vs. 500-1000 mJ/m2) [160] [19]. Having mentioned that most of the phase boundaries presented in the investigated material have a coherent or near-coherent character, it is expected for them to show lower enrichment of C as compared to grain boundaries. From the above observation it appears that grain boundary acts as an extracting agent of C from the phase boundaries.

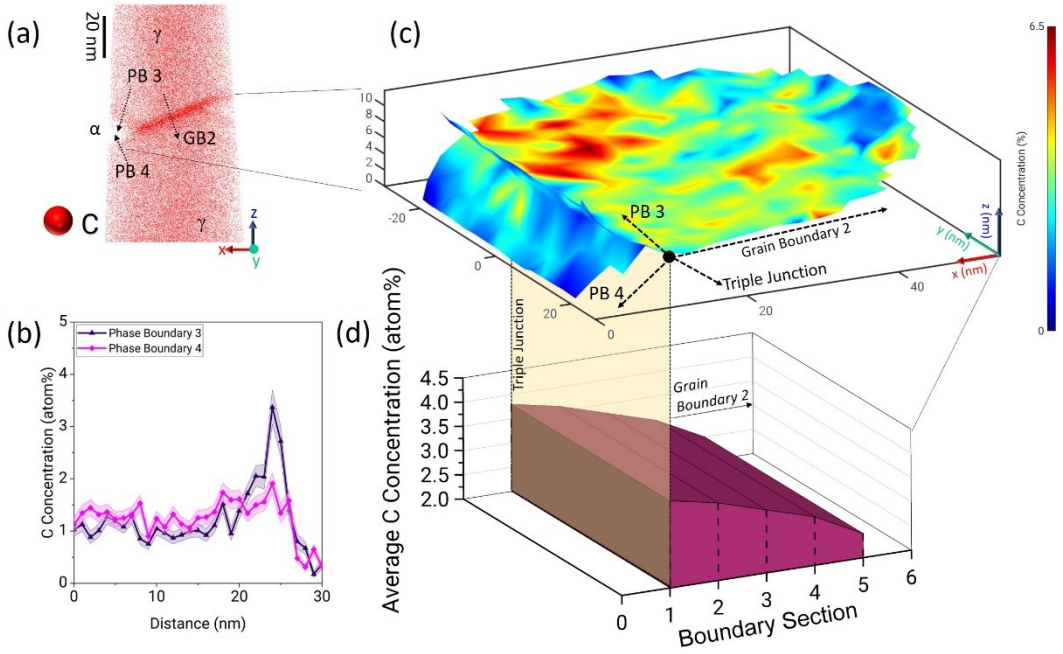

Figure 4.4 (a) Carbon distribution map, (b) 1D composition profile along two α/γ phase boundaries (PB3 and PB4; ROI: ϕ=10 nm), (c) 2D representation of in-plane C distribution along the interfaces PB3, PB4 and GB2, (d) Average C concentration in different sections of the phase and grain boundaries.

The above observation of grain boundary acting as an extracting agent for C is not an isolated event. A similar behavior is seen in triple junctions observed in samples that are tempered for 50 hours as well (figure 4.4). It is evident that PB3 has a clear spike in concentration of Mn at the phase boundary but such spike is absent for PB4. Only a concentration gradient is present at the interface. In-plane composition analysis further helped in realizing the C distribution

along the entire grain boundary plane: It reveals similar to the previous results a higher concentration of C near the triple junction. This further supports our hypothesis that the grain boundary can act as a sink for C specially when a grain boundary is connected to phase boundaries at a triple junction.

Previous results do pose an important question, is there any difference in the character of PB1 and PB2? and if so to what extent does it affect the enrichment behavior of C in those phase boundaries? Furthermore, how will this enrichment appear after the C has been extracted by the grain boundary?

To understand the dependence of C enrichment on slight deviations in the boundary character, a cold rolled (50%) medium-Mn alloy of composition Fe-10Mn-3Al-0.2C (wt.%) was subjected to inter-critical annealing at 700°C (30 min-water quenched) followed by tempering at 450°C (2 hours-water quenched). Material characterization revealed a finely distributed equiaxed morphology containing ferrite and austenite phases (figure. 4.5a). With respect to the orientation relationship, the material exhibited boundaries with and without KS OR. Thus, making it a suitable candidate to study the dependence of enrichment on the OR.

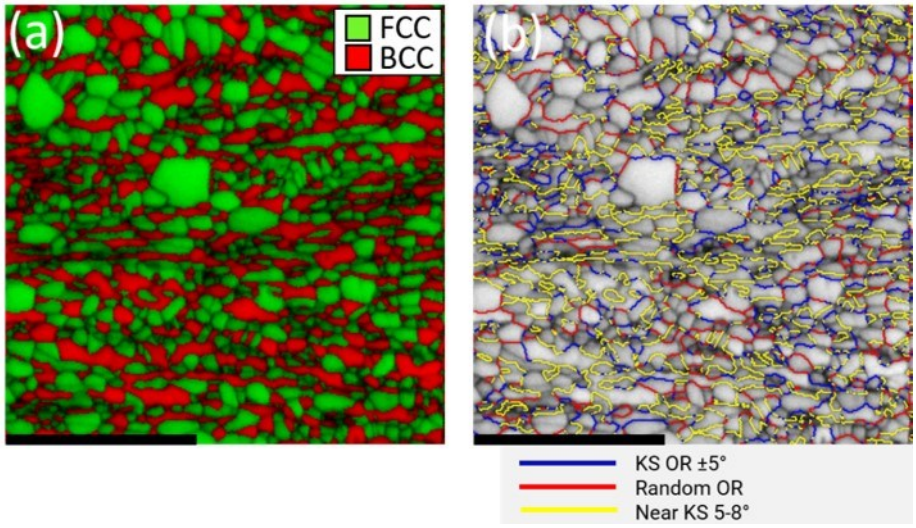

Figure 4.5 (a) Electron backscatter diffraction (EBSD) phase plus image quality map showing the microstructure of the investigated medium Mn steel heat treated at 450°C for 2 hours; (b) OR plus IQ map showing highlighted phase boundaries possessing a Kurdjumov-Sachs (KS) orientation relationship (blue), near Kurdjumov-Sachs (KS) orientation relationship (yellow) and no specific orientation relationships (red). The scale bar is 5µm.

To further enhance our knowledge on the enrichment of C and Mn at the phase boundary, the specimen was studied under APT. Since the sample had submicron sized grains and phase

boundaries with and also without a KS OR, site specific lift out in FIB was not possible. Therefore, a random lift out was practiced and each tip had to be analyzed for crystallographic information of different phases present prior to studying them in APT. Two different techniques were employed crystallographic analysis; TKD and STEM.

4.3.3 Near K-S orientation relationship

Figure. 4.6(a) depicts the IPF and phase map of the APT-tip. Presence of both ferrite (BCC) and austenite (FCC) is evident from the phase map. Elemental map further helps us identify the phases, as can be seen from figure. 4.6(b); A Mn and C lean region corresponds to ferrite (α) while the Mn and C rich region is austenite (γ). The misorientation calculated was ~37°, thus deviating from perfect KS OR by ~6°. Based on the peripheral overlap of poles in the pole figure in figure. 4.6(d) and deviation from perfect KS OR this PB is classified as a Near KS PB and the two phases depicted in figure. 4.6(a) have a Near KS OR between them. To study the

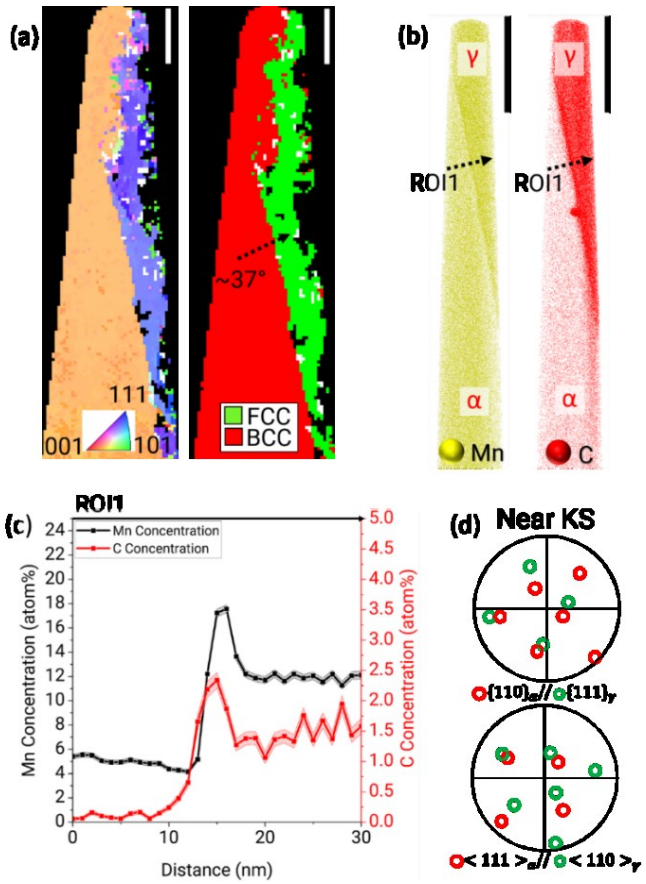

Figure 4.6 (a) IPF and Phase map obtained from Transmission Kikuchi Diffraction (TKD) analysis; (b) Elemental (C and Mn) distribution map in different phases (α and γ) achieved through APT analysis; (c) 1-d Composition profile of C and Mn along the ROI1 (ø15nm) depicted through arrows in (b); (d) Pole figure analysis showing near KS orientation relationship existing between the two phases. The scale is 100nm.

enrichment at the interface, an ROI was drawn through the position denoted as ROI1 in figure. 4.6(b). The obtained composition profile can be seen in figure. 4.6(c). Apart from clear gradient of Mn and C between two phases (α-Mn~5 at.% C~0.1 at.% and γ-Mn~12 at.% C~1.5 at.%), a clear spike in the concentration of both the elements can be seen from the plot. Maximum enrichment of Mn and C at the interfaces is 17.57 at.% and 2.3 at.% respectively.

4.3.4 K-S orientation relationship

Moving on with subsequent APT studies, figure. 4.7(a) shows IPF and phase map of the analyzed tip depicting austenite and ferrite phases. As mentioned earlier and in this case as well, Mn and C, lean and rich regions correspond to ferrite and austenite respectively. Interestingly, the misorientation between two phases is found to be ~43° which is equal to the misorientation of a perfect KS OR. Furthermore, the pole figure analysis shown in figure. 4.7(d) shows substantial overlap of poles thereby confirming the argument on OR based on misorientation angle. The ROI drawn to study the composition variation across the interface in either phase is shown in figure. 4.7(b). The resultant composition profile obtained shows composition gradient between

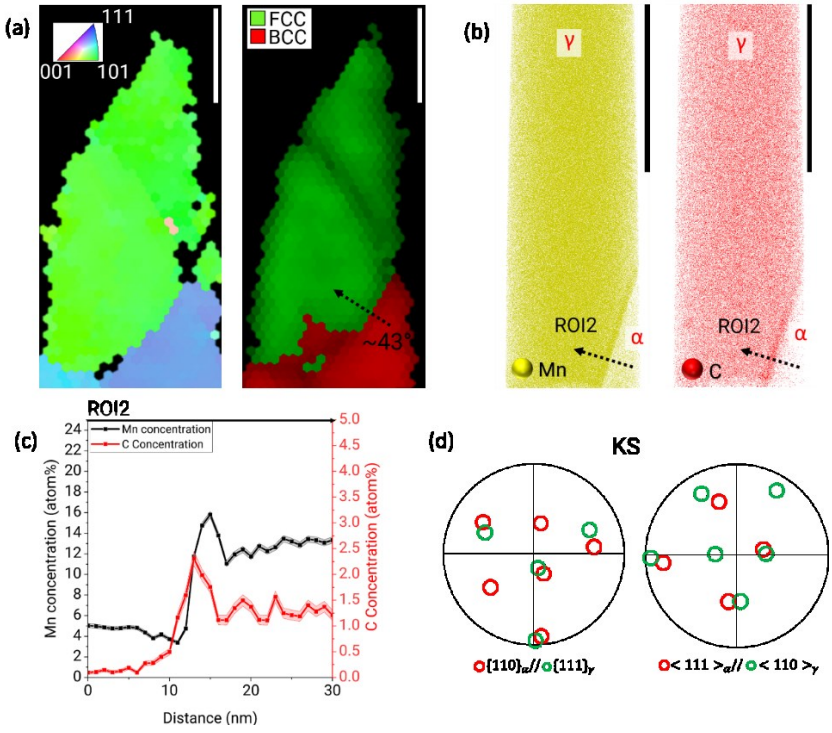

Figure 4.7 (a) IPF and Phase map obtained from TKD analysis; (b) Elemental (C and Mn) distribution map in different phases (α and γ) achieved through APT analysis; (c) 1-d Composition profile of C and Mn along the ROI2 (ø15nm) depicted through arrows in (b); (d) Pole figure analysis showing KS orientation relationship existing between the two phases. The scale is 100nm

two phases and an enrichment of both Mn and C at the interphase boundary. The Mn concentration measured is ~5 at.% and ~12 at.% in ferrite and austenite respectively. C concentration is ~0.1 at.% and ~1.5 at.% in ferrite and austenite respectively. A clear spike in the composition of Mn and C was observed at the phase interface depicting enrichment of elements at the phase boundary. Mn enriched to about 15.28 at.% and C peaked at 2.3 at.% .

One important thing to note is that despite significantly deviating from KS orientation relationship, there was no significant difference in the observed C enrichment behavior. This was not the case for Mn, where enrichment went up from 15.28 at.% at KS OR to 17.57 at.% at Near KS OR.

The energy, structure, and kinetics of α/γ phase boundaries are crucial in phase transformations and microstructure development in most steels. These factors are significant for understanding the mechanical behavior of specific steel classes, such as duplex and transformation-induced plasticity (TRIP) steels [158]. Thus, in this section, an attempt is made to understand the character of the boundaries mentioned in previous section and its influence on enrichment behavior of C and Mn.

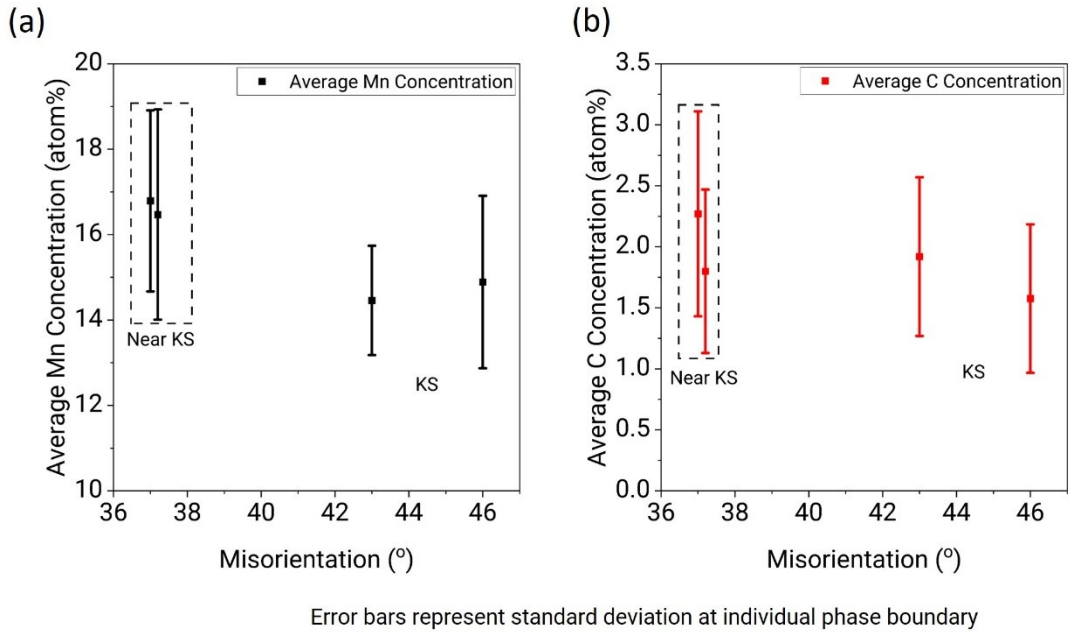

Figure 4.8 Variation in enrichment of (a) Mn and (b) C at the phase boundary based on the misorientation angle between ferrite and austenite phase. (The standard deviation is for individual phase boundary)

Figure. 4.8 shows the variation of Mn and C enrichment at boundaries with varying orientation relationships viz. KS and near KS OR. For the case of Near-KS oriented boundaries, Mn

showed significant difference in enrichment as compared to its KS counterparts. It is a well-established that the enrichment at grain and phase boundaries is dependent upon the boundary structure, and is severely impacted as the coherency at the interface increases [133, 156, 157, 161]. It is thus expected for K-S and N-W interfaces to present lower Mn enrichment as compared to a Near K-S interface. This further suggests that the site density or binding energy at the K-S or N-W interfaces is lower as compared to the Near K-S or non-KS interface [103]. Mn is not the only substitutional element to show such a behavior, molybdenum and vanadium have also been reported to show varying enrichment tendency with a change in OR (between non-KS and near-KS) [103, 162].

Although Mn showed difference in enrichment on moving from KS to near KS, C had comparatively similar range of enrichment across all the misorientation angles and orientation relationships. This observation may appear to contradict the abovementioned theory for Mn but it is consistent with reported enrichment behavior of C [103]. The reason for C not showing any variation in enrichment behavior with change in orientation relationship stems in the observation by Hillert [163] where they observed carbon diffused in the α phase from non-KS to near-KS oriented boundaries, thus feeding and enriching the near-KS boundaries with carbon as well. The observation was consistent over large diffusion distances as well. The difference in enrichment behavior of Mn and other substitution elements helps in understanding the influence of orientation relationship on the suppression of carbide formation. It was reported that with change in OR from non-KS to near-KS, vanadium carbide precipitates were almost absent from the PB after isothermal annealing [164].

From above observation it is clear that even if the two-phase boundaries at the triple junction have a slight or significant difference in their character, it does not necessarily manifest itself in the difference in C enrichment.

4.3.5 DFT calculations (Performed by Dr. Ujjal Saikia)

To achieve a deeper insight of the C segregation competition between austenite GB and PB, DFT calculations [165] were performed to determine the segregation energy of C for the two segregating sites. Σ11[110] 50.48° (figure. 4a) were used as the representative austenite GB for the DFT calculation. The PB was constructed by joining a γ (111) slab with a α (110) slab according to the K-S interface orientation relationship, namely, (111) γ || (110) α and <110> γ || <111> α (figure. 4.9b). With DFT optimized lattice parameters for bulk phases of Fe (2.83 ˚A for α and 3.50 ˚A for γ), ~3% and ~1% strains were used to mitigate the lattice parameter

difference along the interface between the α and γ slabs. For adequate representation of atomic relaxation of the paramagnetic (PM) state of the austenite phase of Fe, spin space averaging (SSA) relaxation method was adopted as described in Refs. [166, 167]. Within this method, instead of an instantaneous force resulting from a static magnetic configuration, the atoms are displaced according to the averaged force over several (here 15) different magnetic configurations. An electronic structure code SPHInX [168] is used for all DFT calculations. To identify the potential segregation sites, we consider three different geometric indicators, Voronoi volume, Fe-C bond length and coordination number. Initially, C atom is placed at the interstitial sites of the GB and PB planes having the maximum Voronoi volume or Fe-C distance or minimum coordination number. Thereon atomic relaxation is performed to achieve optimized configuration. Following this strategy, a C atom is placed at different sites of the GB and PB plane and calculated the segregation tendency of C to these sites from bulk fcc and bcc octahedral sites. The most favorable segregation energy for each scenario is shown as a bar plot in figure. 4.9c. The segregation energy of C from bulk γ to γ/γ GB is -0.91eV, lower than the segregation energy to the phase boundary (-0.74 eV). Thus, it is evident from the plot that segregation of C to γ GB is more energetically favorable as to compared to KS oriented phase boundary.

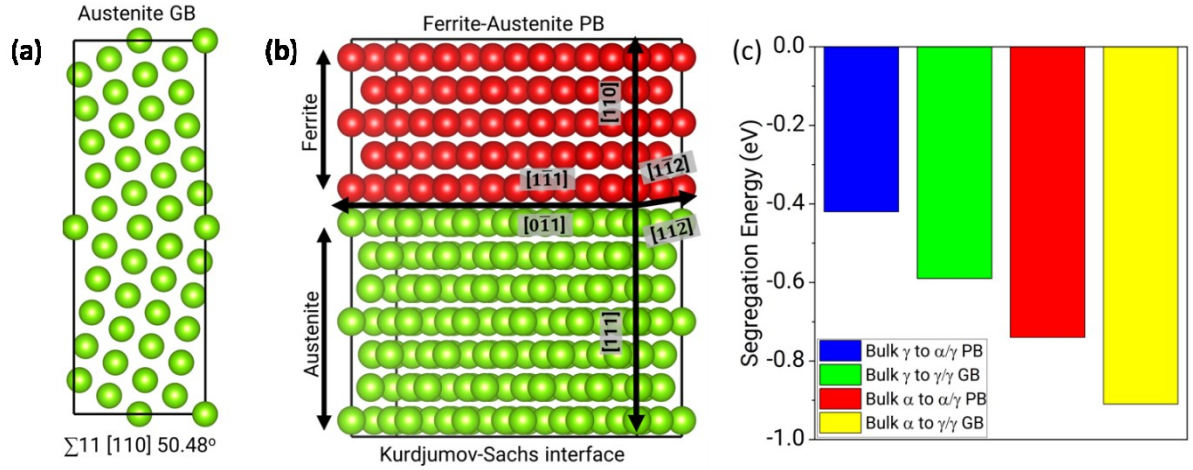

Figure 4.9 Schematic view of (a) Σ11 grain boundary, and (b) fcc-bcc KS interface supercell used for DFT calculations, (c) The segregation energy of C from bulk bcc and fcc octahedral sites to the most favorable sites at the austenite grain boundary and KS oriented phase boundary.

The difference in the calculated segregation energy between grain and coherent phase boundaries further helps to understand the heterogeneous C segregation behavior observed in figure. 4.2. Here it is proposed that the solute segregation of one interface has an effect on the segregation behavior of the same solute at adjoining interfaces. Since most of the adjacent

phases are KS oriented, resulting in much lower segregation energy compared to high-angle grain boundaries, it is expected that the grain boundary will be the preferred region for C enrichment, as shown in figure. 4.2. These grain boundaries thus serve as a sink for C, which reduces its segregating amount at adjoining phase boundaries. This can be visualized from figure 4.3, where PB1 shows a decreasing gradient of C concentration towards the triple junction and the austenite grain boundary. This effect is more intensive for the case of PB2 where it was devoid of any C enrichment. In previous studies about solute segregation and it's engineering methods [169, 170], the interdependency of grain and phase boundaries in trapping solute elements is often overlooked.

4.3.6. Phase interface with small misorientations

Figure. 4.10(a) shows a phase map depicting ferrite (α) and austenite (γ) phase present in the APT tip. There appears to be no concentration gradient in Mn content on moving from α_2 to γ_2 (figure. 4.10b and e). When compared to previous results where there was clear phase separation visible based on composition difference this seems like an anomaly. The hypothesis to understand this observation lies in the fact that the region highlighted as α_2 would have been γ (fcc, austenite, parent phase) during tempering and transformed to α (bcc, ferrite, product phase) structure during quenching. The foundation of this hypothesis lies in the C atomic distribution, concentration profile and density map (figure. 4.10b and e). The density map shows the region denoted as α_2 depleted of C. This depletion of C can very well be attributed to carbide precipitation in the vicinity, which could have acted as a sink for C from the highlighted region of α_2. One such carbide particle is shown in figure. 4.10(c). From composition analysis of the carbide shows it to be Fe_xC_y type of carbide (figure. 4.10e). Detrimental effect of C depletion on the austenite thermal stability is well known [41, 171, 172]. This depletion of C can locally destabilize austenite and thereby increase the probability of its transformation during quenching. There are two possible product phases that could have formed from austenite: bainite or massive ferrite. The possibilities of each product will be investigated based on crystallographic information available from the STEM and APT analysis.

For α_2 to be a bainite phase, it has to satisfy the orientation relationship criteria i.e. NW OR with the austenite phase into which it is growing [173-176]. As can be seen from figure. 4.10(d) there is no overlap of poles, also the misorientation between α_2 and γ_2 is also found to be ~10°; which is far away from the ideal NW OR (47°) or KS OR (43°). Therefore, despite having same Mn composition as the parent austenite, the α_2 cannot correspond to bainite due to OR limitation. Coming to massive ferrite, since there is no specific OR requirement for its

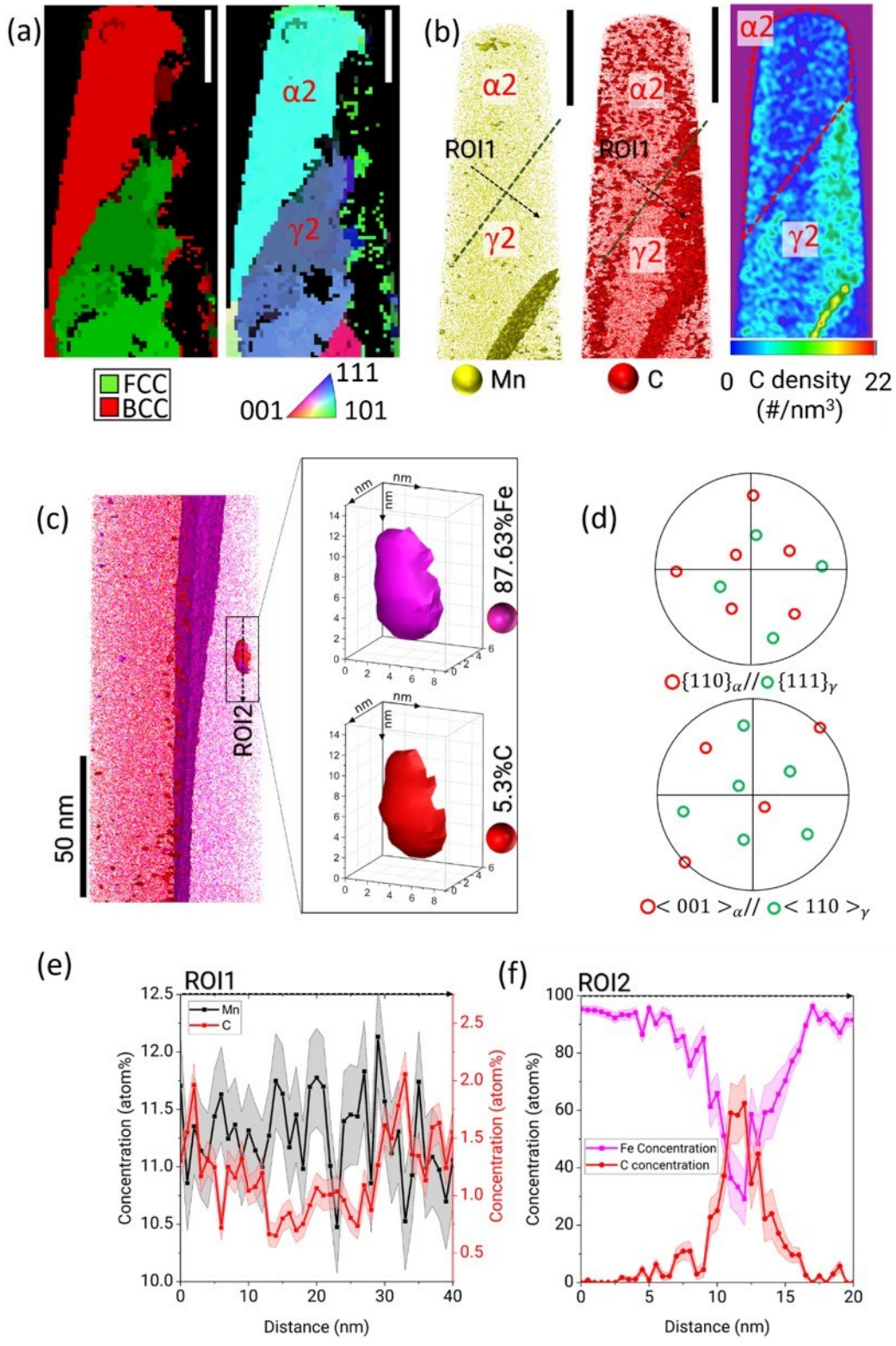

Figure 4.10 (a) IPF Map obtained after STEM analysis; (b) Mn and C atomic map and C density distribution map in different phases (α and γ) achieved through APT analysis; (c) elemental map depicting carbide particle; (d) Pole figure analysis showing non-NW orientation relationship existing between the α_2 and γ_2 phases; Composition profile along the (e) ROI1(ϕ=10nm) and (f) ROI2 (ϕ=3nm), The scale in (a) and (b) is 100 nm.

formation, its nucleation mechanism needs to be discussed [177, 178]. Massive ferrite preferentially nucleates with a hemispherical cap shape at the coherent surface of the boundary [179] and grows with an incoherent boundary. The misorientation between α_2 and γ_2 is 10°, thus very well lying the domain of a low angle grain boundary and is expected to exhibit small patches of coherent atomic matching between misfit dislocations. These coherent parts can very well act as a potential nucleating sites for massive ferrite and resulting in a ferrite with Mn composition same as the parent austenite grain. The low misorientation also explains why there was no pre-transformation enrichment visible.

4.4 Conclusion

The study expands the understanding of interfacial solute segregation in multiphase steels by revealing the thermodynamic competition among different interfaces and its impact on C segregation behavior. Both APT results and DFT calculation showed that high-angle austenite grain boundaries tended to trap a higher amount of C compared with coherent α/γ phase boundaries upon low-temperature heat treatment of a medium Mn steel. Such discrepancy in segregation capacity resulted in a rather heterogenous C segregation behavior within the interface plane when two types of interfaces joined together.

5. Solute decoration states at α/γ phase boundary

5.1. Introduction

Interfaces that embellish the multi-phase microstructure, separating two crystals differing in Bravais lattice, composition, or both lattice and composition, are classified as phase boundaries. Based on atomic matching, these phase boundaries are further categorized as coherent (with a continuous boundary plane and lattice), semi-coherent (featuring periodic regions of coherency and dis-registry), or incoherent (exhibiting a disordered atomic arrangement with a liquid-like atomic coordination) [142, 146]. The fact that phase boundaries have a distinct interface structure and chemistry differentiates them from random high-angle grain boundaries [180-182]. Additionally, the existing mechanical contrast between abutting phases results in high stress/strain concentration at phase boundaries [143-145]. The compound effect of these characteristics of phase boundaries affects the yielding behavior [9, 183], damage tolerance [107], and hydrogen susceptibility [184] of AHSSs. These interfaces are often considered weak links causing material failure; however, they can be modified with respect to *fraction*, *chemistry*, and *structure* to enhance the strength and toughness of the material [185, 186].

In the same modification scheme, medium Mn steels are often subjected to inter-critical annealing to create a two-phase microstructure of ferrite and austenite [41, 187]. This microstructure typically possesses an ultra-fine grain size with a high area fraction of ferrite-austenite phase boundaries, which can become the dominant planar defects affecting the mechanical behavior of medium Mn steels [188]. Dislocation emission from these phase boundaries in the early yielding stage has been observed, suggesting that the large phase boundary area can provide a high density of dislocation sources, leading to the rapid multiplication of mobile dislocations and influencing the yielding behavior [9].

Inter-critical annealing followed by tempering further modifies the chemistry of phase boundaries, often expressed through solute segregation [117], depletion [124], or the precipitation of second phases [170]. When considering high-Mn steels, C segregation is conducive to Mn-C short-range ordering subsequently increasing the stress for interface

dislocation nucleation. Short-range ordering has also been observed to enhance radiation damage resistance, although specifically for MPEAs [125, 189]. Apart from segregation at the phase boundaries, segregation of interstitial atoms at the dislocation has also been reported to increase the yield strength by Cottrell-Bilby interaction, albeit in single-phase ferrite microstructure [190, 191]. Segregation of C at the α/γ phase boundaries increases the yield strength for micro-yielding by around 100 MPa [9]. It was hypothesized that the strong interaction of C with dislocations and ledges present at the phase boundaries increases the energy barrier for dislocation nucleation. As in the case of grain boundaries, where solute segregation stabilizes the dislocation and ledges [137, 192, 193], and the Hall-Petch coefficient K_y increases [140], subsequently increasing the barrier for dislocation emission, the same understanding can be extended to phase boundaries as well [194] [195]. Furthermore, as suggested by molecular dynamics simulations, atomic reshuffling takes place at the interface to support dislocation emission, which could be obstructed by carbon segregation owing to the strong localization of electrons at the iron atoms, resulting in the covalent nature of the bond between carbon and iron, thereby increasing the energy barrier for atomic rearrangement [196, 197].

Having maintained the role of inter-facial ledges and dislocations earlier, there is no exaggeration in saying that the interface structure is one of the most critical factors influencing boundary energy and elemental decoration. Generally, as disorder and compositional differences increase, boundary energy tends to rise, while boundary friction, inversely related to mobility, decreases with greater in-coherency. The energy of coherent phase boundaries typically ranges from 2 to 100 mJ/m^2, whereas incoherent boundaries are believed to exceed several hundred mJ/m^2, with semi-coherent boundaries falling in between. There is a significant correlation between the heat of sublimation and surface energies, as well as grain boundary energy, which is dependent on the adsorption of solute atoms. Consequently, phase boundary energies are also expected to be influenced by solute decorations, especially in semi-coherent and incoherent boundaries [142, 146].

While ample data on solute segregation at grain boundaries exists [117, 129, 133, 139], research on the structure of inter-phase boundaries and the solute segregation associated with them is scarce and needs a thorough investigation. In this work, the aim is to bridge the gap between the observed segregation at the phase boundary and the segregation state of elements at the phase boundary.

5.2 Methods

A medium Mn steel with a chemical composition of Fe-10Mn-3Al-0.2C (wt.%) was selected for this investigation. After austenitization (1000°C-30min) followed by intercritical annealing (700°C-30min) and tempering (450°C-50h) treatments, an ultrafine ferrite-austenite laminated microstructure is obtained (as shown in figure. 5.1a) in which almost all, if not every phase boundary, possess a Kurdjumov-Sachs (KS) orientation relationship (OR), as depicted in figure. 5.1(b). Atom probe tomography (APT) is used to study the Manganese (Mn) segregation behaviour at different types of interfaces which primarily occurs during the tempering treatment.

5.3 Results and discussion

5.3.1 Phase evolution and composition

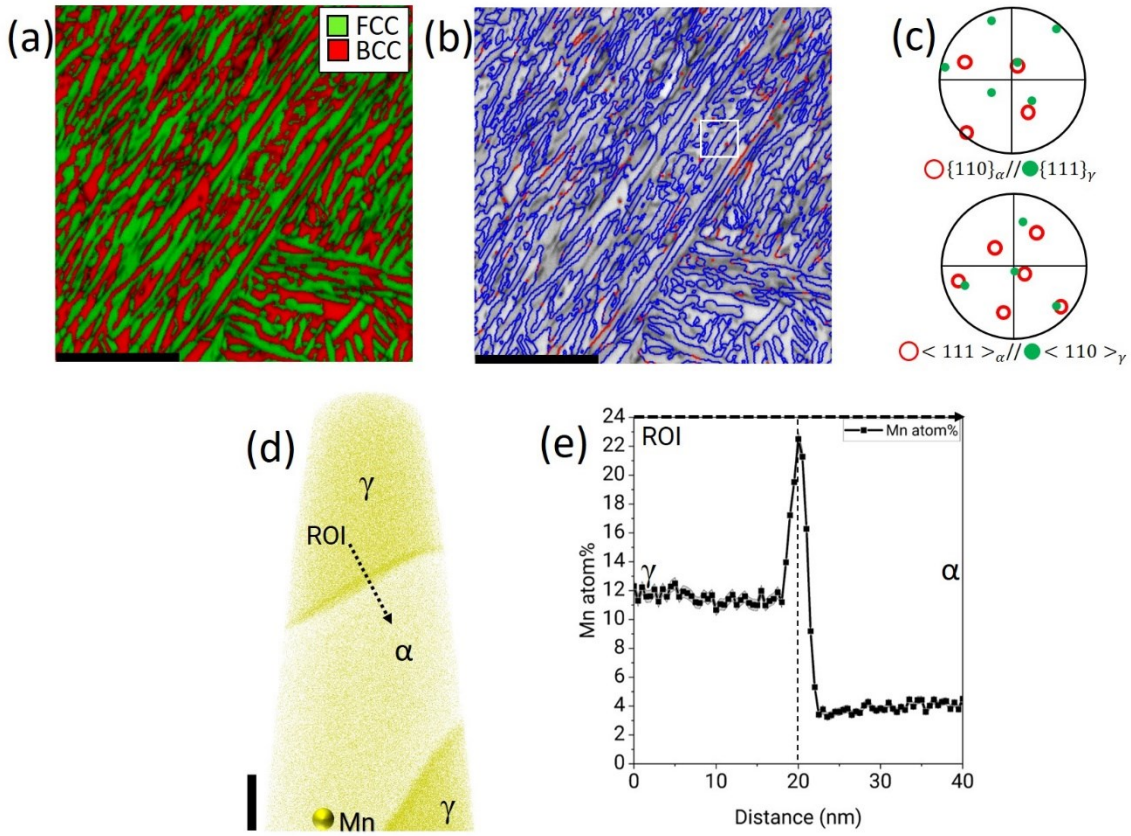

Figure 5.1 (a) IQ+Phase map showing microstructure obtained after annealing for 50 hours at 450°C, (b) IQ map showing highlighted boundaries depicting Kurdjumov-Sachs (KS) interfaces (blue) and interfaces with random orientation relationship (red), (c) Pole figure showing overlapping closed packed planes and direction for the region marked by square in (b), (d) Mn distribution map obtained from APT analysis, (e) 1-Dimensional composition profile across α/γ phase boundary; ROI: φ: 15nm, l=40nm, scale bar in (a) and (b) is 5 µm and in (d) is 25 nm

The microstructure obtained after the heat treatment routine is shown in figure. 5.1(a), characterized by an alternating ferrite and austenite laminated microstructure. The orientation relationship between the two phases is predominantly K-S, as highlighted by the blue color in figure. 5.1(b). The Mn distribution map obtained from APT analysis is shown in figure 5.1(d). The Mn-lean region in the reconstructed tip (AP Suite 6.3.1) is the α iron (BCC) phase, while the Mn-rich region is the γ iron (FCC) phase.

To study the Mn distribution across the α/γ phase boundary, a 1-D composition profile is drawn and shown in figure. 5.1(e). There is a clear concentration difference between the two adjoining phases, with approximately 12 at.% Mn in the austenite (FCC, γ) phase and about 4.5 at.% in the ferrite (BCC, α) phase. A clear spike of ~18 at.% Mn concentration at the phase boundary is also visible..

In the subsequent section, the in-plane distribution of Mn and the associated crystallographic features leading to this distribution are correlated.

5.3.2. Features in straight phase boundary

Reconstructing one of the APT datasets revealed a straight phase boundary separating two chemically distinct phases: ferrite (Mn lean) and austenite (Mn rich) (figure. 5.2a). Furthermore, equidistant Mn-enriched tubular and linear features, spaced about ~17 nm apart, were observed decorating the plane of the straight phase boundary (figure. 5.2b). As known from the EBSD analysis, almost all the boundaries have a K-S orientation relationship (KS OR) between adjacent phases (figure. 5.1b). The most probable explanation for such atomic-scale segregation is that these tubular and linear features likely correspond to steps or interface dislocations.

A density plot of these proposed dislocations is shown in figure. 5.2(b). Here, a pronounced presence of Mn (~55 atoms/nm^3) can be seen along the highlighted Mn iso-surface in figure. 5.2(b). The compositional distribution across the parallelly spaced steps yielded the profile depicted in figure. 5.2(d). High enrichment of Mn, approximately 19-20 at.%, is evident exactly at the proposed interfacial dislocations.

Previous reports on Mn segregation to dislocations are limited to either matrix dislocations or to dislocations present at low-angle grain boundaries [118, 198-200]. Segregation to interface dislocation at the coherent/semi-coherent phase boundary is not a thoroughly researched topic. So far there has been only one report (Tungsten and Cobalt) on segregation at phase boundary

defects has been reported. However, in that case, the regions of interest were multiple atomic layers, as the defect plane corresponded to a stacking fault between the fcc and γL12 phases [201].

The ion map extracted from the α phase of the apt tip reveals poles of (110) family (figure. 5.2e). The plane spacing was adjusted by changing the initial tip radius and the final distance between each peak of count vs z plot was exactly 0.203 nm between atomic planes (figure. 5.2f). This initial tip radius was then used for calibrating the APT tip. The red vector denoted in figure. 5.2(g) is parallel to one of the proposed dislocations lines and is found to have ~93°, 51° and 115° with each (110) poles (figure. 5.2h). By employing pole figure analysis, it is clear that the dislocation vector has a line direction of <4-41> on (110) boundary plane. Since (110) is a primary slip plane for BCC, this linear feature very well satisfies the criteria to considered a lattice dislocation and henceforth termed as misfit dislocation [202]. Considering a/2[111] as the dislocation burgers vector for K-S OR [151, 180, 203-205], the dislocation line is identified to have a mixed character as it makes ~84.2° angle with the Burgers vector. The observation is consistent with the reported results for misfit dislocations at the interface with K-S OR [151, 180].

In order to further understand the spacing between misfit dislocations, similar boundaries that exhibited a KS OR were studied under transmission electron microscope (TEM measurement were performed by Dr. Vivek Devulapalli). Figure. 5.3(a) shows the corresponding bright field TEM image depicting an α/γ phase boundary decorated with periodic strain marks with a ~18 nm spacing. Energy dispersive spectroscopy (EDS) analysis shows high concentration of Mn in the γ phase and a depleted α phase (figure. 5.3b). Adding on, a preferential enrichment of Mn is seen in those strain marks (figure. 5.3a). The crystallographic information obtained from the TKD of the lamella helped identify that the boundary has a scatter of +0.2° around perfect KS OR (figure. 5.3d). Comparing the APT reconstruction and TEM micrograph it very well concludes that these features are transformation structures that are reminiscence of austenite reversion during intercritical annealing of martensite [52, 77, 78].

Commenting on the misfit spacing and deviation from exact KS OR is beyond the scope of this work, but a qualitative comparison can be made. Traditionally, the spacing between misfit dislocation increases with decrease in deviation from coherent orientation relationship, with perfect KS OR having no misfit defects. For a 1° and 3.7° angle between closed pack planes and direction respectively, misfit dislocations for every third layer of closed packed planes

were reported [180]. Atomistic simulation for 3.11° and 4.75° angle between closed pack planes revealed a misfit spacing of ~4 nm and ~2.55 nm [181]. Following the same analogy, the deviation for the observed interface in figure. 5.3(a) is only ~0.28° and ~0.27° between the close-packed planes and direction. Therefore, it is logical to expect that the misfit dislocations will have a larger spacing between them. The observed distance between strain marks is approximately 20 nm. If the traditional formula for misfit dislocation spacing, considering deviation from perfect coherency orientation, is used, it overestimates the spacing by a factor of two (47 nm). This discrepancy is well within the acceptable limit, as the true nature of the boundary is not known. It is unclear whether it is a tilt or twist boundary, or if the dislocation is full or partial.

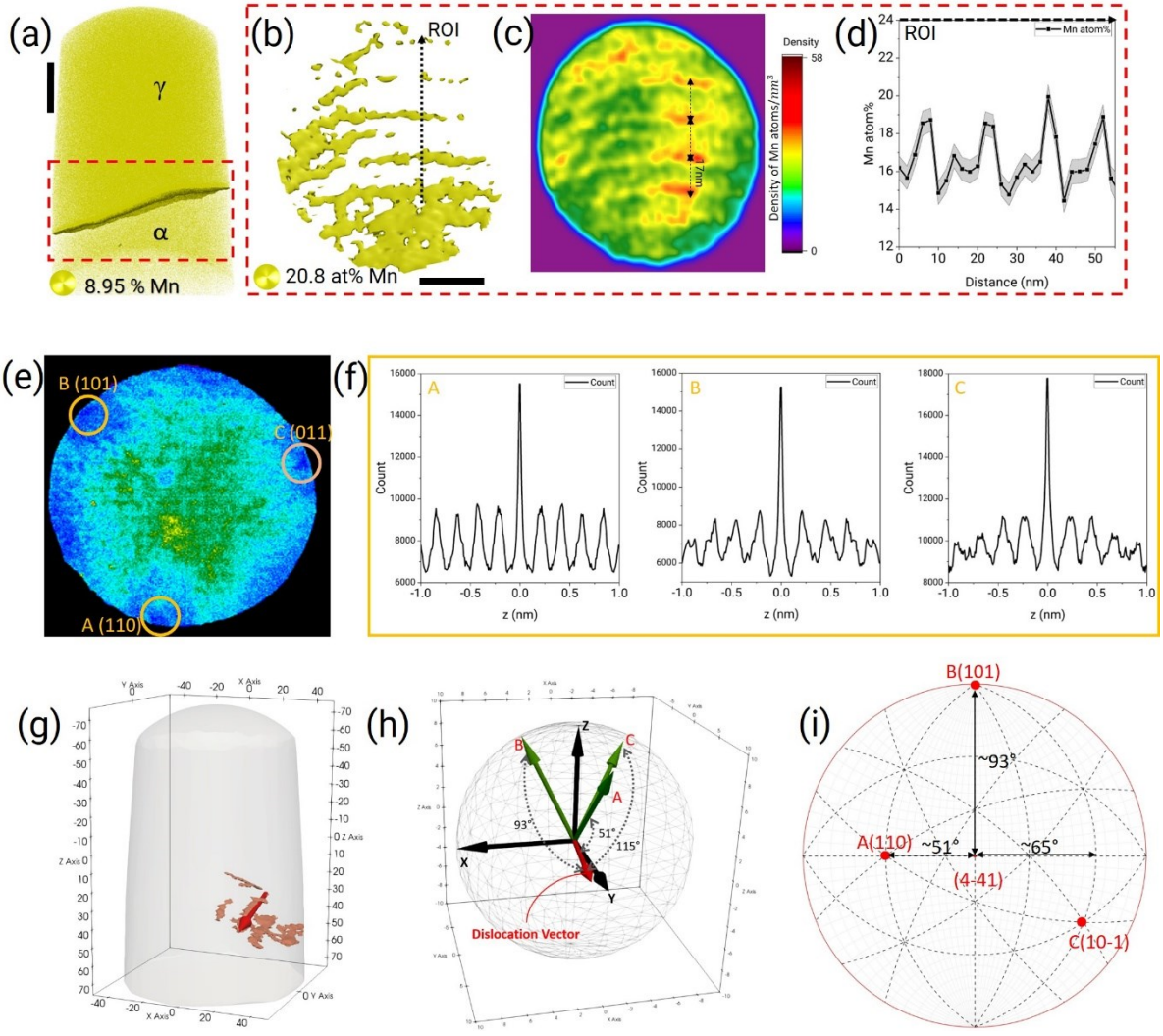

Figure 5.2 (a) Mn distribution map obtained from APT analysis showing α and γ phases with highlighted phase boundary, (b) Enrichment of Mn along the linear features, (c) Mn density map, (d) 1-Dimensional composition profile across linear features shown in (b) (ROI ϕ=5nm), (e) Ion hit map obtained from α phase in the apt tip showing (110) family poles, (f) Atomic planes obtained from each

of the poles,(g) Extracted dislocations from the APT data with dislocation direction, (h) Angle between dislocation vector and three poles, (i) Pole figure with three poles and the correspond dislocation vector, Scale in (a) and (b) is 25 nm.

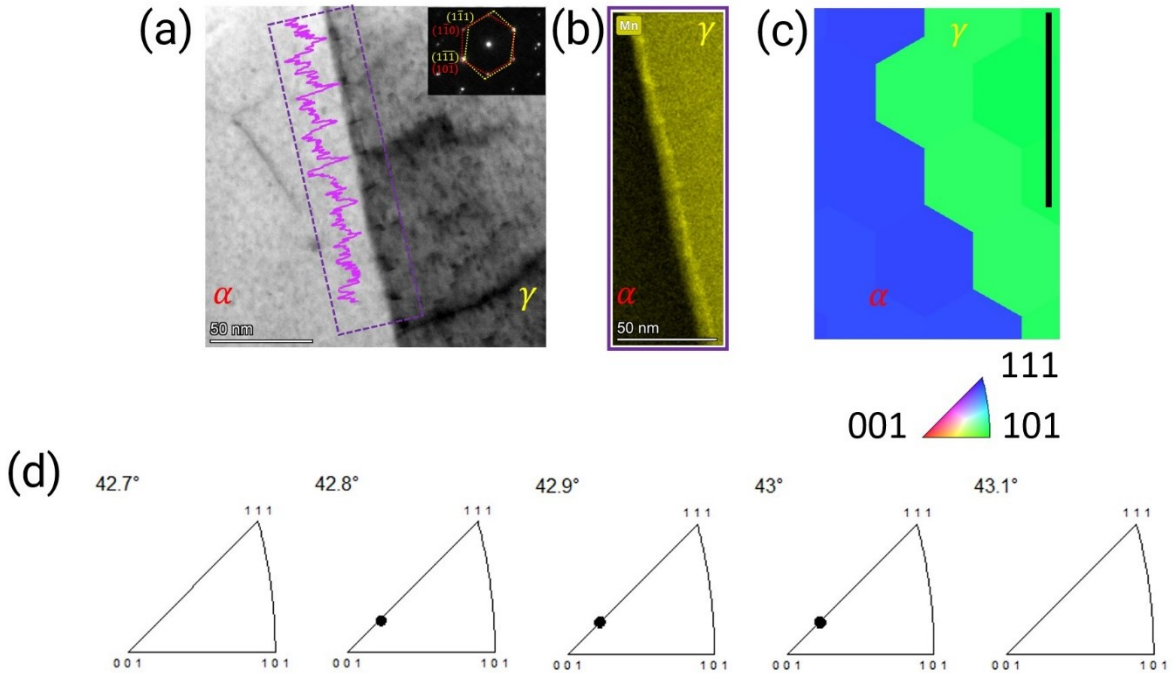

Figure 5.3 (a) Bright field TEM image of α/γ phase boundary, (b) EDS phase map of the region enclosed in (a), (c) Inverse pole figure of the enclosed region in (a); scale bar is 50nm, (d) Angle-axis misorientation. Scale in (c) is 50nm (Measurements performed by Dr. Vivek Devulapalli)

5.3.3. Features in curved phase boundary

On analyzing one of the curved phase boundaries, it was observed that the entire phase boundary surface had a serrated or stepped appearance (figure 5.4b), unlike straight boundaries. These features appear to be interface ledges or facets. Furthermore, apart from an overall enrichment of manganese at the phase boundary, a preferential presence of Mn was recorded in the density plot exactly at the facet junctions (figure. 5.4c).

To get a glimpse of the concentration of Mn enrichment in these proposed features, 22 at.% concentration surface was observed, which revealed Mn atoms preferentially segregating along these junctions (figure. 5.4d). Performing a 1-D concentration analysis along the ROI to get concentration variation across the proposed ledges, we found the variation of Mn enrichment to range between ~21 and 23 at.%, which is about 3 at.% higher than what is observed for the case of dislocations (figure. 5.4e). Unlike grain boundaries, where observing segregation at the

interface facets is very common [126, 134, 206-208], the same has not been reported for phase boundaries, especially when a coherent or nearly coherent interface is involved.

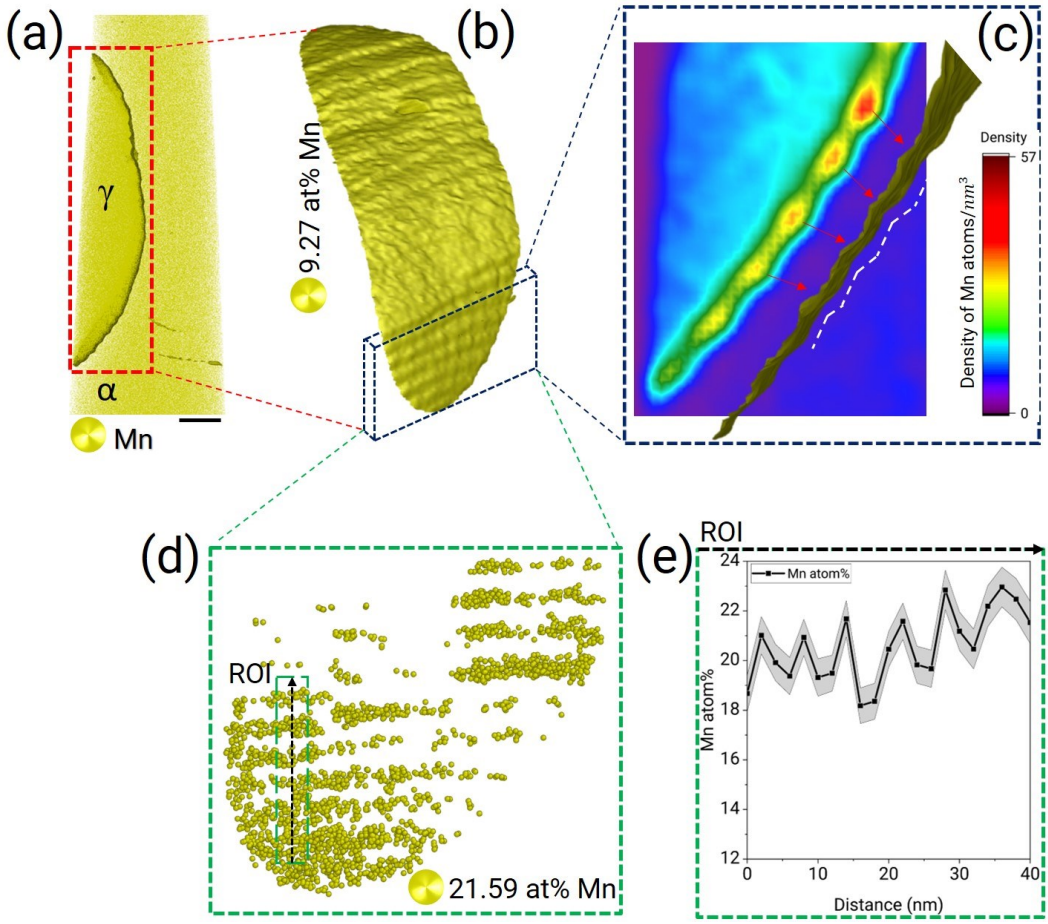

Figure 5.4 (a) Mn distribution map obtained from APT analysis showing α and γ phases with highlighted curved phase boundary, (b) Phase boundary with steps, (c) Mn density map, (d) Significantly high Mn atoms along linear features, (e) 1-D composition profile across the ROI (ϕ=5nm) shown in (d). Scale in (a) is 25 nm.

TEM analysis was further performed on a TEM lamella from the same sample to gain insight into the nature of these ledges/facets, as depicted in figure. 5.5 (Measurement performed by Dr. Vivek Devulapalli). It is evident that as the interphase boundary between the γ and α phases starts to change its curvature, steps begin to appear denoted as $P\alpha_1$, $P\alpha_2$, $P\gamma_1$ and $P\gamma_2$. Since the observed phase boundary does not have an edge on orientation, the identification of boundary plane indices is not straight forward. By employing boundary trace analysis, planes with up to (555) indices were identified and corresponding misorientation tolerance of 2° (M_1) was considered. As mentioned earlier, the boundary has significant inclination, another parameter was considered, angle with vertical axis (V_1). Therefore, indices making 70-90° angle with the vertical axis were discarded. Another important parameter to be considered is distance in

degrees from the trace of the plane in each crystal system (Tα and Tγ). It is evident from the Table. 5.1 that among the set of planes ascribed for $P\alpha_1$ and $P\gamma_1$, there are two combinations; $(435)_\alpha$, $(302)_\gamma$ and $(445)_\alpha$, $(504)_\gamma$ are very close to $(111)_\alpha$ and $(101)_\gamma$. This is in correspondence with Greninger–Troiano (GT') orientation relationship [83, 209], $(111)_\alpha||(110)_\gamma$; an irrational orientation relationship [210]. As for the step denoted by $P\alpha_2$ and $P\gamma_2$, two set of planes were identified and neither of them can be reduced to set of planes known for reported rational or irrational orientation relationships.

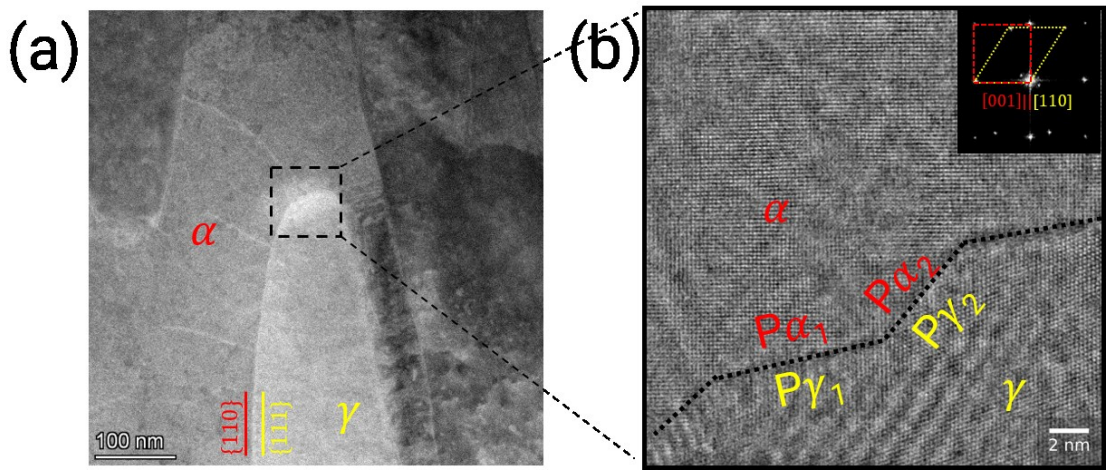

Figure 5.5 (a) Bright field TEM image of α/γ phase boundary, (b) Magnified image of the curved interface with ledges separating the α and γ phases, inset has the diffraction pattern of the interface seen along $<001>_\alpha||<110>_\gamma$ direction (Measurements performed by Dr. Vivek Devulapalli).

$P\alpha_1$	$P\gamma_1$	M_1 (°)	Tα (°)	Tγ (°)	V_1 (°)
(211)	(253)	1.49	9.46	9.06	35
(435)	(302)	1.95	2.06	3.16	55
(534)	(153)	1.13	5.39	5.07	44
(445)	(504)	1.76	8.64	7.6	58

$P\alpha_2$	$P\gamma_2$	M_1 (°)	Tα (°)	Tγ (°)	V_1 (°)
(315)	(140)	0.58	3.9	3.5	60
(515)	(100)	0.61	3.23	2.94	45

Table 5.1: Probable indices of the boundary plane and associated misorientation between them, distance in degrees from the trace and angle from the vertical axis.

This is consistent with the requirement for multiple height facets to exist; multiple height facets can only exist if the facets have irrational or high-index planes [202]. In conventional literature, such crystallographic features are termed superledges. These should not be mistaken for transformation ledges, which are primarily formed during phase transformations to accommodate transformation strain due to phase changes. One such ledge is shown in figure. 5.6. Transformation ledges tend to form in straight phase boundaries where it is easier to accommodate shear [211, 212]. Most common example of transformation ledges is seen in nucleation and growth of proeutectoid ferrite in steels [213]. Multiple height ledges observed on a curved boundary indicate complex interactions between growth processes, impurity effects, and strain minimization mechanisms. When a curved boundary exists, the curvature leads to variations in local strain, making it energetically favorable for unit steps to bunch together, forming superledges to reduce the overall strain energy [202, 214].

In crystal growth, superledges provide sites for the incorporation of atoms, facilitating the advancement of the growth front. They are particularly beneficial in minimizing surface energy during the addition of new atomic layers. These ledges help to reduce the overall energy of the system by accommodating local variations in strain and facilitating the movement of the interface during growth or transformation. Impurities and extrinsic dislocations can pin unit steps, encouraging their aggregation into superledges. These interactions help stabilize the interface by reducing local strain concentrations and facilitating smoother transformation or growth processes [97, 202].

In one reported work [215], curved phase boundary with high index planes are also called as quasi ledges. Quasi-ledges are specialized structural features that form at high-energy, curved, or irregular interphase boundaries in crystalline materials. Unlike regular ledges, which are typically associated with planar and low-energy interfaces, quasi-ledges develop as the boundary navigates around obstacles such as precipitates. These obstacles pin sections of the boundary, causing it to bow and create a series of steps or quasi-ledges. This bowing action and step formation help to accommodate local variations in strain and reduce the overall energy of the system. Quasi-ledges are crucial in managing the complex interactions between the migrating interface and the precipitates, effectively distributing the strain and stabilizing the interface.

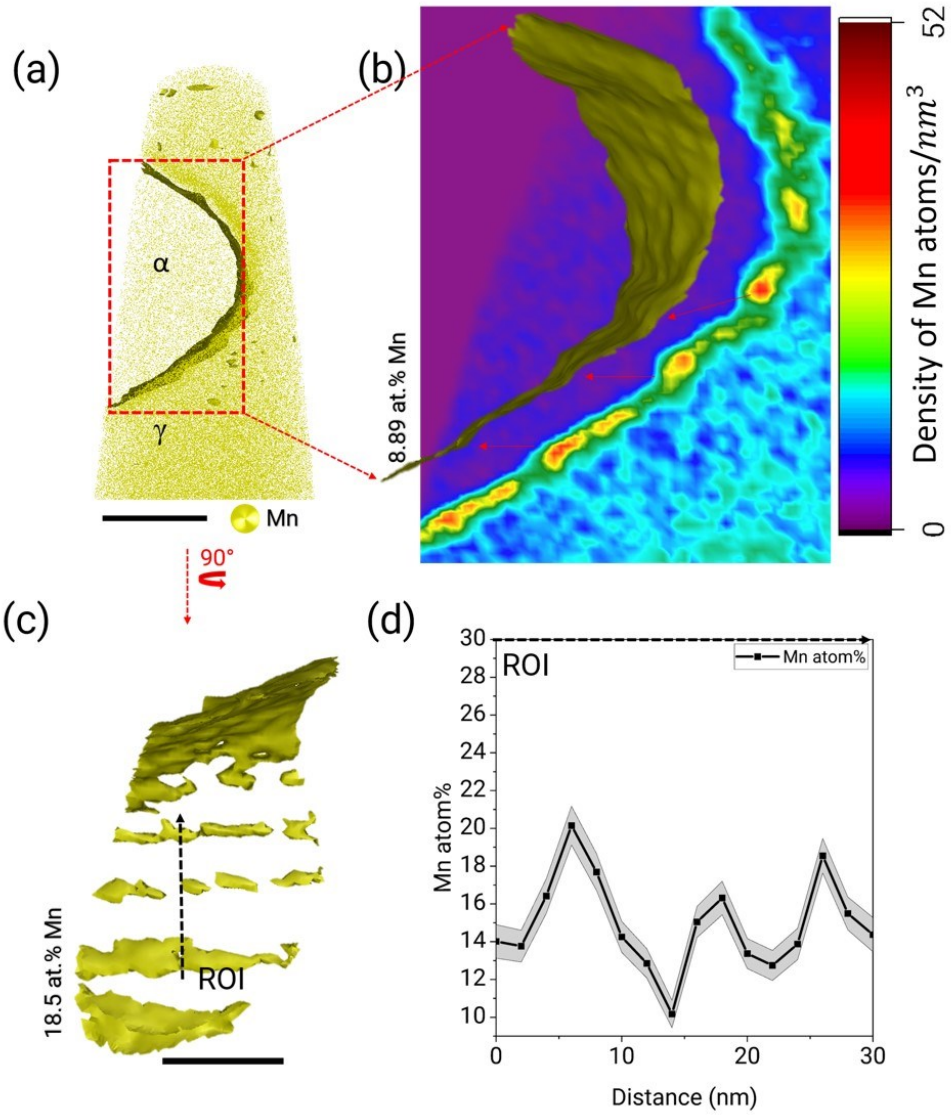

Figure 5.6 (a) Mn distribution map obtained from APT analysis showing α and ϒ phases with highlighted curved phase boundary, (b) Phase boundary with steps with Mn density map showing high intensity of Mn at the steps, (c) Significantly high Mn atoms along linear features, (d) 1-D composition profile across the ROI (ϕ=5nm) shown in (d). Scale in (a) and (c) is 20 nm.

Considering the above-mentioned characteristics of superledges, it is reasonable to conclude that the observed superledges in figure. 5.4 and 5.5 are primarily associated with diffusive transformation [97, 202, 216] rather than a displacive one. Since these ledges were observed in the growth direction of austenite lamella, and the temperature of tempering favors ferrite growth, it is most probable that these features are remanence of the austenite growth structure during intercritical annealing at 700°C.

5.3.4. Time dependent evolution of enrichment

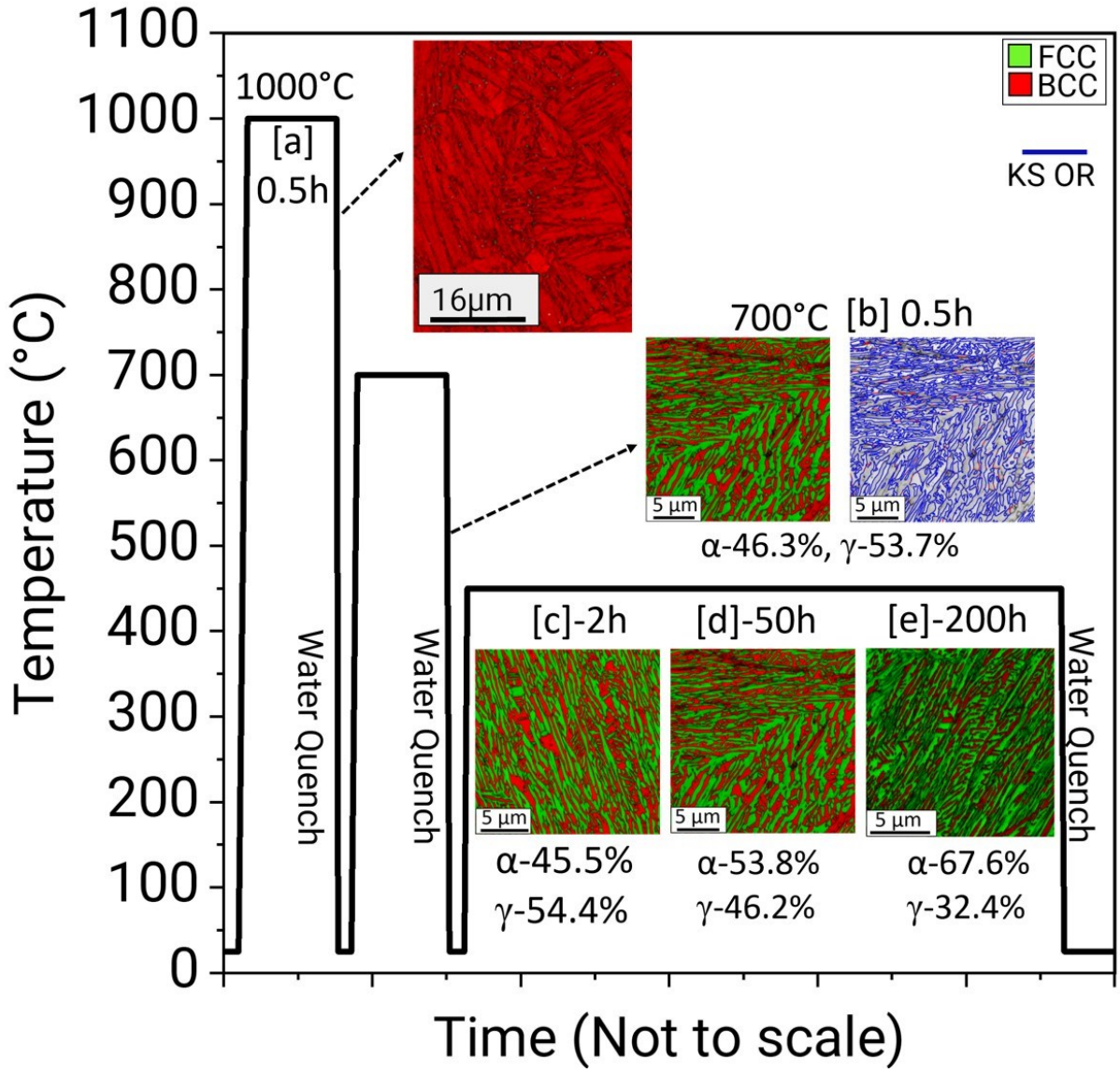

Figure 5.7 Heat treatment schedule with microstructure developed after quenching from (a) 1000°C-30 min, (b) 700°C-30 min (IA), (c) 450°C-2 hours (T2), (d) 450°C-50 hours (T50), (e) 450°C-200 hours (T200)

In order to understand how the enrichment in these features is changing with time and how does this relate to the observed enrichment in APT results, sample achieved after intercritical annealing (700°C-30min WQ) is subjected to varying tempering time, 2, 50, 200 hours. Resulting microstructure is presented in figure. 5.7 (c) through (e). The abbreviations from now will used as such: IA-intercritically annealed sample, T2-tempered for 2 hours, T50-tempered for 50 hours, T200- tempered for 200 hours. It is evident that the phase fraction of ferrite (α) is

increasing with increasing tempering time. This also indicates that partitioning is actively taking place between austenite and ferrite.

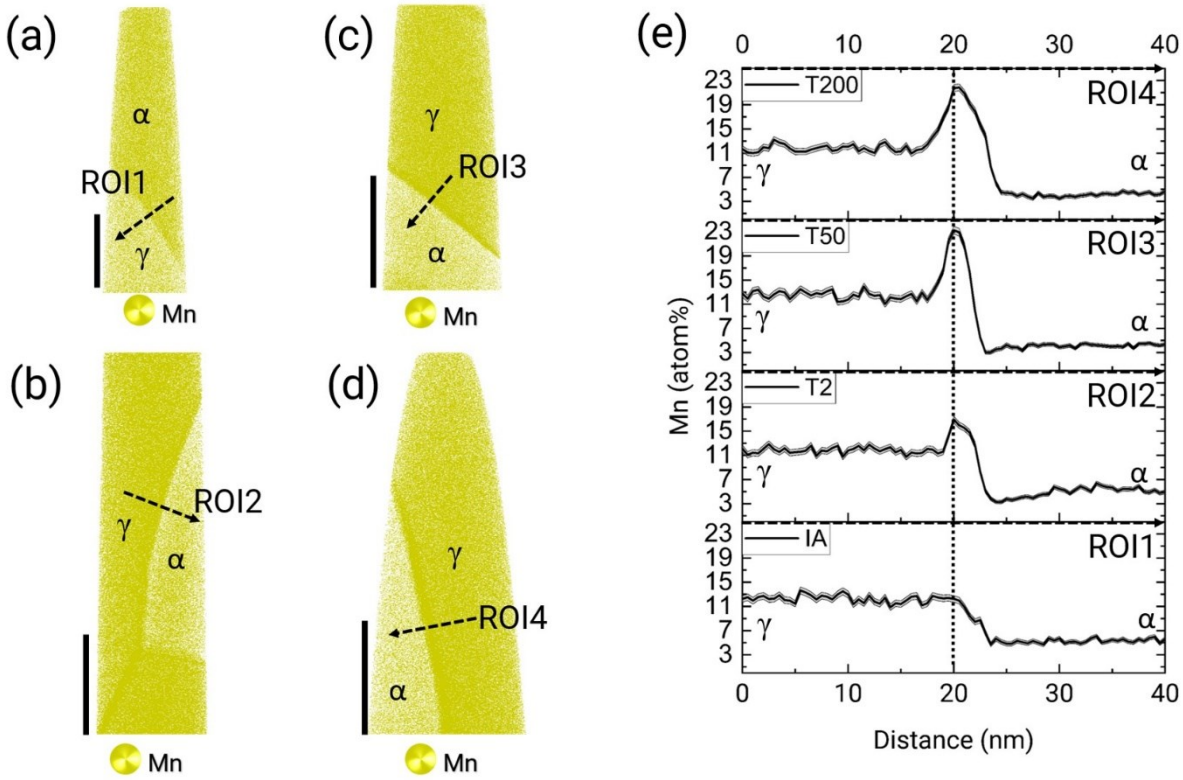

Figure 5.8 Mn distribution map across α/γ phase boundary for samples (a) IA, (b) T2, (c) T50, (d) T200, (e) composition profile across ROIs (ø15nm). Scale is 100nm

To get an idea on how does the enrichment at the interfaces vary with time, samples were extracted from each sample and studied under APT. The Mn distribution map for varying tempering time is show in figure. 5.8. It is evident from figure. 5.8 (e) is that before tempering no enrichment of Mn is observed in IA sample. Thereby confirming whatever peak concentration will be seen hereon, will be purely an outcome of mechanisms taking place during the tempering operation. Furthermore, it can be concluded form figure. 5.8 (e) that as the tempering time is increased the peak enrichment at the phase boundary increases. In order to account for the peak broadening, the machine learning code used in section 4.3 is employed here as well and the average composition at the interface is shown in figure. 5.9. It is important to mention here that only those parts of the interface were used to study the concentration where distinct crystallographic features like facets or dislocations were not visible. It is evident from the figure. 5.9 that there is a gradual increase in Mn enrichment at the phase boundary. The average Mn enrichment increased from ~14.2±1.56 at.% for T2 to 18.05±2.37 at.% for T50 samples, and finally for T200 samples the calculated enrichment is 20.25±2.57 at.%.

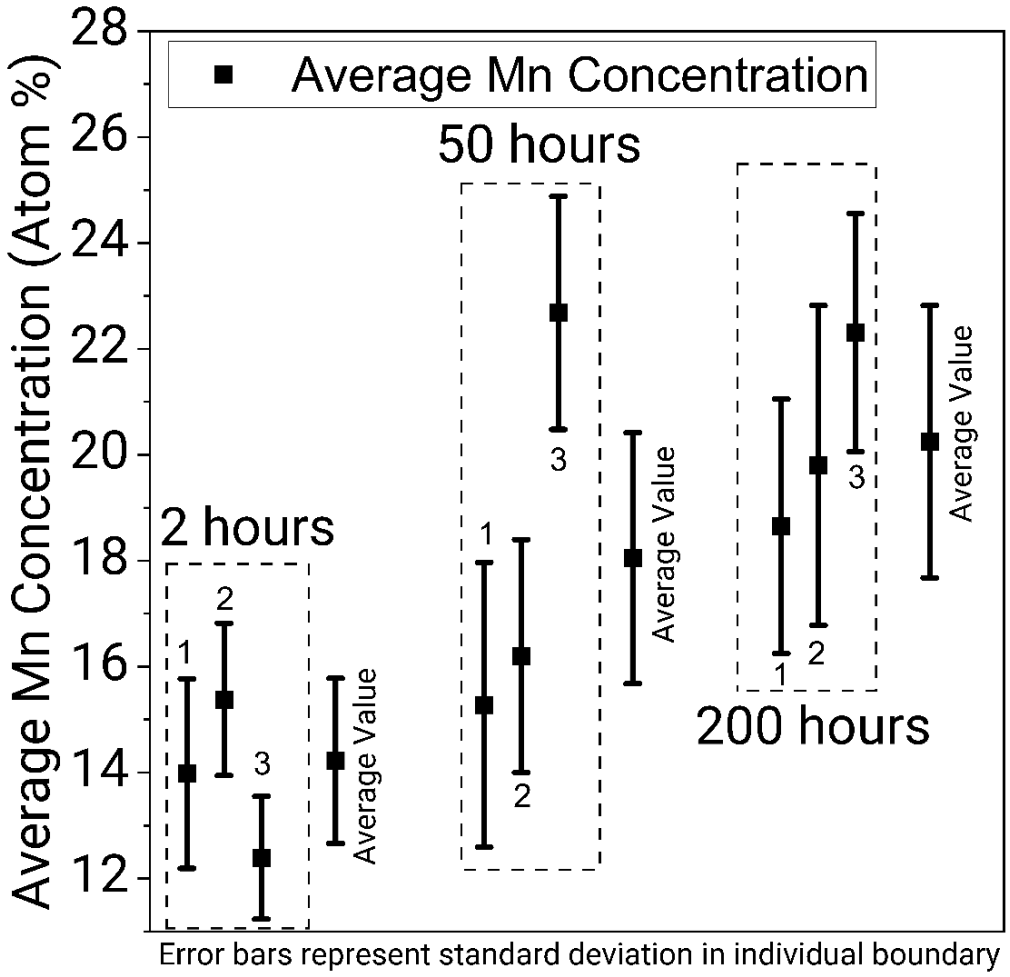

Figure 5.9 Average Mn enrichment at the phase boundary for different tempering time.

In order to understand the behavior of phase boundaries in terms of Mn enrichment, a DICTRA simulation was conducted for a moving phase boundary so that diffusion of elements between austenite and ferrite during tempering operation can be studied. Since PE and LENP mode of growth are not expected for the current experimental procedure [217], LE growth mechanism was used for the simulation. Starting input composition for the running the diffusion simulation were extracted from APT composition for IA samples. The obtained diffusion profile is depicted in figure 5.10. Prima facie, simulation results do not quite resemble the experimental results. With T2 samples showing highest enrichment of ~29.56 at.%, and then a slight decrease in peak concentration was observed (~29.3 at.% for T50 and T200 samples). As for T50 and T200 samples showed miniscule change in peak enrichment (0.03 mole percent) but the peak broadening is observed as well as phase boundary has moved into the austenite phase indicating ferrite growth. Since, DICTRA does not consider the equilibrium segregation at the phase boundary, the observed peak in concentration at the interface can only be an outcome of either local equilibrium or kinetic freezing.

There is significant difference in experimental observation and simulation results specially for T2 samples. Experimentally it is unviable for Mn, owing to slow kinetics at 450°C to show significant partitioning in just 2 hours of tempering. The origin of discrepancy lies in the local equilibrium mechanism included in simulation. The DICTRA module forces a local equilibrium at the interface and consecutively a sharp peak may appear for Mn even for T2 samples. Furthermore, the narrow peak observed for T2 sample, is also prone to errors as the module does not take the gradient energy into account which prevents peak narrowing [217]. Apart from local equilibrium considerations, kinetic freezing may also be playing a significant role in peak in Mn composition profile which at this stage cannot be concluded with full certainty.

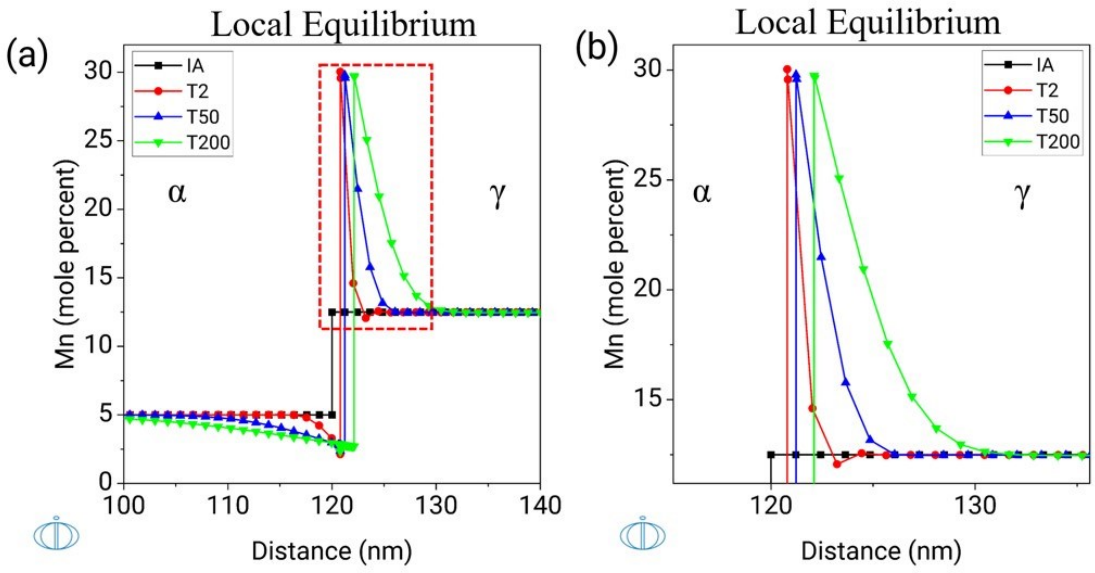

Figure 5.10 DICTRA simulation of Mn profile across the ferrite austenite phase boundary for (a) Local equilibrium condition, (b) Magnified portion of red box in (a)

5.3.5 Enrichment at the straight boundary features (misfit dislocations)

In Section 5.3.2, it is established that the features observed in straight phase boundaries are misfit dislocations. This section will discuss the segregation to these features. Dislocations provide favorable sites for equilibrium segregation owing to free spacing along the dislocation line. Variation of Mn segregation with tempering time, provides an idea on how does equilibrium segregation evolve with time. Figure 5.11(a) represents Mn segregation observed along misfit dislocations in T2 sample. Composition variation across different misfit dislocations is presented along ROI1 and the corresponding graph. It is evident from graph,

that for 2-hour tempering, quite weak segregation is seen at the misfit dislocations, i.e. 14.5 atom% along the enrichment lines. Meanwhile the base concentration is still the same as the bulk austenite Mn composition (~12.5 atom% Mn). For T50 samples, both the misfit dislocation segregation and the base line composition increase, with ~19 at.% of Mn observed a the dislocations, and ~14 at.% Mn at the base line composition. T200 sample showed a further increase in Mn segregation at the misfit dislocations (~21 at.%) and the base line composition reaching up to 16 at.%.

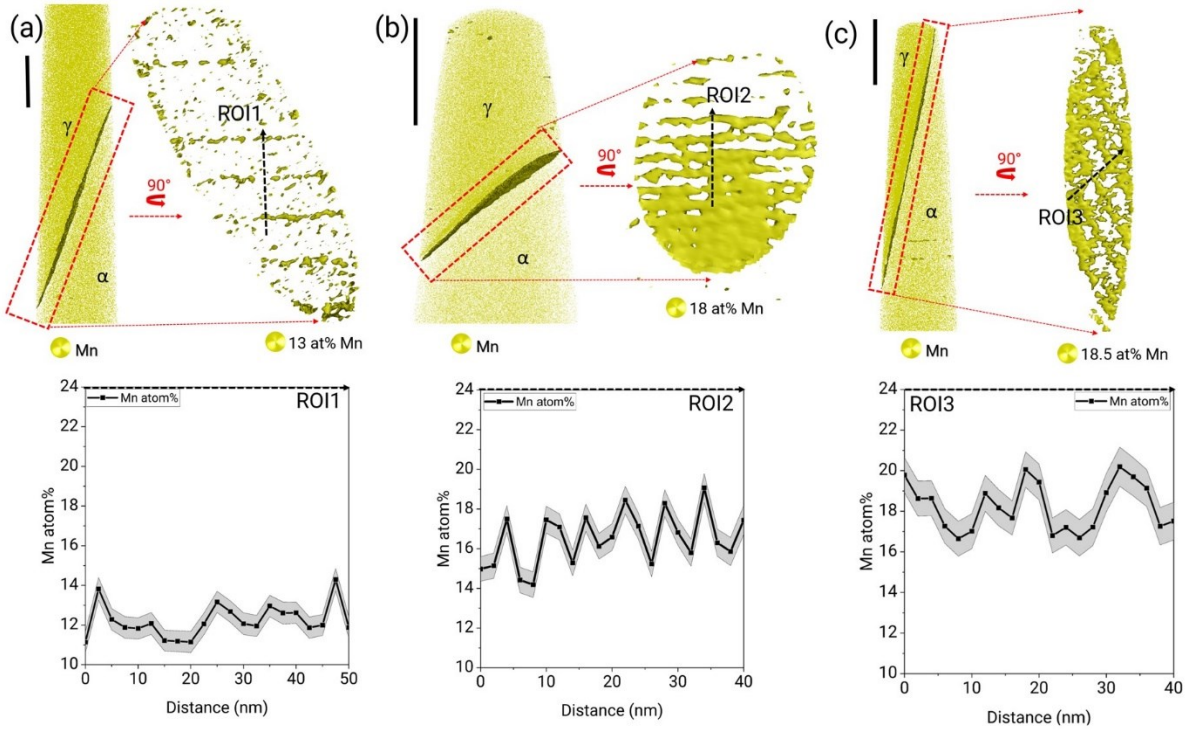

Figure 5.11 Mn enrichment along misfit dislocations in (a) T2, (b) T50 and (c) T200. (ROI ϕ=5nm) Scale is 50 nm

5.3.6 Segregation at curved phase boundary features (Superledges)

Superledges serve as the building blocks of multiatomic steps, aiding phase boundaries in traversing curvature. As mentioned in section 5.3.3 that these features can host Mn atoms either on their high index planes or at the facet junctions by the mechanism of equilibrium segregations. In this section, variation in Mn segregation in these superledges with tempering time will be discussed. Figure. 5.12 (a) shows a curved phase boundary for T2 sample, and the associated superledges and preferential linear Mn segregation with this boundary is shown in

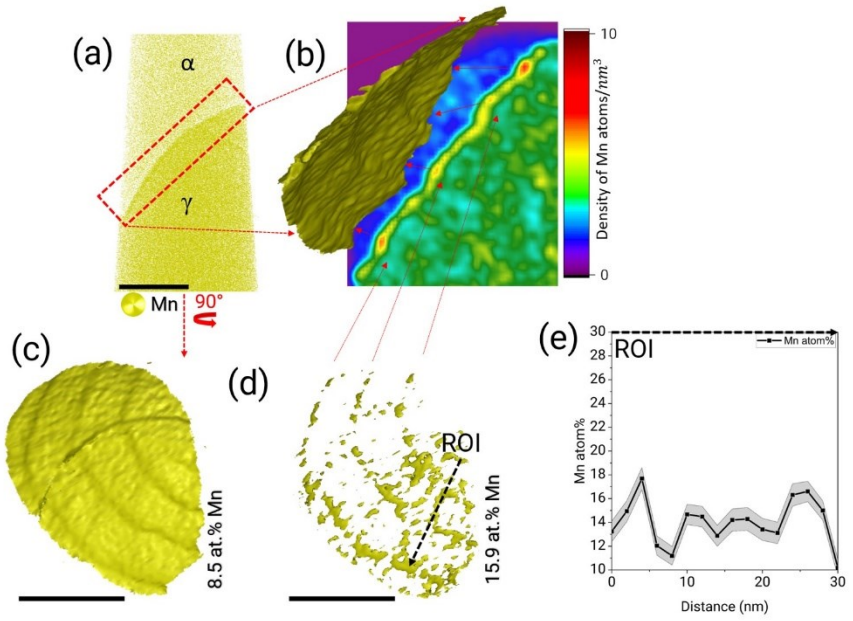

Figure 5.12 (a) Mn distribution map obtained from APT analysis showing α and γ phases with highlighted curved phase boundary for T2 sample, (b) Phase boundary with steps, (c) Significantly high Mn atoms along linear features, (d) Mn density map, (e) 1-D composition profile across the ROI (ϕ=5nm) shown in (d). Scale in (a, c, d) is 50 nm.

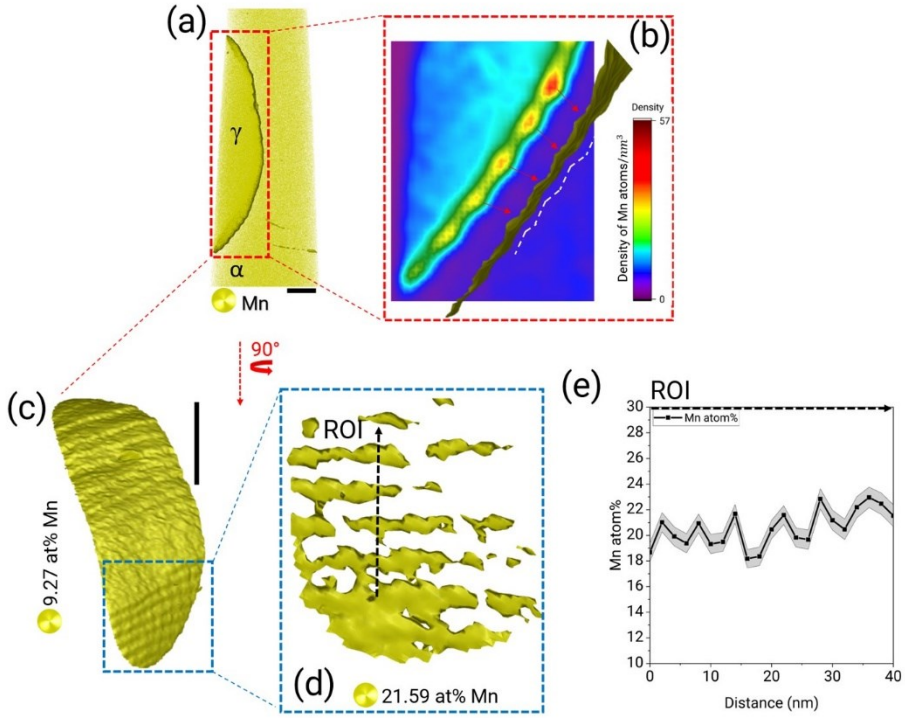

Figure 5.13 (a) Mn distribution map obtained from APT analysis showing α and γ phases with highlighted curved phase boundary for T50 sample, (b) Phase boundary with steps, (c) Significantly high Mn atoms along linear features, (d) Mn density map, (e) 1-D composition profile across the ROI (ϕ=5nm) shown in (d). Scale in (a) is 25 and (c) is 50nm .

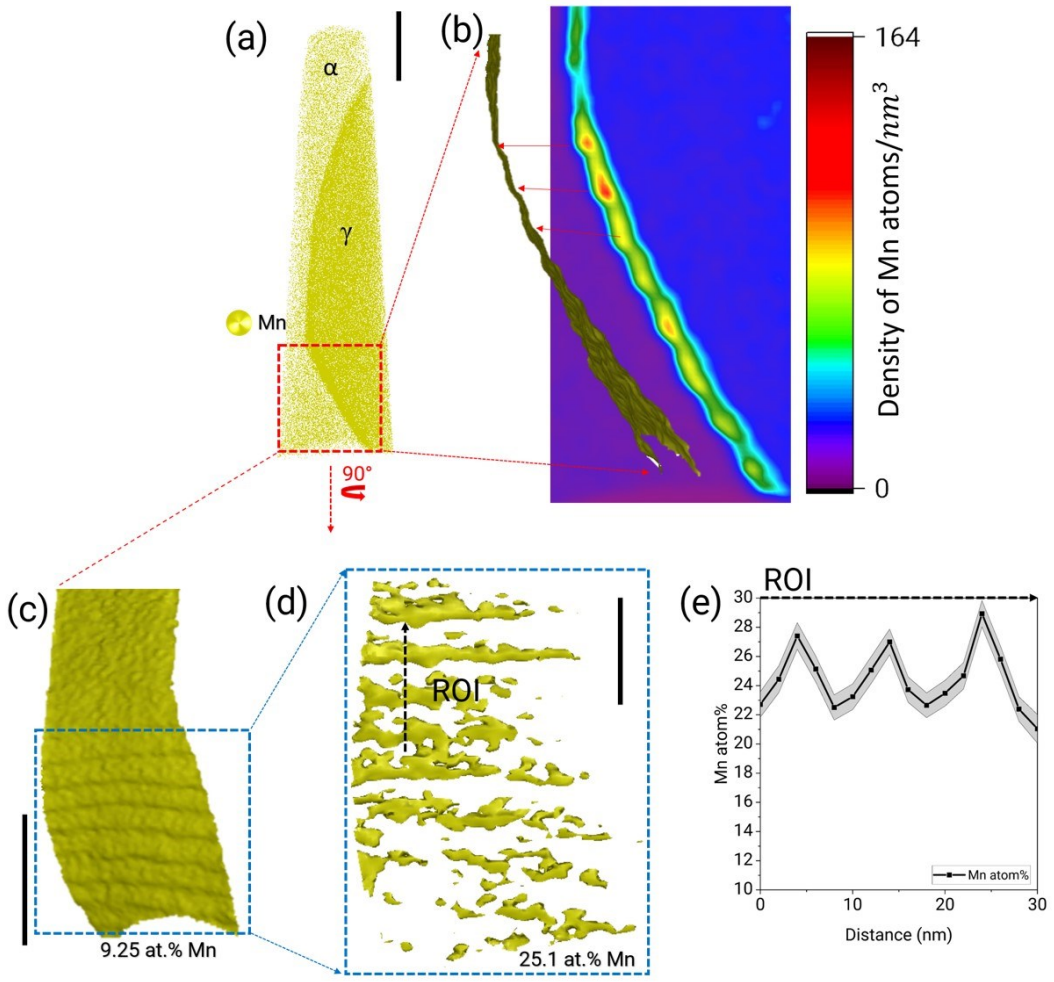

Figure 5.14 (a) Mn distribution map obtained from APT analysis showing α and γ phases with highlighted curved phase boundary for T200 sample, (b) Phase boundary with steps, (c) Significantly high Mn atoms along linear features, (d) Mn density map, (e) 1-D composition profile across the ROI (ϕ=5nm) shown in (d). Scale in (a) is 100 nm, (c) is 50 nm and (d) is 25 nm.

Figure. 5.12 (c) and (d) respectively. To get a better understanding, a density mapping of Mn atom is shown figure. 5.12 (b), with high density of Mn exactly at the superledge junction. In order to quantify the segregation an ROI is constructed across the linear Mn segregation and the composition profile obtained along the ROI is presented in figure 5.12 (e). Maximum segregation of ~18 at.% Mn is observed in the superledge. Meanwhile the base line concentration is ~11 at.% Mn. To get a trend of Mn segregation with tempering time, similar features were identified for T50 and T200 samples as well and the result is showcased in figure. 5.13 and 5.14 respectively with legends same as T2 sample in figure. 5.12. The density of Mn in super ledges shows a gradual increase, 10 atoms/nm^3 for T2 to 57 atoms/nm^3 in T50 and finally 164 atoms/nm^3 for T200. To quantify the segregation in superledges, ROI across linear features were constructed. It is evident from figure. 5.13 (e) and 5.14 (e), there is an increase

in peak Mn segregation along superledges (23 at.% for T50 and 29 at.% for T200). Apart from Mn segregation along the superledges, base line Mn concentrations is also witnessed to have increase from 18 at.% for T50 sample to 22 at.% for T200 sample.

5.3.7 Equilibrium segregation Vs Kinetic freezing

Since equilibrium segregation at the phase boundary is expected to increase with tempering at lower temperature and time [9], comparing the increase in segregation to these features can provide with an insight into segregation states and their respective mechanism.

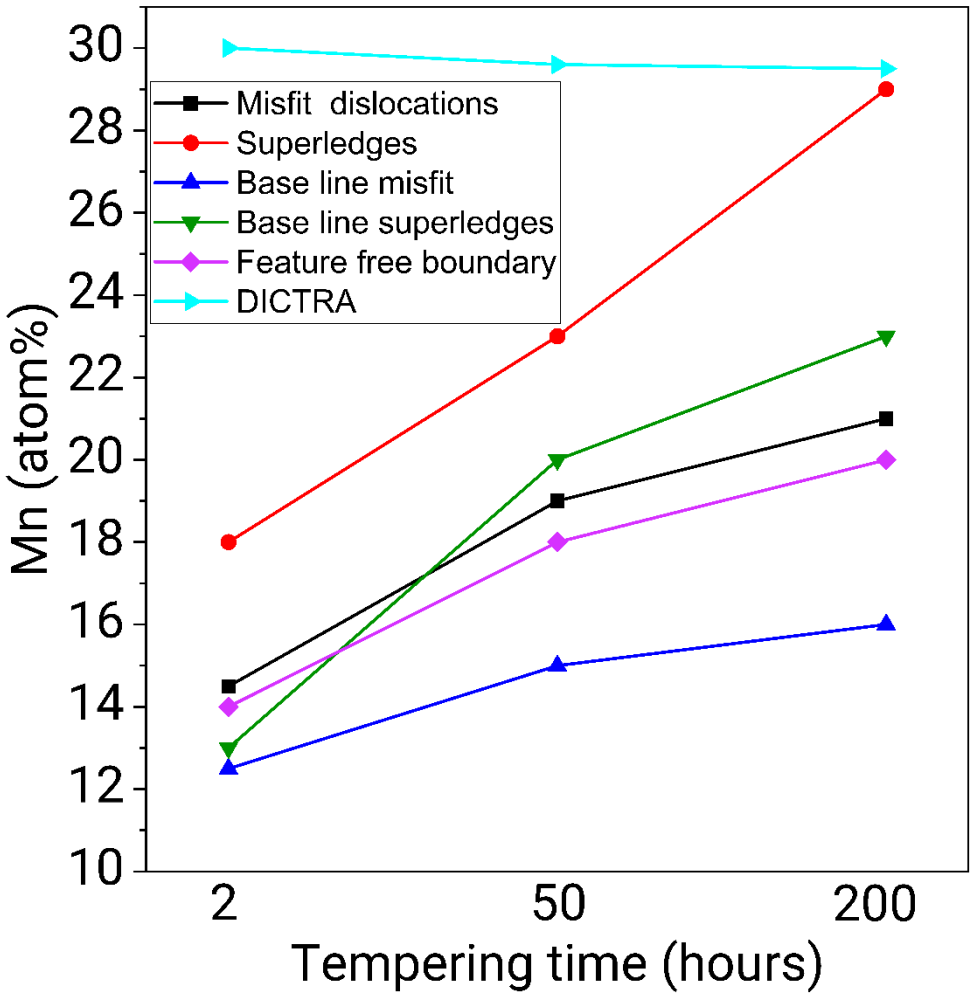

Figure 5.15 Variation of Mn enrichment with tempering time for different crystallographic feature observed experimentally and the peak composition extracted from, DICTRA module.

In figure 5.15, a compilation of enrichment values for different features (misfit dislocations, superledges, baseline, DICTRA prediction, and average values calculated from boundaries free from distinct dislocations or superledges) and conditions with time is presented. It is important to note that at 450°C, the diffusion of Mn in austenite is very slow. This low mobility primarily contributes to the accumulation of Mn at the phase boundary instead of its diffusion away.

The discrepancy between DICTRA predictions and the experimental observations can be understood as follows: the continued increase of Mn enrichment at the phase boundary with increasing time hints towards a kinetic transition from paraequilibrium (PE) - where there is no partitioning of substitutional elements - to a quasi-paraequilibrium partitioning mode (QPE). QPE is a condition where the system, constrained by kinetic limitations, exhibits slow diffusivity of substitutional elements, thus hindering the complete homogenization of solute distribution across the phase boundary or within the phase itself. The system is in a state between nonequilibrium and full equilibrium. Therefore, it is understandable why the experimental Mn enrichment is low in the early stages of tempering. During PE mode, no partitioning would have taken place, and with the kinetic transition, it starts increasing slowly, approaching the simulation value by 200 hours [218]. This also explains the rise in the enrichment baseline for both misfit dislocations and superledges, as well as for the composition obtained from feature-free portions of the phase boundary.

Another question may arise: although the diffusion of Mn is slow, why does diffusion away from the interface not increase significantly as tempering time approaches 200 hours? This can be understood by considering that the ferrite-austenite interface is moving throughout the experiment, which means a continuous flux of Mn atoms moves towards the interface, thereby maintaining the Mn peak. Thus, a metastable state exists where the phase boundary continues to accumulate Mn due to the ongoing phase transformation. Theoretically, if the timescale of the experiment were indefinitely extended and no additional Mn were introduced to the interface, the Mn peak would eventually disappear as diffusion away from the interface would then balance the concentration gradient. However, in practical scenarios, this time could be quite long.

As for the segregation in dislocations and superledges, Mn segregation in these features tends to stabilize the concentration profile by acting as sinks and trapping Mn because of their strain fields and binding energy. These dislocations can also act as additional pathways for Mn diffusion, behaving as a persistent source of Mn for the phase boundaries and continually feeding Mn to them. It is important to note that maximum segregation of Mn is witnessed at the superledges for T200 samples. This means that the superledge’s concentration is fast approaching the steady-state condition specific to the local environment of the phase boundary and is achieving local thermodynamic balance with the surrounding matrix.

5.4 Conclusion

In this research, an investigation was conducted to study the behavior of Mn segregation in Fe–C–Mn-Al medium Mn steel at 450°C, focusing on the role of phase boundaries features on the enrichment behavior of alloying elements. The study reveals several important observations regarding the thermodynamic and kinetic processes governing the solute redistribution in this system.

1. The straight phase boundaries contain misfit dislocations with a mixed character. These dislocations serve as effective sites for Mn segregation.
2. Curved phase boundaries are characterized by the presence of superledges. These superledges are decorated by Mn segregation, although the true position of this segregation is not known (i.e. is it at the junction or at one of the facet planes). Notably, the Mn segregation at superledges approaches near-local equilibrium with the matrix, highlighting their importance in achieving localized thermodynamic balance.
3. Mn segregation is observed in both misfit dislocations and superledges and at the phase boundaries without any distinct crystallographic feature. The extent of segregation is influenced by the feature that decorate the phase boundaries. While Mn segregation at superledges reaches near-local equilibrium, the overall phase boundary does not attain local equilibrium due to kinetic constraints at 450°C.
4. The phase boundary as a whole exhibit a quasi-paraequilibrium state. This state is characterized by partial equilibrium where fast-diffusing species like carbon may attain local equilibrium, but slower-diffusing Mn remains kinetically constrained. This results in an Mn spike at the Phase boundary that is lower than the local equilibrium partitioning peak value.

6. Effect of external magnetic field on Mn segregation at α/α grain boundaries

6.1 Introduction

Grain boundaries are two-dimensional defects where two or more regularly arranged atomic lattices meet. When the abutting crystals have different orientations with respect to each other, there exist a local structural disregistry due to the lattice mismatch and a resultant excess energy which is generally reduced by equilibrium segregation [219-221]. Segregation at grain boundaries usually leads to varying outcomes. To begin with, enhanced cohesion at the interface can be achieved through dislocation pinning or stabilization of the boundary, such as when boron occupies high-energy sites. Furthermore, segregation at the grain boundary can be a precursor to phase transformation. Additionally, segregation may promote formation of second phases at the enrichment boundary (complexion, precipitation or boundary phase formation). Segregation at the grain boundaries is conceivable through following measures: inherent elemental decoration from previous thermomechanical processing (enrichment in prior austenite grain boundaries) or upon tempering after quenching (at ferrite grain boundaries) [117, 128, 133, 139, 222].

In recent years, annealing in tandem with magnetic field (MF) with or without in synergy with strain has gained significant importance. Inherent material characteristics like susceptibility, lattice structure etc. react differently to external field which helps in realizing a multitude of interesting microstructural features and enhanced mechanical properties [223-226]. Monte Carlo simulations of HCP systems revealed that susceptibility difference between basal plane and c-axis influence the microstructure evolution albeit qualitatively [227]. It was further reported that permeability difference between matrix and product phase has an effect on the precipitation of the latter. Lower permeability of the product phase than the matrix inhibits its precipitation and vice versa [29]. High external magnetic field (120-kOe) presents an opportunity to increase the tensile strength (~6%) and Brinell hardness, by increasing the carbon content of the matrix and inhibiting primary cementite precipitation [228]. It was reported for ferromagnetic substitutional alloying elements (Co, Ni), external field reduces the diffusion coefficient as with magnetic field, ordered arrangement of atoms makes the atomic

jump difficult [27]. For carbon, annealing above the Curie temperature the diffusion coefficient and distance both increased with increasing field strength [24].

Lately, the concept of magnetic annealing has been extended to grain boundaries as well [229]. Magnetic field processing has been reported to increase the frequency of low Σ and low angle grain boundaries. Furthermore, a field of 8T resulted in an increased sharpness in texture which further enhanced the occurrence of low Σ boundaries [230-232]. In Ni with a nanocrystalline microstructure, magnetic annealing successfully helped suppress the abnormal grain growth [233, 234].

Considering the significant impact of magnetic annealing in altering grain boundary properties and the crucial role of boundary segregation in enhancing the mechanical performance, the field effect on boundary segregation is worth investigating. So far there has been only one study reported for the field effect on tin segregation in Fe-Sn alloy, and it reported that segregation decreases with the introduction of a field during annealing [235]. But a similar study is missing for Fe-Mn alloys. Several articles do study the effect of a field on the transformation temperature in Fe and Fe-C alloys and associated energetic study [23, 28, 29, 228, 236-238], but the effect of a field on segregation that eventually forms the precursor for transformation is still required. In subsequent sections, an investigation is made to understand experimental observation by complimenting it with reported energetics analysis.

6.2 Methods

6.2.1 Experiment

The Fe-8Mn wt% alloy was subjected to an annealing process at 450°C for 5.5 hours, both in the presence of a 9 Tesla magnetic field and without the field. The heating and cooling rate used was 20 K/min. After the annealing treatment, the subsequent segregation of Mn at the ferrite grain boundaries was studied using Atom Probe Tomography (APT).

The magnetic response was evaluated using the Quantum Design Magnetic Property Measurement System (MPMS) equipped with a standard Vibrating Sample Magnetometry (VSM) option. For these measurements, cuboid specimens with dimensions of 3 mm × 2 mm × 1 mm (length × width × thickness) were used.

6.2.2 Calculations

6.2.2.1 Magnetization

Application of a magnetic field, aligns the magnetic moment of a ferromagnetic material in a direction parallel to the applied external field. This increases the exchange interaction and further enhances the magnetization. Using Weiss molecular field theory [28, 238, 239], magnetization (M) can be expressed as:

$$M = NmB_j(\alpha) \tag{1}$$

where

$$B_j(\alpha) = \frac{2j+1}{2j}\coth\left(\frac{2j+1}{2j}\alpha\right) - \frac{1}{2j}coth(\frac{1}{2j}\alpha) \tag{2}$$

$$\alpha = \frac{m(H+\lambda M)}{kT} \tag{3}$$

$$\lambda = \frac{3jkT_c}{Nm^2(j+1)} \tag{4}$$

In above equations, N corresponds to Avogadro's constant, H is the intensity of an applied external magnetic field, λ is the molecular field constant, k is the Boltzmann constant, T_c is the Curie temperature, T is the temperature of annealing, m is magnetic moment of the phase and j is the quantum number referring to atomic angular momentum. Referring to previous reported values j will be used as 1 [238, 239].

For paramagnetic phase, the magnetization is given by [240]:

$$M = N\mu\mu_b B_j(x) \tag{5}$$

Where x takes the form [241],

$$x = \frac{\mu\mu_b H}{kT} \tag{6}$$

For small x, the Brillouin function can be approximated $B_j(x) \approx x$ [242]. N is Avogadro's number, μ is Bohr magneton number, μ_b is Bohr magneton, H is applied external field, k is k is Boltzmann constant and T is annealing temperature.

6.2.2.2 Thermodynamic calculation

The Gibbs free energy of a ferromagnetic material consists of two components: Chemical contribution and magnetic contribution.

$$G^{\phi}_{Total} = G^{\phi}_{chem} + G^{\phi}_{mag} \quad (7)$$

The magnetic field energy further can be described as a combination of external and internal magnetic free energy.

$$G^{\phi}_{mag} = G^{\phi}_{mag,in} + G^{\phi}_{mag,ex} \quad (8)$$

Where $G^{\phi}_{mag,in}$ is expressed as (by Hillert et al. [243]):

$$G^{\phi}_{mag,in} = RTln(ß + 1)f(\tau) \quad (9)$$

Here $\tau = T/T_C$ and ß concerns with gross magnetic entropy and will be considered to be molar Bohr magnetic moment. For $\tau \leq 1$ the function $f(\tau)$ takes the following form [243]:

$$f(\tau) = 1 - \frac{1}{A}\left[\frac{79\tau^{-1}}{140P} + \frac{474}{497}\left(\frac{1}{P} - 1\right)\left(\frac{\tau^3}{6} + \frac{\tau^9}{135} + \frac{\tau^{15}}{600}\right)\right] \quad (10)$$

and for $\tau > 1$ it becomes:

$$f(\tau) = -\frac{1}{A}\left(\frac{\tau^{-5}}{10} + \frac{\tau^{-15}}{315} + \frac{\tau^{-25}}{1500}\right) \quad (11)$$

$$A = \frac{518}{1125} + \left(\frac{11692}{15975}\right)\left(\frac{1}{P} - 1\right) \quad (12)$$

For bcc, P is 0.4 and for other structures 0.28. As for $G^{\phi}_{mag,ex}$ the energy can be approximated as [238]:

$$G^{\phi}_{mag,ex} = -\int_0^H MdH \quad (13)$$

6.3 Results

6.3.1 Influence of magnetic field on segregation

The influence of a magnetic field on the segregation behavior of Mn during annealing can be understood by studying the APT reconstruction of the analyzed tips. Figure. 6.1(a) shows an IPF map depicting a random high angle grain boundary. The respective Mn distribution map across the entire volume of the tip and with the grain boundary highlighted with segregation of Mn is presented in figure 6.1(b). This data set belongs to sample annealed at 0T. To quantitatively estimate the composition an ROI was constructed across the highlighted Mn iso-

surface and the segregation value turns out to be ~18 at%, whereas it was around 7.5 at%. in grain interiors (figure. 6.1c). For samples annealed with a field of 9T, the results are depicted in figure. 6.1(d) through (e), where (d) shows the IPF map of the apt tip highlighting the random high angle grain boundary and its corresponding Mn distribution map with Mn segregation at the grain boundaries depicted using iso-surface. The 1-d concentration profile to study the concentration across the boundary, was drawn along the ROI2 and result is shown in figure. 6.1(f). The peak enrichment of ~17 at% is observed and the bulk composition observed is ~8 at%. In order to get an in-plane composition values, similar steps were taken as mentioned earlier (section 4.3) for previous APT analysis. The average in-plane composition for 0T sample is 18.10±1.23 at%, for 9T sample, it is 18.3±1.2 at%. It is clear from comparison between samples annealed at 0T and 9T that the segregation in both conditions is almost similar (within margin of error) in both the conditions.

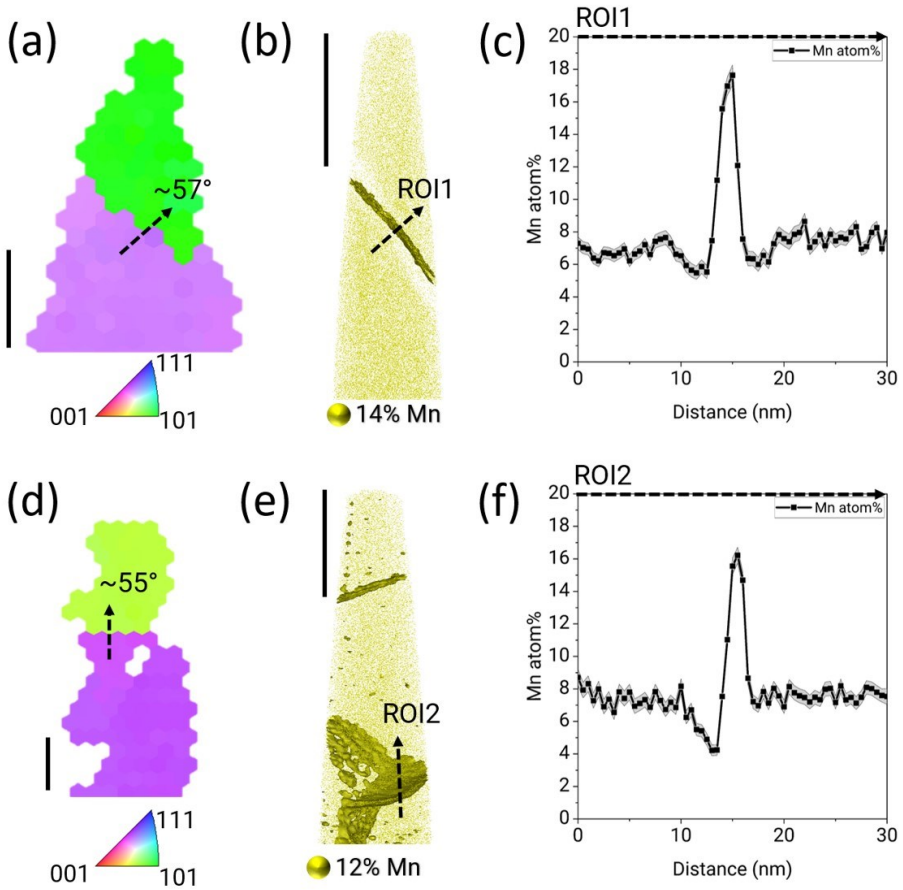

Figure 6.1 IPF map showing random high angle grain boundaries in samples annealed at (a) 0T and (d) 9T. Mn distribution map achieved through APT analysis for (b) 0T and (e) 9T; (c) and (e) 1-d Composition profile of Mn along the ROI1 (ϕ=15nm) and ROI2 (ϕ=15nm) depicted through arrows in (b) and (e) respectively. The scale is 50nm

To have a better statistic and understanding of segregation trends, several other tips were studied. The in-plane Mn concentration analysis is conducted using an open-source machine learning code [159] [159]. Figure. 6.2 shows the average in-plane Mn concentration at the grain boundaries. There is significant scatter in the data not just between different field strengths but within one field strength as well. While it is evident that the average Mn concentration from 0T varied from 11.74±1.8 at.% to 24.46±6.13 at.%, for 9T it varied from 11.36±2.28 at.% to 23.71±1.19 at.%. The average boundary segregation of Mn for 0T is 17.78±2.96 at.% and for 9T it is 16.68±1.9 at.%. From initial observations it appears that a magnetic field has no influence on the segregation tendency of Mn at the random high angle grain boundaries. This observation is contrary to what was observed for Fe-0.8 at.% Sn, where annealing in presence of magnetic field (6T) resulted in a decrease in segregation [235].

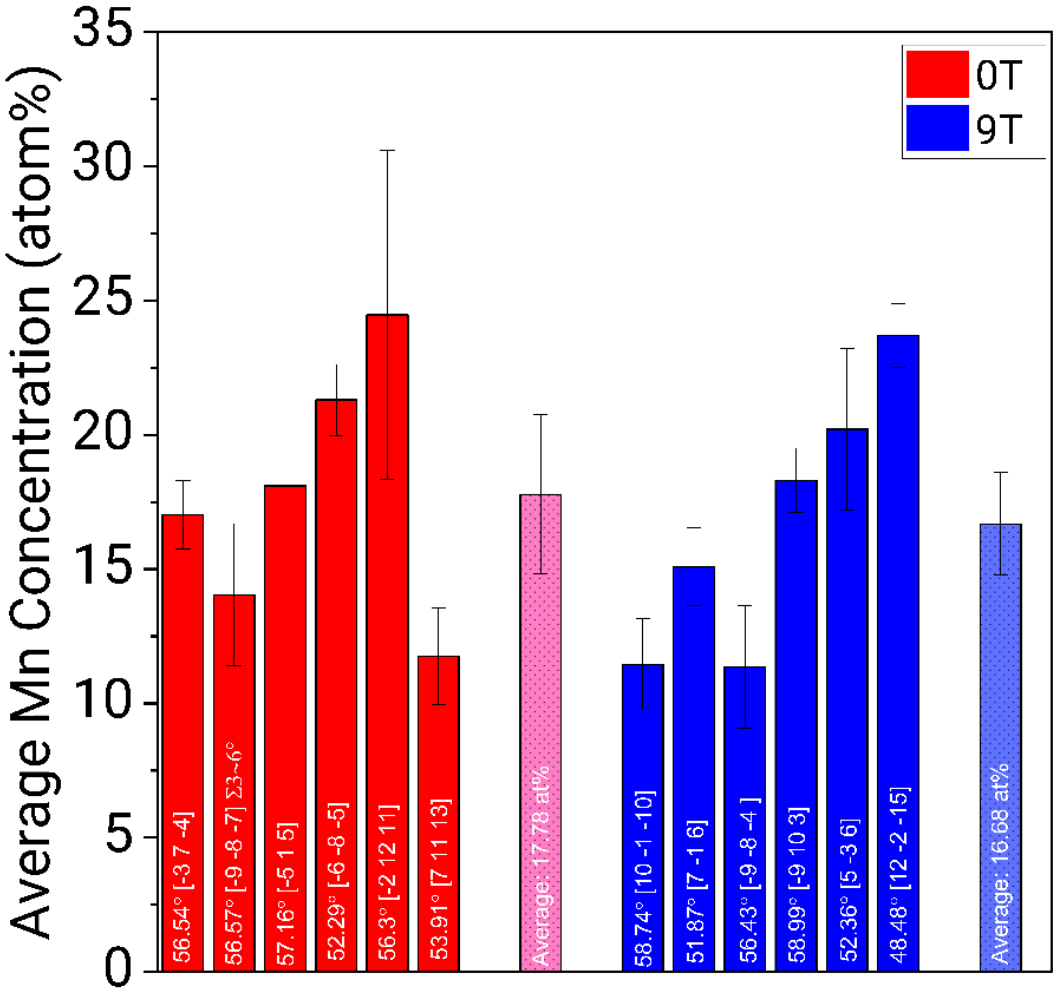

Figure 6.2 Variation in in-plane enrichment of Mn at the grain boundary based on the misorientation angle and field strength. (The standard deviation is for individual phase boundaries)

6.3.2 Highly enriched Mn phase

Figure. 6.3(a) shows a highly enriched Mn phase precipitating at the grain boundary which had irregular shape and appeared as a perturbation in the grain boundary. Even after the iso surface value is increased, the particles are still visible and maintained their irregular shape (figure. 6.3b). For through thickness composition of the particles an ROI was drawn across one of the particles and the composition profile is shown in figure. 6.3(c). Mn composition of the

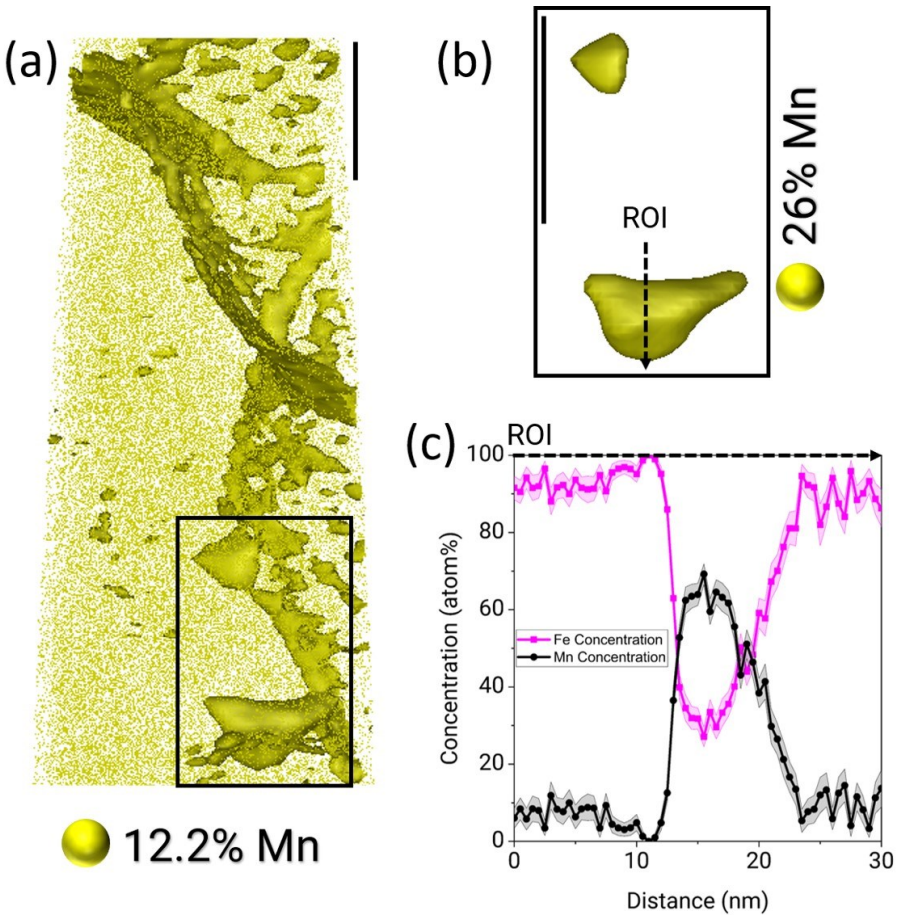

Figure 6.3 (a) Mn distribution map of sample annealed at 450°C for 5.5h under a 9T magnetic field, (b) Magnified image of α manganese particles shown enclosed in (a), (c)1-d composition profile across the α manganese particle (ROI:ϕ=2nm). The scale is 25nm.

particle is as high as ~60 at%, and most probable explanation for observing these particles is precipitation of α-Mn which also tend to have such high concentration of Mn albeit at much lower temperature (250°C) for this alloy composition.

6.4 Discussion

6.4.1 Effect of external field on Mn segregation

To better understand segregation behavior, the effect of an external magnetic field on the Gibbs energy of individual phases is compared with the free energy curves obtained without an external field. The magnetization of each phase is calculated according to their magnetic character: equation (1) for the ferromagnetic phase and equation (5) for the paramagnetic phase, as presented in figure. 6.3 (a) and (b). It is evident that only ferrite exhibits a change in free energy, and that change is minuscule. The external magnetic field reduces the free energy of ferrite in Mn-rich regions, but the effect diminishes with increasing Mn content. While ferrite shows some differences, the Gibbs energy of austenite and α-Mn remains largely unaffected by the external field.

A question arises: how does the external magnetic field affect grain boundary energy, which further influences segregation tendencies? Currently, there is no theoretical model available to study the effect of the magnetic field on grain boundary energy. The understanding is further complicated by the increase in magnetic moments due to the free volume in the grain boundary. It is worth mentioning that, due to its structure, the grain boundary is bound to have different magnetic characteristics than the bulk, especially the Curie temperature. Hegde [141] established that the Curie temperature of the grain boundary in an Fe-Mn binary alloy is approximately 208°C lower than that of the bulk and decreases at a rate of 12°C per Mn%. Considering this rate of Curie temperature reduction, the annealing temperature is well above the Curie temperature of the grain boundary for all observed segregation values. Thus, we are in a situation where the grain boundary is paramagnetic, and the bulk is ferromagnetic.

An important factor in understanding this outcome is the Curie temperature of the bulk ferrite. The applied 9 Tesla magnetic field was insufficient to significantly alter the Curie temperature of the bulk ferrite, changing it by only about 3°C. Since the change in the magnetic properties of the ferrite bulk drives the segregation behavior at the grain boundaries, the minimal impact on the Curie temperature means that the segregation energy conditions at the grain boundaries remained largely unchanged.

The underlying reason for this lack of effect lies in the magnetic character of the system. The reported [244] segregation energy for a completely paramagnetic system (paramagnetic bulk + paramagnetic grain boundary) is -0.1eV (figure. 6.4b). Whereas for the case of ferromagnetic bulk and paramagnetic boundary (0T), it is -0.40 eV (figure. 6.4b). As mentioned earlier for

applied annealing temperature, the bulk and grain boundary have ferromagnetic and paramagnetic character. Therefore, for a noticeable change in segregation behaviour to occur, both the bulk ferrite and the grain boundary would need to transition to a paramagnetic state. Such a transition would alter the segregation energy conditions at the grain boundary, potentially affecting Mn segregation. However, the annealing temperature, field strength, and alloy composition are not favourable for such a transition. For the given annealing temperature, the minimum bulk Mn composition should be approximately 22% for its transition to a paramagnetic state (Curie temperature 445°C). As a result, both bulk and grain boundary would have paramagnetic characteristics. To transform the bulk into a ferromagnetic state, the external field strength should be at least 20T, resulting in a Curie temperature increase of 6°C. Thus, there is a possibility that an external field could change the overall character of the system, with the bulk becoming ferromagnetic and the grain boundary remaining paramagnetic, as opposed to the absence of the field. Hence, the difference in segregation energy between the two cases (-3eV) will come into effect and manifest as Mn segregation at the grain boundaries.

Another possibility to witness a change in segregation behaviour for the same alloy as used in earlier experiments is by increasing the annealing temperature to 648°C (the Curie temperature for Fe-8Mn wt.% is 647°C; para bulk + para grain boundary). If an external field of 9T is applied, an increase in Curie temperature can be observed, transforming the bulk to a ferromagnetic state and changing the segregation energy. However, a higher annealing temperature requires much shorter annealing times to prevent austenite nucleation, which would absorb Mn from neighbouring ferrite grain boundaries, making it difficult to comment on the segregation behaviour of the grain boundaries and its relation to the magnetic field. Additionally, the proximity of the annealing temperature to the Curie temperature of the bulk presents added complexity, as oscillations are commonly observed during the holding time of annealing. While oscillations themselves do not pose problems, the risk is that during holding, the bulk may alternately be in a ferromagnetic or paramagnetic state. Therefore, it would be very difficult to comment on the segregation behaviour of such a sample.

Considering above mentioned scenarios, the only possible way to witness a change in segregation with the application of an external field is by increasing the field strength. A high field strength will also help in selecting a much higher annealing temperature for a given alloy composition. Since with increasing field strength the Curie temperature is also increased. Thereby avoiding the associated problem of temperature oscillations witnessed during the holding time.

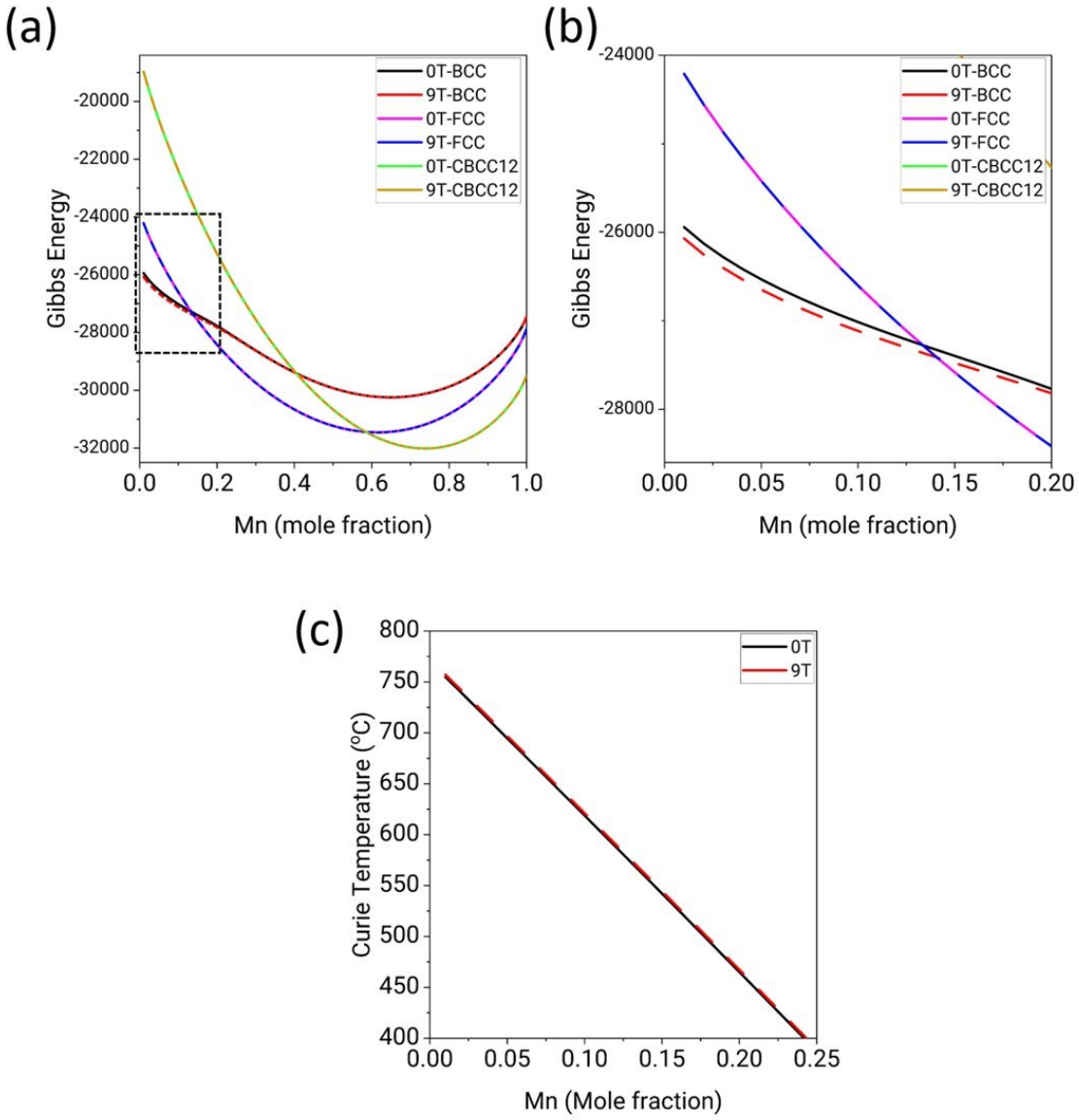

Figure 6.4 (a) Gibbs energy change with magnetic field and Mn content, (c) Change in Curie temperature with Mn content and external field in Mn-rich region of ferrite.(Primary data is extracted from Thermocalc, database TCFE11)

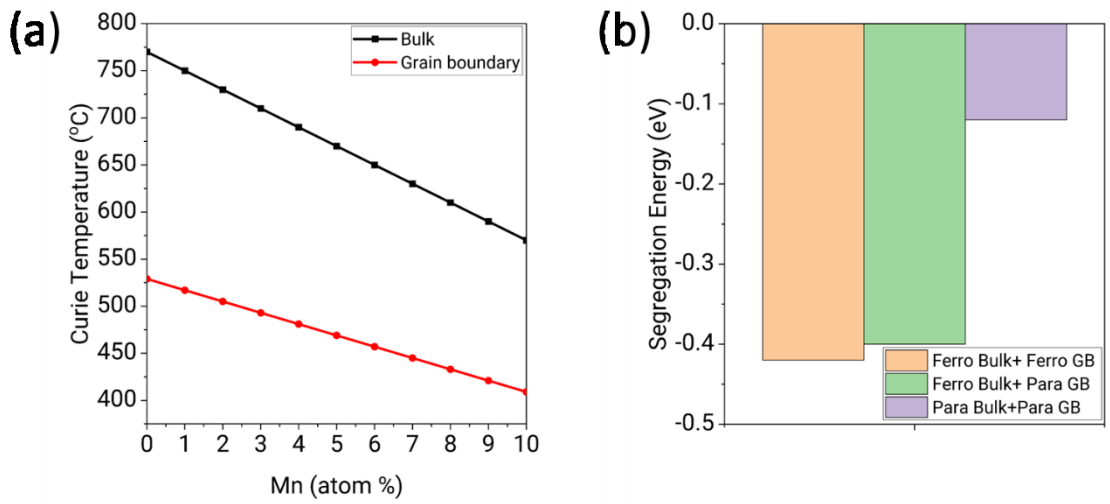

Ref: O. G. Hegde, "Ab initio based study of magneto-chemo-structural coupling in complex alloys," 2022.

Figure 6.5 (a) Change in the curie temperature of bulk and grain boundary with Mn content, (b) Segregation energy for Mn segregation with different magnetic character of bulk and grain boundary [244].

6.4.2 α-Mn precipitation

α-Mn is stable only up to 249°C, which is around 200°C below our annealing temperature. Observing α-Mn particles in samples annealed at 9T at this temperature contradicts Thermocalc calculations, which predict that only austenite and ferrite can exist at 450°C. The Gibbs energy plot clearly shows that α-ferrite can only be in equilibrium with austenite (figure. 6.6a). Even the introduction of a magnetic field decreases the free energy by a negligible amount, which is insufficient to stabilize α-Mn with α-ferrite.

However, if we consider that austenite has not yet nucleated, then α-ferrite can be in equilibrium with α-Mn, and the observed composition is very close to what is predicted by Thermocalc (i.e., 8 wt.% Mn in α-ferrite and ~54 wt.% Mn in α-Mn; figure. 6.6b). This is also evident from the phase evolution in the presence and absence of austenite (figures. 6.6b and c). With austenite included in the calculation, α-Mn vanishes above ~247°C, while when austenite is excluded, α-Mn is seen to exist until 450°C, albeit in near-zero quantity.

Considering the heating rate (20 K/min) during the annealing process, it is possible that α-Mn could have nucleated during the early stages of heat treatment and became susceptible to dissolution as the annealing progressed. Currently, there is no information available regarding the effect of external fields on interface and boundary energy and subsequently on the kinetics of austenite nucleation. Therefore, to comment on austenite nucleation, triple junctions are

studied, as they have been reported to be one of the primary sites for nucleation [198]. Figure. 6.7 shows the triple junction for samples annealed with a field strength of 9T. The Mn enrichment was around 20 at.% at the triple junction, much lower than what is expected for austenite nucleation, even for a grain boundary phase [198]. In the absence of austenite, it is possible that locally, α-Mn could have remained stable even at 450°C with α-ferrite, albeit in very small quantities.

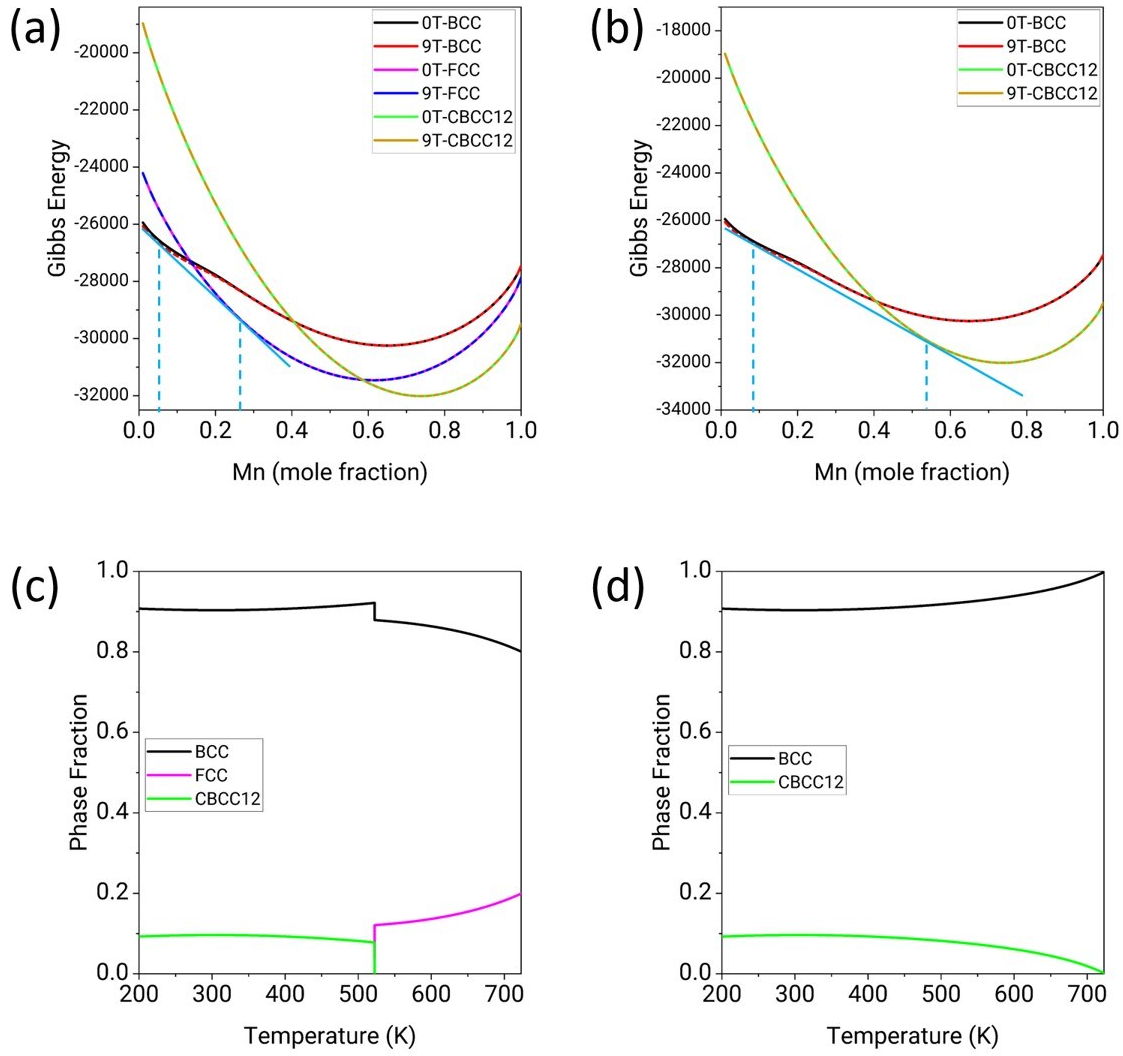

Figure 6.6 (a) Gibbs energy plot for different phases, (b) Gibbs energy plot in the absence of austenite, (c) Phase evolution with temperature, (d) Phase evolution with temperature without austenite.

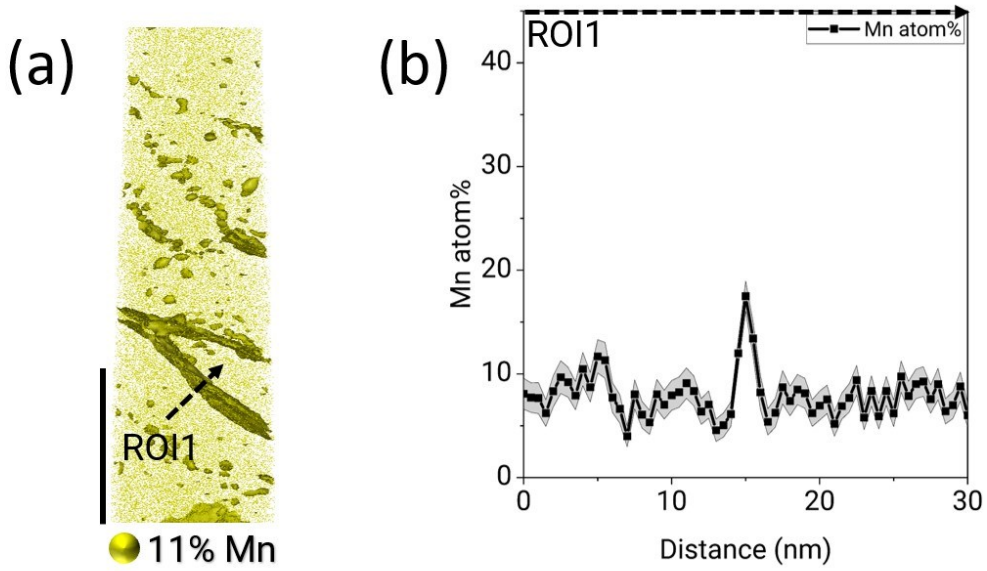

Figure 6.7 Mn distribution map for sample annealed at 9T field, (b)Composition profile across ROI1 (ϕ=5nm). Scale in (a) is 50 nm.

6.5 Conclusion

The effect of a magnetic field on the annealing of an Fe-8Mn (wt.%) binary alloy at 450°C was investigated. The results indicate segregation of Mn at the ferrite grain boundaries under both conditions (0T and 9T); however, no change in the intensity of segregation was observed due to the applied external magnetic field.

This observation is attributed to the magnetic properties of the bulk and the grain boundaries at the annealing temperature. At 450°C, the bulk is in a ferromagnetic state, while the grain boundaries are in a paramagnetic state. The only possible way to witness a difference in segregation is by employing really strong field strength (~30T) and a higher annealing temperature than use in the present experiments. The higher annealing temperature will help in avoiding the oscillations near the Curie temperature. Thus, it will be possible to have a paramagnetic system without field and a ferromagnetic bulk and paramagnetic grain boundary with introduction of external magnetic field. Which in turn will manifest itself in a much negative segregation energy for magnetically annealed samples and subsequent increase in Mn segregation at the ferrite grain boundaries.

7. Conclusion and outlook

7.1 Conclusion

The thesis aimed to identify and understand the solute decoration state at the phase boundary, along with the associated thermodynamics and kinetics, in a Fe-10Mn-3Al-0.2C (wt.%) medium manganese alloy. The alloy was fully austenitized, followed by intercritical annealing (700°C for 0.5 hours) and low-temperature annealing at 450°C for 2, 50, and 200 hours. To assess the effect of an external magnetic field on the segregation of paramagnetic solute (Mn) in a ferromagnetic system (Fe), annealing was conducted on a Fe-8Mn (wt.%) binary alloy with and without a 9T field. The results of these investigations are divided into three separate chapters, and a brief summary is presented below:

1. Chapter 4 addressed the heterogeneity in solute enrichment within a microstructure characterized by laminated austenite and ferrite with a Kurdjumov-Sachs (KS) orientation relationship between them. For a triple junction with two phase boundaries (PB) and a grain boundary (GB), one of the PBs was observed to be depleted of carbon (C), while the other PB exhibited depletion near the triple junction. This behaviour can be understood as follows:
    a. The observations indicate that GB acts as an extracting agent for C, effectively depleting C from the adjacent phase boundary.
    b. To determine if there is any difference between the character of the two PBs, a separate study was undertaken on a microstructure that exhibited diverse OR between phases, ranging from KS to near KS. It was observed that even though the OR between adjacent phases varied, it did not affect the enrichment of C at these boundaries. Thus, the C depletion observed in the PB is primarily due to its direct connection to a GB at the triple junction.
    c. This idea is further supported by ab-initio calculations, which predicted that the segregation energy of C, at austenite/austenite grain boundaries (-0.91 eV) is much more negative than at the austenite/ferrite phase boundary (-0.74 eV).
    d. A peculiar observation was made regarding phase boundaries with misorientation as low as ~10°. Although the TKD of the APT tip showed two different phases, there was no observed difference in the Mn composition in

either grain. It was found that this boundary was originally a low-angle grain boundary between two neighboring austenite grains, and due to one grain being depleted of C, it transformed into massive ferrite during quenching after tempering.

2. Chapter 5 discusses in detail the Mn distribution states at the phase boundary, as well as the associated crystallography, thermodynamics, and kinetics of the observed enrichments. Following tempering, it was observed that Mn segregated linearly and periodically in the plane of the phase boundary. Crystallographic analysis of these linear features revealed the following observations:
    a. The linear segregation of Mn present at the straight phase boundaries is associated with misfit dislocations having mixed character. These dislocations exist due to the deviation from the parallel configuration of close-packed planes.
    b. At phase boundaries with curvature, Mn is observed to have segregated along the superledges composed of multiatomic facets. These facets are characterized by one set of high-index planes and another set belonging to the GT' type irrational plane configuration.
    c. As for the average Mn enrichment at the phase boundary, it increased with increasing tempering time. This is because the partitioning in the early stage of tempering followed a quasi-paraequilibrium mode, and as time progressed, it began to approach local equilibrium partitioning. Consequently, an increase in Mn enrichment was observed.
    d. Superledges presented a unique situation where the Mn concentration at these defects approaches equilibrium with the surrounding matrix faster than at other defects, thereby stabilizing these defects relative to the surrounding matrix.
3. Furthermore, the magnetic field does not cause a variation in Mn segregation at the ferrite grain boundaries. The ineffectiveness of the magnetic field arises from the fact that, at the annealing temperature, the grain boundary exhibits paramagnetism while the bulk ferrite experiences ferromagnetism. For the annealing temperature in consideration, the magnetic field strength does not alter the magnetic state of the system. Any change in grain boundary segregation can only be observed if the temperature is high enough for the bulk to transition to a paramagnetic state and the field strength is high enough to transform just the bulk to ferromagnetic state thereby making the segregation energy more negative. This study is important in understanding

the magnetic and thermal behavior of metal and alloys where the matrix and alloying element have different magnetic character. Furthermore, such an investigation can aid in potential application of magnetic field in various industrial processes.

7.2 Outlook

Several models have been proposed to explain the diffusion governing the growth of a phase during solid-state phase transformation. These models include paraequilibrium partitioning, local equilibrium partitioning, and negligible partitioning local equilibrium. While these models have had some success in predicting the diffusion of elements during partitioning, they often fail when the diffusing species have significantly different diffusivities, such as in the case of C and Mn partitioning. In such situations, C may achieve local equilibrium due to its high diffusivity, but the same cannot be said for substitutional elements like Ni and Mn.

In experiments, especially during low-temperature tempering (~450°C), it has been observed that Mn begins to diffuse but does not achieve local equilibrium, as noted in my experiments. This situation falls between the paraequilibrium and local equilibrium partitioning mechanisms.

To understand such a situation, a quasi-paraequilibrium model was proposed where substitutional elements like Ni and Mn are expected to exhibit partitioning behaviour. They do partition, but with limited diffusivity, and consequently, do not achieve local equilibrium. So far, I have only provided a theoretical explanation of the quasi-paraequilibrium model to explain my results. Proper computer-based modelling of these parameters is necessary to further comment on the diffusion process.

The superledges exhibited near-local equilibrium segregation values, but the exact location of Mn segregation is still unknown. Although it might appear that a certain specific set of planes should host the segregating species [126], numerous other studies have concluded that facet junctions host them [134]. Meanwhile one article reported that carbides segregate at the low index semi-coherent planes [215]. Under such circumstances, it is important to have a thorough understanding of the energetics of these superledges and the corresponding segregation of species in these crystallographic features. Since the observed superledges are never edge on with the beam direction, it becomes difficult to do compositional analysis as the inclination tends to smear out the preferential segregation behavior. The next step should be coupling APT study with machine learning for proper analysis of dataset and corresponding correlation with the embedded crystallographic information which usually goes unnoticed.

List of figures

List of Tables

References

[1] M. Gouné *et al.*, "Overview of the current issues in austenite to ferrite transformation and the role of migrating interfaces therein for low alloyed steels," *Materials Science and Engineering: R: Reports,* vol. 92, pp. 1-38, 2015.

[2] D. A. Porter and K. E. Easterling, *Phase transformations in metals and alloys (revised reprint)*. CRC press, 2009.

[3] H. K. D. H. Bhadeshia and R. W. K. Honeycombe, *Steels: microstructure and properties*. Butterworth-Heinemann, 2017.

[4] H. K. D. H. Bhadeshia and C. M. Wayman, "Phase Transformations," in *Physical Metallurgy*, 2014, pp. 1021-1072.

[5] M. Hillert, "Paraequilibrium and other restricted equilibria," *MRS Online Proceedings Library (OPL),* vol. 19, p. 295, 1982.

[6] J. Kirkaldy, "Theory of diffusional growth in solid-solid transformations," *Decomposition of Austenite by Diffusional Processes,* pp. 39-122, 1962.

[7] H. Chen, B. Appolaire, and S. van der Zwaag, "Application of cyclic partial phase transformations for identifying kinetic transitions during solid-state phase transformations: Experiments and modeling," *Acta Materialia,* vol. 59, no. 17, pp. 6751-6760, 2011.

[8] A. Van der Ven and L. Delaey, "Models for precipitate growth during the γ→ α+ γ transformation in Fe-C and Fe-C- M alloys," *Progress in materials science,* vol. 40, no. 3, pp. 181-264, 1996.

[9] Y. Ma *et al.*, "Phase boundary segregation-induced strengthening and discontinuous yielding in ultrafine-grained duplex medium-Mn steels," *Acta Materialia,* vol. 200, pp. 389-403, 2020, doi: 10.1016/j.actamat.2020.09.007.

[10] O. Dmitrieva *et al.*, "Chemical gradients across phase boundaries between martensite and austenite in steel studied by atom probe tomography and simulation," *Acta Materialia,* vol. 59, no. 1, pp. 364-374, 2011, doi: 10.1016/j.actamat.2010.09.042.

[11] J. W. Gibbs, "Thermodynamics," vol. 1, 1961.

[12] K. i. Shimizu and T. Kakeshita, "Effect of magnetic fields on martensitic transformations in ferrous alloys and steels," *ISIJ International,* vol. 29, no. 2, pp. 97-116, 1989.

[13] D. Nicholson *et al.*, "The effect of high magnetic field on phase stability in Fe-Ni," *Journal of Applied Physics,* vol. 95, no. 11, pp. 6580-6582, 2004.

[14] Y. Waseda and K. Suzuki, "Atomic distribution and magnetic moment in liquid iron by neutron diffraction," *東北大学研究所報告. A 集, 物理学・化学・冶金学= Science reports of the Research Institutes, Tohoku University. Ser. A, Physics, chemistry and metallurgy,* no. 22, pp. 181-181, 1970.

[15] Y.-Y. Chuang, Y. A. Chang, R. Schmid, and J.-C. Lin, "Magnetic contributions to the thermodynamic functions of alloys and the phase equilibria of Fe-Ni system below 1200 K," *Metallurgical Transactions A,* vol. 17, pp. 1361-1372, 1986.

[16] E. Fokina, L. Smirnov, and V. Sadovsky, "Effect of a magnetic field on the position of the martensite point in carbon steels," *FIZIKA METALLOV METALLOVEDENIE,* vol. 27, no. 4, pp. 756-757, 1969.

[17] J. W. Cahn, "Magnetic Aging of Spinodal Alloys," *Journal of Applied Physics,* vol. 34, no. 12, pp. 3581-3586, 1963, doi: 10.1063/1.1729261.

[18] Y. Zhang, N. Gey, C. He, X. Zhao, L. Zuo, and C. Esling, "High temperature tempering behaviors in a structural steel under high magnetic field," *Acta Materialia,* vol. 52, no. 12, pp. 3467-3474, 2004, doi: 10.1016/j.actamat.2004.03.044.

[19] G. H. Wu, T. P. Hou, K. M. Wu, and L. Chen, "Influence of high magnetic field on carbides and the dislocation density during tempering of high Chromium-containing steel," *Journal of Magnetism and Magnetic Materials,* vol. 479, pp. 43-49, 2019, doi: 10.1016/j.jmmm.2019.01.109.

[20] Y. Wu, Y. Lu, X. Zhao, and L. Zuo, "Effect of High Magnetic Field on Diffusion Behavior of Carbon in Pure Iron," *Advanced Materials Research,* vol. 194-196, pp. 67-70, 2011, doi: 10.4028/www.scientific.net/AMR.194-196.67.

[21] X. Zhang, Y. Zhang, M. Gong, C. Esling, X. Zhao, and L. Zuo, "Magnetic-field-induced microstructural features in a high carbon steel during diffusional phase transformation," *Journal of Magnetism and Magnetic Materials,* vol. 324, no. 24, pp. 4184-4188, 2012, doi: 10.1016/j.jmmm.2012.07.041.

[22] X. Zhang, Q. Zhao, Z. Cai, and J. Pan, "Effects of magnetic field on the residual stress and structural defects of Ti-6Al-4V," *Metals,* vol. 10, no. 1, p. 141, 2020.

[23] Y. Zhang and C. Esling, "The effect of a magnetic field on phase transformations in steels," in *Phase Transformations in Steels*, 2012, pp. 555-580.

[24] Z. W. Zhang, Y. Wu, and X. Zhao, "Effects of Magnetic Field Intensity on Carbon Diffusion in Pure Iron in Paramagnetic Ferrite Region," *Materials Science Forum,* vol. 879, pp. 2434-2438, 2016, doi: 10.4028/www.scientific.net/MSF.879.2434.

[25] I. R. Souza Filho, M. J. R. Sandim, R. Cohen, L. C. C. M. Nagamine, H. R. Z. Sandim, and D. Raabe, "Magnetic properties of a 17.6 Mn-TRIP steel: Study of strain-induced martensite formation, austenite reversion, and athermal α'-formation," *Journal of Magnetism and Magnetic Materials,* vol. 473, pp. 109-118, 2019, doi: 10.1016/j.jmmm.2018.10.034.

[26] I. Mirebeau *et al.*, "Magnetic and atomic short range order in $Fe_{1-x}Cr_x$ alloys," *Physical Review B,* vol. 100, no. 22, 2019, doi: 10.1103/PhysRevB.100.224406.

[27] X. J. Liu, Y. Lu, Y. M. Fang, and C. P. Wang, "Effects of external magnetic field on the diffusion coefficient and kinetics of phase transformation in pure Fe and Fe–C alloys," *Calphad,* vol. 35, no. 1, pp. 66-71, 2011/03/01/ 2011, doi: https://doi.org/10.1016/j.calphad.2010.12.004.

[28] X. J. Liu, Y. M. Fang, C. P. Wang, Y. Q. Ma, and D. L. Peng, "Effect of external magnetic field on thermodynamic properties and phase transitions in Fe-based alloys," *Journal of Alloys and Compounds,* vol. 459, no. 1-2, pp. 169-173, 2008, doi: 10.1016/j.jallcom.2007.04.289.

[29] W. Liu, D. R. Ou, H. H. Zhou, G. Y. Tang, and F. Wu, "Effect of a magnetic field on phase transformation of steel," *Journal of Materials Research,* vol. 16, no. 8, pp. 2280-2282, 2011, doi: 10.1557/jmr.2001.0313.

[30] J. F. Libsch, E. Both, G. W. Beckman, D. Warren, and R. J. Franklin, "Effect of annealing in a magnetic field upon iron-cobalt and iron-cobalt-nickel alloys prepared by powder metallurgy," *JOM,* vol. 2, pp. 287-296, 1950.

[31] Z. Li, T. Hou, G. Wu, K. Wu, and H. Lin, "Thermodynamic Analysis for the Magnetic-Field-Induced Precipitation Behaviours in Steels," *Metals,* vol. 9, no. 8, 2019, doi: 10.3390/met9080909.

[32] T. P. Hou *et al.*, "Magnetism and high magnetic-field-induced stability of alloy carbides in Fe-based materials," *Sci Rep,* vol. 8, no. 1, p. 3049, Feb 14 2018, doi: 10.1038/s41598-018-20910-3.

[33] S. Chen, R. Rana, A. Haldar, and R. K. Ray, "Current state of Fe-Mn-Al-C low density steels," *Progress in Materials Science,* vol. 89, pp. 345-391, 2017, doi: 10.1016/j.pmatsci.2017.05.002.

[34] R. A. Howell and D. C. Van Aken, "A literature review of age hardening Fe-Mn-Al-C alloys," 2009.

[35] H. Kim, D.-W. Suh, and N. J. Kim, "Fe–Al–Mn–C lightweight structural alloys: a review on the microstructures and mechanical properties," *Science and technology of advanced materials,* 2013.

[36] G. Frommeyer and U. Brüx, "Microstructures and mechanical properties of high-strength Fe-Mn-Al-C light-weight TRIPLEX steels," *Steel research international,* vol. 77, no. 9-10, pp. 627-633, 2006.

[37] I. Kalashnikov, A. Shalkevich, O. Acselrad, and L. Pereira, "Chemical composition optimization for austenitic steels of the Fe-Mn-Al-C system," *Journal of materials engineering and performance,* vol. 9, pp. 597-602, 2000.

[38] S. Chang, Y. Hsiau, and M. Jahn, "Tensile and fatigue properties of Fe-Mn-Al-C alloys," *Journal of materials science,* vol. 24, pp. 1117-1120, 1989.

[39] I. Kalashnikov, O. Acselrad, L. Pereira, T. Kalichak, and M. Khadyyev, "Behavior of Fe-Mn-Al-C steels during cyclic tests," *Journal of materials engineering and performance,* vol. 9, pp. 334-337, 2000.

[40] C. Kao and C. Wan, "Effect of temperature on the oxidation of Fe-7.5 A1-o. 65C alloy," *Journal of materials science,* vol. 23, pp. 1943-1947, 1988.

[41] Y. K. Lee and J. Han, "Current opinion in medium manganese steel," *Materials Science and Technology,* vol. 31, no. 7, pp. 843-856, 2014, doi: 10.1179/1743284714y.0000000722.

[42] B. Sun, H. Aydin, F. Fazeli, and S. Yue, "Microstructure Evolution of a Medium Manganese Steel During Thermomechanical Processing," *Metallurgical and Materials Transactions A,* vol. 47, no. 4, pp. 1782-1791, 2016, doi: 10.1007/s11661-016-3338-5.

[43] D. K. Matlock and J. G. Speer, "Third generation of AHSS: microstructure design concepts," in *Microstructure and Texture in Steels: and Other Materials*: Springer, 2009, pp. 185-205.

[44] A. Dumay, J.-P. Chateau, S. Allain, S. Migot, and O. Bouaziz, "Influence of addition elements on the stacking-fault energy and mechanical properties of an austenitic Fe–Mn–C steel," *Materials Science and Engineering: A,* vol. 483, pp. 184-187, 2008.

[45] W. D. Callister *et al.*, *Materials science and engineering: an introduction*. John wiley & sons New York, 2007.

[46] C. G. De Andres, F. Caballero, C. Capdevila, and L. Alvarez, "Application of dilatometric analysis to the study of solid–solid phase transformations in steels," *Materials Characterization,* vol. 48, no. 1, pp. 101-111, 2002.

[47] R. Dippenaar and R. W. K. Honeycombe, "The crystallography and nucleation of pearlite," *Proceedings of the Royal Society of London. A. Mathematical and Physical Sciences,* vol. 333, no. 1595, pp. 455-467, 1973.

[48] H. Aaronson, "The proeutectoid ferrite and the proeutectoid cementite reactions," *Decomposition of Austenite by Diffusional Process,* vol. 167, 1962.

[49] H. Bhadeshia, "The bainite transformation: unresolved issues," *Materials science and engineering: A,* vol. 273, pp. 58-66, 1999.

[50] A. Cottrell, *An introduction to metallurgy*. CRC Press, 2019.

[51] L. Fielding, "The bainite controversy," *Materials Science and Technology,* vol. 29, no. 4, pp. 383-399, 2013.

[52] Y. Zhang, C. Zhang, X. Yuan, D. Li, Y. Yin, and S. Li, "Microstructure Evolution and Orientation Relationship of Reverted Austenite in 13Cr Supermartensitic Stainless Steel During the Tempering Process," *Materials (Basel),* vol. 12, no. 4, Feb 15 2019, doi: 10.3390/ma12040589.

[53] D.-W. Suh, S.-J. Park, T.-H. Lee, C.-S. Oh, and S.-J. Kim, "Influence of Al on the microstructural evolution and mechanical behavior of low-carbon, manganese transformation-induced-plasticity steel," *Metallurgical and Materials Transactions A,* vol. 41, pp. 397-408, 2010.

[54] H. Aydin, "Effect of microstructure on static and dynamic mechanical properties of third generation advanced high strength steels," 2013.

[55] H. Huang, O. Matsumura, and T. Furukawa, "Retained austenite in low carbon, manganese steel after intercritical heat treatment," *Materials science and technology,* vol. 10, no. 7, pp. 621-626, 1994.

[56] Q. Han, Y. Zhang, and L. Wang, "Effect of annealing time on microstructural evolution and deformation characteristics in 10Mn1. 5Al TRIP steel," *Metallurgical and Materials Transactions A,* vol. 46, pp. 1917-1926, 2015.

[57] H. Farahani, W. Xu, and S. Van der Zwaag, "Prediction and validation of the austenite phase fraction upon intercritical annealing of medium Mn steels," *Metallurgical and Materials Transactions A,* vol. 46, pp. 4978-4985, 2015.

[58] B. He, H. Luo, and M. Huang, "Experimental investigation on a novel medium Mn steel combining transformation-induced plasticity and twinning-induced plasticity effects," *International Journal of Plasticity,* vol. 78, pp. 173-186, 2016.

[59] J. Han, S.-J. Lee, J.-G. Jung, and Y.-K. Lee, "The effects of the initial martensite microstructure on the microstructure and tensile properties of intercritically annealed Fe–9Mn–0.05 C steel," *Acta Materialia,* vol. 78, pp. 369-377, 2014.

[60] T. W. J. Kwok and D. Dye, "A review of the processing, microstructure and property relationships in medium Mn steels," *International Materials Reviews,* vol. 68, no. 8, pp. 1098-1134, 2023/11/01 2023, doi: 10.1080/09506608.2023.2199617.

[61] M. F. Buchely, D. Field, and D. C. Van Aken, "Analysis of hot-and cold-rolled loads in medium-Mn TRIP steels," *Metallurgical and Materials Transactions B,* vol. 50, pp. 1180-1192, 2019.

[62] S. Lee and B. C. De Cooman, "Tensile Behavior of Intercritically Annealed Ultra-Fine Grained 8% Mn Multi-Phase Steel," *steel research international,* vol. 86, no. 10, pp. 1170-1178, 2015.

[63] M. Haupt, A. Dutta, D. Ponge, S. Sandlöbes, M. Nellessen, and G. Hirt, "Influence of intercritical annealing on microstructure and mechanical properties of a medium manganese steel," *Procedia engineering,* vol. 207, pp. 1803-1808, 2017.

[64] Z. Zhao, J. Liang, A. Zhao, J. Liang, D. Tang, and Y. Gao, "Effects of the austenitizing temperature on the mechanical properties of cold-rolled medium-Mn steel system," *Journal of Alloys and Compounds,* vol. 691, pp. 51-59, 2017.

[65] E. J. Seo, L. Cho, and B. C. De Cooman, "Modified methodology for the quench temperature selection in quenching and partitioning (Q&P) processing of steels," *Metallurgical and Materials Transactions A,* vol. 47, pp. 3797-3802, 2016.

[66] E. J. Seo, L. Cho, and B. C. De Cooman, "Application of quenching and partitioning processing to medium Mn steel," *Metallurgical and Materials Transactions A,* vol. 46, pp. 27-31, 2015.

[67] B. C. De Cooman, S. J. Lee, S. Shin, E. J. Seo, and J. G. Speer, "Combined intercritical annealing and Q&P processing of medium Mn steel," *Metallurgical and Materials Transactions A,* vol. 48, pp. 39-45, 2017.

[68] T. Tsuchiyama, T. Inoue, J. Tobata, D. Akama, and S. Takaki, "Microstructure and mechanical properties of a medium manganese steel treated with interrupted quenching and intercritical annealing," *Scripta Materialia,* vol. 122, pp. 36-39, 2016.

[69] Y.-U. Heo, D. H. Kim, N. H. Heo, C. W. Hong, and S.-J. Kim, "Deformation behavior in medium Mn steel of nanometer-sized α'+ γ lamellar structure," *Metallurgical and Materials Transactions A,* vol. 47, pp. 6004-6016, 2016.

[70] S. Liu, Z. Xiong, H. Guo, C. Shang, and R. Misra, "The significance of multi-step partitioning: Processing-structure-property relationship in governing high strength-high ductility combination in medium-manganese steels," *Acta materialia,* vol. 124, pp. 159-172, 2017.

[71] H. Aaronson, W. Reynolds, and G. Purdy, "Coupled-solute drag effects on ferrite formation in Fe-CX systems," *Metallurgical and Materials Transactions A,* vol. 35, pp. 1187-1210, 2004.

[72] H. Kitahara, R. Ueji, N. Tsuji, and Y. Minamino, "Crystallographic features of lath martensite in low-carbon steel," *Acta materialia,* vol. 54, no. 5, pp. 1279-1288, 2006.

[73] D. B. Williams and C. B. Carter, "Transmission electron microscopy: a textbook for materials science," *Micron,* vol. 28, no. 1, pp. 75-75, 1997.

[74] H. Kitahara, R. Ueji, M. Ueda, N. Tsuji, and Y. Minamino, "Crystallographic analysis of plate martensite in Fe–28.5 at.% Ni by FE-SEM/EBSD," *Materials Characterization,* vol. 54, no. 4-5, pp. 378-386, 2005.

[75] A. King and T. Bell, "Morphology and crystallography of Widmanstätten proeutectoid ferrite," *Metal Science,* vol. 8, no. 1, pp. 253-260, 1974.

[76] A. King and T. Bell, "Crystallography of grain boundary proeutectoid ferrite," *Metallurgical Transactions A,* vol. 6, pp. 1419-1429, 1975.
[77] H. Shirazi, G. Miyamoto, S. Hossein Nedjad, T. Chiba, M. Nili Ahmadabadi, and T. Furuhara, "Microstructure evolution during austenite reversion in Fe-Ni martensitic alloys," *Acta Materialia,* vol. 144, pp. 269-280, 2018, doi: 10.1016/j.actamat.2017.10.068.
[78] P. Wang, W. Zheng, X. Yu, and Y. Wang, "Advantageous Implications of Reversed Austenite for the Tensile Properties of Super 13Cr Martensitic Stainless Steel," *Materials (Basel),* vol. 15, no. 21, Nov 1 2022, doi: 10.3390/ma15217697.
[79] E. C. Bain, "The nature of martensite," *trans. AIME,* vol. 70, p. 25, 1924.
[80] G. Kurdjumov, "Over the mechanisms of steel hardening," *Z. Phys.,* vol. 64, p. 325, 1930.
[81] G. Wassermann, "Influence of the α–γ transformation of an irreversible Ni steel onto crystal orientation and tensile strength," *Arch. Eisenhüttenwes,* vol. 126, p. 647, 1933.
[82] W. Pitsch, "Der Orientierungszusammenhang zwischen Zementit und Austenit," *Acta Metallurgica,* vol. 10, no. 9, pp. 897-900, 1962/09/01/ 1962, doi: https://doi.org/10.1016/0001-6160(62)90108-6.
[83] A. B. Greninger and A. R. Troiano, "Crystallography of austenite decomposition," *Trans. Aime,* vol. 140, pp. 307-336, 1940.
[84] W. Z. Zhang and G. C. Weatherly, "On the crystallography of precipitation," *Progress in Materials Science,* vol. 50, no. 2, pp. 181-292, 2005, doi: 10.1016/j.pmatsci.2004.04.002.
[85] G. Speich, V. Demarest, and R. Miller, "Formation of austenite during intercritical annealing of dual-phase steels," *Metallurgical and materials transactions A,* vol. 12, pp. 1419-1428, 1981.
[86] Q. Lai *et al.*, "Mechanism of austenite formation from spheroidized microstructure in an intermediate Fe-0.1 C-3.5 Mn steel," *Metallurgical and Materials Transactions A,* vol. 47, pp. 3375-3386, 2016.
[87] S. Lee and B. C. De Cooman, "On the selection of the optimal intercritical annealing temperature for medium Mn TRIP steel," *Metallurgical and Materials Transactions A,* vol. 44, pp. 5018-5024, 2013.
[88] N. Nakada, T. Tsuchiyama, S. Takaki, and N. Miyano, "Temperature dependence of austenite nucleation behavior from lath martensite," *ISIJ international,* vol. 51, no. 2, pp. 299-304, 2011.
[89] R. Wei, M. Enomoto, R. Hadian, H. Zurob, and G. Purdy, "Growth of austenite from as-quenched martensite during intercritical annealing in an Fe–0.1 C–3Mn–1.5 Si alloy," *Acta Materialia,* vol. 61, no. 2, pp. 697-707, 2013.
[90] C. Garcia and A. Deardo, "Formation of austenite in 1.5 pct Mn steels," *Metallurgical Transactions A,* vol. 12, pp. 521-530, 1981.
[91] X.-L. Cai, A. Garratt-Reed, and W. Owen, "The development of some dual-phase steel structures from different starting microstructures," *Metallurgical Transactions A,* vol. 16, pp. 543-557, 1985.
[92] J. Ågren, "Computer simulations of the austenite/ferrite diffusional transformations in low alloyed steels," *Acta Metallurgica,* vol. 30, no. 4, pp. 841-851, 1982.
[93] B. De Cooman, "Graduate Institute of Ferrous Technology, POSTECH, Pohang, South Korea," *Automotive Steels: Design, Metallurgy, Processing and Applications,* p. 317, 2016.
[94] M. Gouné, P. Maugis, and J. Drillet, "A criterion for the change from fast to slow regime of cementite dissolution in Fe–C–Mn steels," *Journal of Materials Science & Technology,* vol. 28, no. 8, pp. 728-736, 2012.
[95] Q. Lai, "Microstructure optimization of ferrite-martensite steels with 3.5 wt% Mn: from phase transformation to micromechanics," Université de Grenoble, 2014.
[96] N. Fonstein, *Advanced high strength sheet steels*. Springer, 2015.
[97] J. Christian, *The theory of transformations in metals and alloys*. Newnes, 2002.

[98] C. Zener, "Theory of growth of spherical precipitates from solid solution," *Journal of applied physics,* vol. 20, no. 10, pp. 950-953, 1949.
[99] M. Hillert and J. Ågren, "On the definitions of paraequilibrium and orthoequilibrium," *Scripta Materialia,* vol. 50, no. 5, pp. 697-699, 2004.
[100] D. Coates, "Diffusion controlled precipitate growth in ternary systems: II," *Metallurgical Transactions,* vol. 4, pp. 1077-1086, 1973.
[101] G. Purdy, D. Weichert, and J. Kirkaldy, "Growth of proeutectoid ferrite in ternary iron-carbon-manganese austenites," *Transactions of the Metallurgical Society of AIME,* vol. 230, no. 5, pp. 1025-&, 1964.
[102] C. Qiu, "The'Solute-Drag'Effect on Migrating Interfaces During Solid-state Phase Transformations," Monash University, 2013.
[103] G. Miyamoto and T. Furuhara, "Interaction of alloying elements with migrating ferrite/austenite interface," *ISIJ International,* vol. 60, no. 12, pp. 2942-2953, 2020.
[104] G. Miyamoto, K. Yokoyama, and T. Furuhara, "Quantitative analysis of Mo solute drag effect on ferrite and bainite transformations in Fe-0.4 C-0.5 Mo alloy," *Acta Materialia,* vol. 177, pp. 187-197, 2019.
[105] H. Dong *et al.*, "Analysis of the interaction between moving α/γ interfaces and interphase precipitated carbides during cyclic phase transformations in a Nb-containing Fe-C-Mn alloy," *Acta Materialia,* vol. 158, pp. 167-179, 2018, doi: 10.1016/j.actamat.2018.07.052.
[106] H. Dong *et al.*, "Unraveling the effects of Nb interface segregation on ferrite transformation kinetics in low carbon steels," *Acta Materialia,* vol. 215, 2021, doi: 10.1016/j.actamat.2021.117081.
[107] B. Sun *et al.*, "Revealing fracture mechanisms of medium manganese steels with and without delta-ferrite," *Acta Materialia,* vol. 164, pp. 683-696, 2019, doi: 10.1016/j.actamat.2018.11.029.
[108] H. Aaronson and H. Domian, "Partition of alloying elements between austenite and proeutectoid ferrite or bainite," *AIME MET SOC TRANS,* vol. 236, no. 5, pp. 781-796, 1966.
[109] J. Bradley and H. Aaronson, "Growth kinetics of grain boundary ferrite allotriomorphs in Fe-CX alloys," *Metallurgical transactions A,* vol. 12, pp. 1729-1741, 1981.
[110] G. Miyamoto, K. Yokoyama, and T. Furuhara, "Quantitative analysis of Mo solute drag effect on ferrite and bainite transformations in Fe-0.4C-0.5Mo alloy," *Acta Materialia,* vol. 177, pp. 187-197, 2019/09/15/ 2019, doi: https://doi.org/10.1016/j.actamat.2019.07.040.
[111] W. Reynolds, S. Liu, F. Li, S. Hartfield, and H. Aaronson, "An investigation of the generality of incomplete transformation to bainite in Fe-CX alloys," *Metallurgical Transactions A,* vol. 21, pp. 1479-1491, 1990.
[112] H. Goldenstein and H. I. Aaronson, "Overall reaction kinetics and morphology of austenite decomposition between the upper nose and the M s of a hypoeutectoid Fe-C-Cr alloy," *Metallurgical Transactions A,* vol. 21, pp. 1465-1478, 1990.
[113] K. Aust and u. J. Rutter, "Grain boundary migration in high-purity lead and dilute lead-tin alloys," *Transactions of the American Institute of Mining and Metallurgical Engineers,* vol. 215, no. 1, pp. 119-127, 1959.
[114] J. W. Cahn, "The impurity-drag effect in grain boundary motion," *Acta metallurgica,* vol. 10, no. 9, pp. 789-798, 1962.
[115] G. Purdy and Y. Brechet, "A solute drag treatment of the effects of alloying elements on the rate of the proeutectoid ferrite transformation in steels," *Acta metallurgica et materialia,* vol. 43, no. 10, pp. 3763-3774, 1995.
[116] M. Enomoto, "Influence of solute drag on the growth of proeutectoid ferrite in Fe–C–Mn alloy," *Acta materialia,* vol. 47, no. 13, pp. 3533-3540, 1999.
[117] D. Raabe *et al.*, "Segregation engineering enables nanoscale martensite to austenite phase transformation at grain boundaries: A pathway to ductile martensite," *Acta Materialia,* vol. 61, no. 16, pp. 6132-6152, 2013, doi: 10.1016/j.actamat.2013.06.055.

[118] A. Kwiatkowski da Silva *et al.*, "Confined chemical and structural states at dislocations in Fe-9wt%Mn steels: A correlative TEM-atom probe study combined with multiscale modelling," *Acta Materialia,* vol. 124, pp. 305-315, 2017, doi: 10.1016/j.actamat.2016.11.013.

[119] S. Araki, K. Mashima, T. Masumura, T. Tsuchiyama, S. Takaki, and T. Ohmura, "Effect of grain boundary segregation of carbon on critical grain boundary strength of ferritic steel," *Scripta Materialia,* vol. 169, pp. 38-41, 2019, doi: 10.1016/j.scriptamat.2019.05.001.

[120] P. R. Cantwell *et al.*, "Grain Boundary Complexion Transitions," *Annual Review of Materials Research,* vol. 50, no. 1, pp. 465-492, 2020, doi: 10.1146/annurev-matsci-081619-114055.

[121] C. E. Carlton and P. J. Ferreira, "What is behind the inverse Hall–Petch effect in nanocrystalline materials?," *Acta Materialia,* vol. 55, no. 11, pp. 3749-3756, 2007, doi: 10.1016/j.actamat.2007.02.021.

[122] T. Frolov, M. Asta, and Y. Mishin, "Segregation-induced phase transformations in grain boundaries," *Physical Review B,* vol. 92, no. 2, 2015, doi: 10.1103/PhysRevB.92.020103.

[123] A. Ahmadian *et al.*, "Interstitial Segregation has the Potential to Mitigate Liquid Metal Embrittlement in Iron," *Adv Mater,* vol. 35, no. 28, p. e2211796, Jul 2023, doi: 10.1002/adma.202211796.

[124] A. Ahmadian *et al.*, "Aluminum depletion induced by co-segregation of carbon and boron in a bcc-iron grain boundary," *Nat Commun,* vol. 12, no. 1, p. 6008, Oct 14 2021, doi: 10.1038/s41467-021-26197-9.

[125] C. M. Barr *et al.*, "Exploring radiation induced segregation mechanisms at grain boundaries in equiatomic CoCrFeNiMn high entropy alloy under heavy ion irradiation," *Scripta Materialia,* vol. 156, pp. 80-84, 2018, doi: 10.1016/j.scriptamat.2018.06.041.

[126] V. Devulapalli, M. Hans, P. T. Sukumar, J. M. Schneider, G. Dehm, and C. H. Liebscher, "Microstructure, grain boundary evolution and anisotropic Fe segregation in (0001) textured Ti thin films," *Acta Materialia,* vol. 238, p. 118180, 2022/10/01/ 2022, doi: https://doi.org/10.1016/j.actamat.2022.118180.

[127] S. J. Dillon, M. Tang, W. C. Carter, and M. P. Harmer, "Complexion: A new concept for kinetic engineering in materials science," *Acta Materialia,* vol. 55, no. 18, pp. 6208-6218, 2007, doi: 10.1016/j.actamat.2007.07.029.

[128] M. Herbig *et al.*, "Grain boundary segregation in Fe–Mn–C twinning-induced plasticity steels studied by correlative electron backscatter diffraction and atom probe tomography," *Acta Materialia,* vol. 83, pp. 37-47, 2015, doi: 10.1016/j.actamat.2014.09.041.

[129] M. Herbig, D. Raabe, Y. J. Li, P. Choi, S. Zaefferer, and S. Goto, "Atomic-scale quantification of grain boundary segregation in nanocrystalline material," *Phys Rev Lett,* vol. 112, no. 12, p. 126103, Mar 28 2014, doi: 10.1103/PhysRevLett.112.126103.

[130] L. Huber, R. Hadian, B. Grabowski, and J. Neugebauer, "A machine learning approach to model solute grain boundary segregation," *npj Computational Materials,* vol. 4, no. 1, 2018, doi: 10.1038/s41524-018-0122-7.

[131] M. Kuzmina, D. Ponge, and D. Raabe, "Grain boundary segregation engineering and austenite reversion turn embrittlement into toughness: Example of a 9 wt.% medium Mn steel," *Acta Materialia,* vol. 86, pp. 182-192, 2015, doi: 10.1016/j.actamat.2014.12.021.

[132] A. Kwiatkowski da Silva, R. D. Kamachali, D. Ponge, B. Gault, J. Neugebauer, and D. Raabe, "Thermodynamics of grain boundary segregation, interfacial spinodal and their relevance for nucleation during solid-solid phase transitions," *Acta Materialia,* vol. 168, pp. 109-120, 2019, doi: 10.1016/j.actamat.2019.02.005.

[133] P. Lajcek, *Grain boundary segregation in metals*. Springer Science and Business Media, 2010.

[134] C. H. Liebscher *et al.*, "Strain-Induced Asymmetric Line Segregation at Faceted Si Grain Boundaries," *Physical Review Letters,* vol. 121, no. 1, p. 015702, 07/06/ 2018, doi: 10.1103/PhysRevLett.121.015702.

[135] N. Ma, S. A. Dregia, and Y. Wang, "Solute segregation transition and drag force on grain boundaries," *Acta Materialia,* vol. 51, no. 13, pp. 3687-3700, 2003, doi: 10.1016/s1359-6454(03)00184-8.

[136] J. R. Mianroodi, P. Shanthraj, A. K. da Silva, B. Svendsen, and D. Raabe, "Combined modeling and experimental characterization of Mn segregation and spinodal decomposition along dislocation lines in Fe–Mn alloys," *Acta Materialia,* vol. 251, p. 118873, 2023.

[137] B. Mintz, H. Ke, and G. D. W. Smith, "Grain size strengtherning in steel and its relationship to grain boundary segregation of carbon," *Material Science and Technology,* vol. 8, no. 6, pp. 537-540, 1992.

[138] *Microstructural Design of Advanced Engineering Materials* Wiley VCH Verlag GmbH & Co. , 2013.

[139] D. Raabe *et al.*, "Grain boundary segregation engineering in metallic alloys: A pathway to the design of interfaces," *Current Opinion in Solid State and Materials Science,* vol. 18, no. 4, pp. 253-261, 2014, doi: 10.1016/j.cossms.2014.06.002.

[140] S. Takaki, D. Akama, N. Nakada, and T. Tsuchiyama, "Effect of Grain Boundary Segregation of Interstitial Elements on Hall–Petch Coefficient in Steels," *Materials Transactions,* vol. 55, no. 1, pp. 28-34, 2014, doi: 10.2320/matertrans.MA201314.

[141] K. Takeda, N. Nakada, T. Tscuchiyama, and S. Takaki, "Effect of interstitial elements on hall-petch coefficient of ferritic iron," *ISIJ International,* vol. 48, no. 8, pp. 1122-1125, 2008.

[142] J. M. Howe, *Interfaces in Materials*. New York: Wiley, 1997.

[143] C. C. Tasan *et al.*, "Integrated experimental–simulation analysis of stress and strain partitioning in multiphase alloys," *Acta Materialia,* vol. 81, pp. 386-400, 2014.

[144] Z. H. Cong, N. Jia, X. Sun, and Y. Ren, "Stress and strain paritioning of ferrite and martensite during deformation," *Metallurgical and Materials Transactions A,* vol. 40, no. 6, pp. 1383-1387, 2009.

[145] N. Ishikawa *et al.*, "Microscopic deformation and strain hardening analysis of ferrite–bainite dual-phase steels using micro-grid method," *Acta Materialia,* vol. 97, pp. 257-268, 2015.

[146] M. Enomoto, "Structure, energy and migration of phase boundaries in steels," in *Phase Transformations in Steels*, 2012, pp. 157-183.

[147] G. Olson and M. Cohen, "Interphase-boundary dislocations and the concept of coherency," *Acta Metallurgica,* vol. 27, no. 12, pp. 1907-1918, 1979.

[148] D. Wolf and S. Yip, *Materials interfaces: atomic-level structure and properties*. London, 1992.

[149] K. C. Russell, H. I. Aaronson, and M. S. o. A. H. T. Committee, *Precipitation Processes in Solids: Proceedings of a Symposium Sponsored by the TMS-AIME Heat Treatment Committee at the 1976 TMS Fall Meeting at Niagara Falls, New York, September 20, 21*. Metallurgical Society of AIME, 1978.

[150] J. Watson and P. McDougall, "The crystallography of Widmanstätten ferrite," *Acta metallurgica,* vol. 21, no. 7, pp. 961-973, 1973.

[151] J. Rigsbee and H. Aaronson, "The interfacial structure of the broad faces of ferrite plates," *Acta Metallurgica,* vol. 27, no. 3, pp. 365-376, 1979.

[152] Y. Liu, H. Aaronson, K. Kinsman, and M. Hall, "The habit plane of Widmanstätten ferrite sideplates," *Metallurgical Transactions,* vol. 3, pp. 1318-1320, 1972.

[153] J. Young, "Crystallographic studies of meteoric iron," *Philosophical Transactions of the Royal Society of London. Series A, Mathematical and Physical Sciences,* vol. 238, no. 794, pp. 393-421, 1939.

[154] U. Dahmen, P. Ferguson, and K. Westmacott, "Invariant line strain and needle-precipitate growth directions in Fe-Cu," *Acta Metallurgica,* vol. 32, no. 5, pp. 803-810, 1984.

[155] C. Luo and G. Weatherly, "The invariant line and precipitation in a Ni-45 wt% Cr alloy," *Acta metallurgica,* vol. 35, no. 8, pp. 1963-1972, 1987.

[156] J. Chen, D. Farkas, and W. Reynolds Jr, "Atomistic simulations of fcc: bcc interphase boundary structures and energies," *PTM'94, Solid-to-Solid Phase Transformations,* pp. 1097-1102, 1994.

[157] J. Chen, D. Farkas, and W. Reynolds Jr, "Atomistic simulation of an fcc/bcc interface in Ni・Cr alloys," *Acta materialia,* vol. 45, no. 11, pp. 4415-4421, 1997.

[158] T. Nagano and M. Enomoto, "Calculation of the interfacial energies between α and γ iron and equilibrium particle shape," *Metallurgical and Materials Transactions A,* vol. 37, pp. 929-937, 2006.

[159] X. Zhou *et al.*, "Revealing in-plane grain boundary composition features through machine learning from atom probe tomography data," *Acta Materialia,* vol. 226, 2022, doi: 10.1016/j.actamat.2022.117633.

[160] X. F. Gu and W. Z. Zhang, "An Energetic Study on the Preference of the Habit Plane in Fcc/bcc System," *Solid State Phenomena,* vol. 172-174, pp. 260-266, 2011, doi: 10.4028/www.scientific.net/SSP.172-174.260.

[161] Z. Yang and R. Johnson, "An EAM simulation of the alpha-gamma iron interface," *Modelling and Simulation in Materials Science and Engineering,* vol. 1, no. 5, p. 707, 1993.

[162] Y.-J. Zhang, G. Miyamoto, K. Shinbo, and T. Furuhara, "Effects of α/γ orientation relationship on VC interphase precipitation in low-carbon steels," *Scripta Materialia,* vol. 69, no. 1, pp. 17-20, 2013.

[163] M. Hillert, Swedish Institute of Metal Research, 1960, vol. 1.

[164] Y. J. Zhang, G. Miyamoto, K. Shinbo, and T. Furuhara, "Quantitative measurements of phase equilibria at migrating α/γ interface and dispersion of VC interphase precipitates: Evaluation of driving force for interphase precipitation," *Acta Materialia,* vol. 128, pp. 166-175, 2017, doi: 10.1016/j.actamat.2017.02.020.

[165] P. Hohenberg and W. Kohn, "Inhomogeneous Electron Gas," *Physical Review,* vol. 136, no. 3B, pp. B864-B871, 1964, doi: 10.1103/PhysRev.136.B864.

[166] O. Hegde *et al.*, "Atomic relaxation around defects in magnetically disordered materials computed by atomic spin constraints within an efficient Lagrange formalism," *Physical Review B,* vol. 102, no. 14, 2020, doi: 10.1103/PhysRevB.102.144101.

[167] F. Körmann, A. Dick, B. Grabowski, T. Hickel, and J. Neugebauer, "Atomic forces at finite magnetic temperatures: Phonons in paramagnetic iron," *Physical Review B,* vol. 85, no. 12, 2012, doi: 10.1103/PhysRevB.85.125104.

[168] S. Boeck, C. Freysoldt, A. Dick, L. Ismer, and J. Neugebauer, "The object-oriented DFT program library S/PHI/nX," *Computer Physics Communications,* vol. 182, no. 3, pp. 543-554, 2011, doi: 10.1016/j.cpc.2010.09.016.

[169] R. S. Varanasi, M. Lipińska-Chwałek, J. Mayer, B. Gault, and D. Ponge, "Mechanisms of austenite growth during intercritical annealing in medium manganese steels," *Scripta Materialia,* vol. 206, 2022, doi: 10.1016/j.scriptamat.2021.114228.

[170] L. Morsdorf, A. Kashiwar, C. Kübel, and C. C. Tasan, "Carbon segregation and cementite precipitation at grain boundaries in quenched and tempered lath martensite," *Materials Science and Engineering: A,* vol. 862, 2023, doi: 10.1016/j.msea.2022.144369.

[171] S. Y. Shin *et al.*, "Correlation of microstructure and cracking phenomenon occurring during hot rolling of lightweight steel plates," *Metallurgical and Materials Transactions A,* vol. 41, pp. 138-148, 2010.

[172] S. Y. Han, S. Y. Shin, S. Lee, N. J. Kim, J.-H. Kwak, and K.-G. Chin, "Effect of carbon content on cracking phenomenon occurring during cold rolling of three light-weight steel plates," *Metallurgical and Materials Transactions A,* vol. 42, pp. 138-146, 2011.

[173] B. P. J. Sandvik, "The Bainite reaction in Fe-Si-C Alloys: The primary stage," *Metallurgical Transactions A,* Article vol. 13, no. 5, pp. 777-787, 1982, doi: 10.1007/BF02642391.

[174] C. Servant and G. Cizeron, "contribution to the crystallography of the bainite transformation in a high strength low alloy steel 40 NSCD 7-7-3 (AISI 300M)," *Acta Metallurgica,* Article vol. 37, no. 2, pp. 465-476, 1989, doi: 10.1016/0001-6160(89)90230-7.

[175] S. Hoekstra, H. Van Der Lelie, and C. Verbraak, "A general method of habit plane determination in bainitic steels—II. Habit plane determination of the bainite," *Acta Metallurgica,* vol. 26, no. 10, pp. 1517-1527, 1978.

[176] H. Bhadeshia, "The lower bainite transformation and the significance of carbide precipitation," *Acta metallurgica,* vol. 28, no. 8, pp. 1103-1114, 1980.

[177] T. Massalski, "Massive transformations revisited," *Metallurgical and Materials Transactions A,* vol. 33, pp. 2277-2283, 2002.

[178] T. B. Massalski, "Comments concerning some features of phase diagrams and phase transformations," *Materials transactions,* vol. 51, no. 4, pp. 583-596, 2010.

[179] E. A. Wilson, "The Gamma to Alpha Transformation in Low Carbon Irons," *ISIJ International,* vol. 34, no. 8, pp. 615-630, 1994, doi: 10.2355/isijinternational.34.615.

[180] T. Moritani, N. Miyajima, T. Furuhara, and T. Maki, "Comparison of interphase boundary structure between bainite and martensite in steel," *Scripta materialia,* vol. 47, no. 3, pp. 193-199, 2002.

[181] F. Maresca and W. A. Curtin, "The austenite/lath martensite interface in steels: Structure, athermal motion, and in-situ transformation strain revealed by simulation and theory," *Acta Materialia,* vol. 134, pp. 302-323, 2017, doi: 10.1016/j.actamat.2017.05.044.

[182] Y. Toji, H. Matsuda, M. Herbig, P. P. Choi, and D. Raabe, "Atomic-scale analysis of carbon partitioning between martensite and austenite by atom probe tomography and correlative transmission electron microscopy " *Acta Materialia,* vol. 65, pp. 215-228, 2014.

[183] B. Sun *et al.*, "Macroscopic to nanoscopic in situ investigation on yielding mechanisms in ultrafine grained medium Mn steels: Role of the austenite-ferrite interface," *Acta Materialia,* vol. 178, pp. 10-25, 2019, doi: 10.1016/j.actamat.2019.07.043.

[184] H. K. D. H. Bhadeshia, "Prevention of hydrogen embrittlement in steels," *ISIJ International,* vol. 56, no. 1, pp. 24-36, 2016.

[185] J.-M. Jang, S.-J. Kim, N. H. Kang, K.-M. Cho, and D.-W. Suh, "Effects of annealing conditions on microstructure and mechanical properties of low carbon, manganese transformation-induced plasticity steel," *Metals and Materials International,* vol. 15, no. 6, pp. 909-916, 2009, doi: 10.1007/s12540-009-0909-7.

[186] R. Cao, J. Liang, F. Li, C. Li, and Z. Zhao, "Intercritical Annealing Processing and a New Type of Quenching and Partitioning Processing, Actualized by Combining Intercritical Quenching and Tempering, for Medium Manganese Lightweight Steel," *steel research international,* vol. 91, no. 1, 2019, doi: 10.1002/srin.201900335.

[187] H. Luo, J. Shi, C. Wang, W. Cao, X. Sun, and H. Dong, "Experimental and numerical analysis on formation of stable austenite during the intercritical annealing of 5Mn steel," *Acta Materialia,* vol. 59, no. 10, pp. 4002-4014, 2011, doi: 10.1016/j.actamat.2011.03.025.

[188] J. Shi, J. Hu, C. Wang, C. Y. Wang, H. Dong, and W. Q. Cao, "Ultrafine Grained Duplex Structure Developed by ART-annealing in Cold Rolled Medium-Mn Steels," *Journal of Iron and Steel Research, International,* vol. 21, no. 2, pp. 208-214, 2014.

[189] L. Koch *et al.*, "Local segregation versus irradiation effects in high-entropy alloys: Steady-state conditions in a driven system," *Journal of Applied Physics,* vol. 122, no. 10, 2017, doi: 10.1063/1.4990950.

[190] E. Pereloma, H. Beladi, L. Zhang, and I. Timokhina, "Understanding the Behavior of Advanced High-Strength Steels Using Atom Probe Tomography," *Metallurgical and Materials Transactions A,* vol. 43, no. 11, pp. 3958-3971, 2011, doi: 10.1007/s11661-011-0782-0.

[191] A. H. Cottrell and B. A. Bilby, "Dislocation Theory of Yielding and Strain ageing of Iron," *Proceedings of the Physical Society A,* pp. 49-62, 1949.

[192] J. P. Hirth and R. W. Balluffi, "On Grain Boundary Dislocations and Ledges," *Acta Metallurgica,* vol. 21, pp. 929-942, 1973.
[193] M. A. Tschopp and D. L. McDowell, "Grain boundary dislocation sources in nanocrystalline copper," *Scripta Materialia,* vol. 58, no. 4, pp. 299-302, 2008, doi: 10.1016/j.scriptamat.2007.10.010.
[194] G. J. Shiflet and J. H. Van der Merve, "The role of structural ledges as misfit compensating defects; fcc-bcc interphase boundaries," *Metallurgical and Materials Transactions A,* vol. 25, pp. 1895-1903, 1994.
[195] M. G. Hall, H. I. Aaranson, and K. R. Kinsma, "The structure of nearly coherent fcc-bcc boundaries in CU CR Alloy," *Surface Science,* vol. 31, pp. 257-274, 1972.
[196] V. Borovikov, M. I. Mendelev, and A. H. King, "Solute effects on interfacial dislocation emission in nanomaterials: Nucleation site competition and neutralization," *Scripta Materialia,* vol. 154, pp. 12-15, 2018, doi: 10.1016/j.scriptamat.2018.05.011.
[197] V. Borovikov, M. I. Mendelev, and A. H. King, "Effects of solutes on dislocation nucleation from grain boundaries," *International Journal of Plasticity,* vol. 90, pp. 146-155, 2017, doi: 10.1016/j.ijplas.2016.12.009.
[198] A. Kwiatkowski da Silva *et al.*, "Phase nucleation through confined spinodal fluctuations at crystal defects evidenced in Fe-Mn alloys," *Nature Communications,* vol. 9, no. 1, p. 1137, 2018/03/19 2018, doi: 10.1038/s41467-018-03591-4.
[199] J. T. Benzing *et al.*, "Multi-scale characterization of austenite reversion and martensite recovery in a cold-rolled medium-Mn steel," *Acta Materialia,* vol. 166, pp. 512-530, 2019, doi: 10.1016/j.actamat.2019.01.003.
[200] H. Xie *et al.*, "Nonsymmetrical Segregation of Solutes in Periodic Misfit Dislocations Separated Tilt Grain Boundaries," *Nano Lett,* vol. 21, no. 7, pp. 2870-2875, Apr 14 2021, doi: 10.1021/acs.nanolett.0c05008.
[201] S. K. Makineni *et al.*, "On the diffusive phase transformation mechanism assisted by extended dislocations during creep of a single crystal CoNi-based superalloy," *Acta Materialia,* vol. 155, pp. 362-371, 2018/08/15/ 2018, doi: https://doi.org/10.1016/j.actamat.2018.05.074.
[202] J. Christian, "Crystallographic theories, interface structures, and transformation mechanisms," *Metallurgical and Materials Transactions A,* vol. 25, pp. 1821-1839, 1994.
[203] P. Howell, P. Southwick, and R. Honeycombe, "The austenite/ferrite interface in a duplex alloy steel: structure and associated diffraction effects," *Journal of Microscopy,* vol. 116, no. 1, pp. 151-158, 1979.
[204] B. Sandvik and C. Wayman, "Characteristics of lath martensite: Part II. The martensite-austenite interface," *Metallurgical Transactions A,* vol. 14, pp. 823-834, 1983.
[205] B. Sandvik and C. Wayman, "The substructure of (252) f martensite formed in an Fe-8Cr-1 C alloy," *Metallurgical transactions A,* vol. 14, pp. 2455-2468, 1983.
[206] H. Zhao *et al.*, "Interplay of Chemistry and Faceting at Grain Boundaries in a Model Al Alloy," *Physical Review Letters,* vol. 124, no. 10, p. 106102, 03/09/ 2020, doi: 10.1103/PhysRevLett.124.106102.
[207] S.-P. Tsai, S. K. Makineni, B. Gault, K. Kawano-Miyata, A. Taniyama, and S. Zaefferer, "Precipitation formation on∑ 5 and∑ 7 grain boundaries in 316L stainless steel and their roles on intergranular corrosion," *Acta Materialia,* vol. 210, p. 116822, 2021.
[208] N. J. Peter *et al.*, "Segregation-Induced Nanofaceting Transition at an Asymmetric Tilt Grain Boundary in Copper," *Physical Review Letters,* vol. 121, no. 25, p. 255502, 12/20/ 2018, doi: 10.1103/PhysRevLett.121.255502.
[209] K. Verbeken, L. Barbé, and D. Raabe, "Evaluation of the crystallographic orientation relationships between FCC and BCC phases in TRIP steels," *ISIJ international,* vol. 49, no. 10, pp. 1601-1609, 2009.

[210] W.-Z. Zhang and G. Weatherly, "On the crystallography of precipitation," *Progress in Materials Science,* vol. 50, no. 2, pp. 181-292, 2005.

[211] K. Ogawa and S. Kajiwara, "High-resolution electron microscopy study of ledge structures and transition lattices at the austenite–martensite interface in Fe-based alloys," *Philosophical Magazine,* vol. 84, no. 27, pp. 2919-2947, 2004.

[212] K. Kinsman, E. Eichen, and H. Aaronson, "Thickening kinetics of proeutectoid ferrite plates in Fe-C alloys," *Metallurgical Transactions A,* vol. 6, pp. 303-317, 1975.

[213] H. Dong *et al.*, "Heterogeneous segregation behavior of Nb at the stepped migrating interface during phase transformation," *Scripta Materialia,* vol. 222, p. 115038, 2023/01/01/ 2023, doi: https://doi.org/10.1016/j.scriptamat.2022.115038.

[214] J. Van der Merwe and G. Shiflet, "The role of structural ledges at phase boundaries—III. FCC-BCC interfaces in Kurdjumov-Sachs orientation," *Acta metallurgica et materialia,* vol. 42, no. 4, pp. 1199-1205, 1994.

[215] R. A. Ricks and P. R. Howell, "The formation of discrete precipitate dispersions on mobile interphase boundaries in iron-base alloys," *Acta Metallurgica,* vol. 31, no. 6, pp. 853-861, 1983/06/01/ 1983, doi: https://doi.org/10.1016/0001-6160(83)90113-X.

[216] J. Nutter, "Direct TEM Observation of the Movement of the Austenite-Ferrite Interface in Steels," University of Sheffield, 2018.

[217] H. Bhadeshia, "Some difficulties in the theory of diffusion-controlled growth in substitutionally alloyed steels," *Current Opinion in Solid State and Materials Science,* vol. 20, no. 6, pp. 396-400, 2016.

[218] H. S. Zurob, C. Hutchinson, A. Béché, G. R. Purdy, and Y. Bréchet, "A transition from local equilibrium to paraequilibrium kinetics for ferrite growth in Fe–C–Mn: A possible role of interfacial segregation," *Acta Materialia,* vol. 56, no. 10, pp. 2203-2211, 2008.

[219] J. W. Gibbs, *The Collected Works of J. Willard Gibbs: pt. 1. Elementary principles in statistical mechanics.-pt. 2. Dynamics. Vector analysis and multiple algebra. Electromagnetic theory of light, etc*. Yale University Press, 1948.

[220] D. McLean, "Grain boundaries in metals," 1957.

[221] I. Langmuir, "The adsorption of gases on plane surfaces of glass, mica and platinum," *Journal of the American Chemical society,* vol. 40, no. 9, pp. 1361-1403, 1918.

[222] D. Raabe *et al.*, "Interface Segregation in Advanced Steels Studied at the Atomic Scale," in *Microstructural Design of Advanced Engineering Materials*, 2013, pp. 267-298.

[223] V. I. Alshits, E. V. Darinskaya, M. V. Koldaeva, and E. A. Petrzhik, "Chapter 86 - Magnetoplastic Effect in Nonmagnetic Crystals," in *Dislocations in Solids*, vol. 14, J. P. Hirth Ed.: Elsevier, 2008, pp. 333-437.

[224] S. Asai, "Recent development and prospect of electromagnetic processing of materials," *Science and Technology of Advanced Materials,* vol. 1, no. 4, pp. 191-200, 2000.

[225] Y. I. Golovin, "Magnetoplastic effects in solids," *Physics of the solid state,* vol. 46, pp. 789-824, 2004.

[226] J. T. Lenkkeri and J. Levoska, "Effects of magnetic and structural changes on elastic moduli of iron-manganese alloys," *Philosophical Magazine A,* vol. 48, no. 5, pp. 749-758, 2006, doi: 10.1080/01418618308236541.

[227] P. E. Goins, H. A. Murdoch, E. Hernández-Rivera, and M. A. Tschopp, "Effect of magnetic fields on microstructure evolution," *Computational materials science,* vol. 150, pp. 464-474, 2018.

[228] H. D. Joo, S. U. Kim, N. S. Shin, and Y. M. Koo, "An effect of high magnetic field on phase transformation in Fe–C system," *Materials Letters,* vol. 43, no. 5-6, pp. 225-229, 2000, doi: 10.1016/s0167-577x(99)00263-3.

[229] T. Watanabe, S. Tsurekawa, X. Zhao, and L. Zuo, "Grain boundary engineering by magnetic field application," *Scripta Materialia,* vol. 54, no. 6, pp. 969-975, 2006.

[230] T. Watanabe, Y. Suzuki, S. Tanii, and H. Oikawa, "The effects of magnetic annealing on recrystallization and grain-boundary character distribution (GBCD) in iron–cobalt alloy polycrystals," *Philosophical magazine letters,* vol. 62, no. 1, pp. 9-17, 1990.

[231] L. Zuo, T. Watanabe, and C. Esling, "A Theoretical Approach to Grain Boundary Character Distribution (GBCD) in Textured Polyerystalline Materials/Eine theoretische Näherung zur Korngrenzencharakter-Verteilungsfunktion in polykristallinen texturierten Werkstoffen: Dedicated to Professor Dr. rer. nat. Dr. hc Hans-Joachim Bunge on the occasion of his 65th birthday," *International Journal of Materials Research,* vol. 85, no. 8, pp. 554-558, 1994.

[232] T. Watanabe, S. Tsurekawa, X. Zhao, L. Zuo, and C. Esling, "A new challenge: grain boundary engineering for advanced materials by magnetic field application," *Journal of materials science,* vol. 41, pp. 7747-7759, 2006.

[233] S. Tsurekawa, K. Harada, T. Sasaki, T. Matsuzaki, and T. Watanabe, "Magnetic sintering of ferromagnetic metal powder compacts," *Materials Transactions, JIM,* vol. 41, no. 8, pp. 991-999, 2000.

[234] G. Gottstein and D. A. Molodov, "Recrystallization and grain growth: proceedings of the first joint international conference, August 27-31, 2001, RWTH Aachen, Germany," *(No Title),* 2001.

[235] S. Tsurekawa, K. Okamoto, K. Kawahara, and T. Watanabe, "The control of grain boundary segregation and segregation-induced brittleness in iron by the application of a magnetic field," *Journal of materials science,* vol. 40, pp. 895-901, 2005.

[236] H. D. Joo, S. U. Kim, Y. M. Koo, N. S. Shin, and J. K. Choi, "An effect of a strong magnetic field on the phase transformation in plain carbon steels," *Metallurgical and Materials Transactions A,* vol. 35, no. 6, pp. 1663-1668, 2004, doi: 10.1007/s11661-004-0075-y.

[237] M. Enomoto, H. Guo, Y. Tazuke, Y. Abe, and M. Shimotomai, "Influence of magnetic field on the kinetics of proeutectoid ferrite transformation in iron alloys," *Metallurgical and Materials Transactions A,* vol. 32, pp. 445-453, 2001.

[238] H. Guo and M. Enomoto, "Influence of Magnetic Fields on α⁄γ Equilibrium in Fe–C (–X) Alloys," *Materials transactions, JIM,* vol. 41, no. 8, pp. 911-916, 2000.

[239] B. D. Cullity and C. D. Graham, *Introduction to magnetic materials*. John Wiley & Sons, 2011.

[240] S. Blundell, *Magnetism in condensed matter*. OUP Oxford, 2001.

[241] C. Kittel and P. McEuen, *Introduction to solid state physics*. John Wiley & Sons, 2018.

[242] N. W. Ashcroft and N. D. Mermin, "Solid state physics," *(No Title),* 1976.

[243] M. Hillert and M. Jarl, "A model for alloying in ferromagnetic metals," *Calphad,* vol. 2, no. 3, pp. 227-238, 1978/01/01/ 1978, doi: https://doi.org/10.1016/0364-5916(78)90011-1.

[244] O. G. Hegde, "Ab initio based study of magneto-chemo-structural coupling in complex alloys," 2022.